ABSTRACT

Title of thesis: COMPUTATIONAL FLUID DYNAMIC SOLUTIONS OF OPTIMIZED HEAT SHIELD DESIGNS FOR EARTH ENTRY

Degree candidate: Jamie Meeroff

Degree and year: Master of Science, 2010

Thesis directed by: Professor Mark Lewis
Department of Aerospace Engineering

Computational fluid dynamic solutions are obtained for heat shields optimized for aerothermodynamic performance using modified Newtonian impact theory. Aerodynamically, the low-order approach matches all computational simulations within 10%. Benchmark Apollo 4 solutions, at the moment of maximum heating, show that predicted heat fluxes using this approach under-predict convective heat flux by approximately 30% and over-predict radiative heat flux by approximately 16% when compared to computational results. Parametric edge radius studies display a power law reliance of convective heat flux on local edge radius of curvature. A slender, oblate heat shield optimized for a single design point is shown to produce heat fluxes that are 1.8 times what was predicted using the Newtonian approach. For this design, maximum heat flux decreases with the inverse cube of the base cross section sharpness. Uncoupled radiative heat flux results based on CFD solutions for a slender heat shield show that the lower-order approach under-predicts

the heating from the radiating shock layer by 70%, suggesting the infeasibility of empirical relations used to predict radiative heat flux for eccentric blunt-body heat shields. Coupled vehicle/trajectory optimized designs are examined for both lunar return (11 km/s) and Mars return (12.5 km/s) and show possible discrepancies for eccentric cross sections using low-order semi-empirical correlations. Ultimately, gains suggested by the lower order approach using more complex geometries are not reflected in these high-fidelity simulations. In some respects (especially with regards to the heating environment), the simpler shape (i.e. a 25° spherical segment) is the ideal one.

COMPUTATIONAL FLUID DYNAMIC SOLUTIONS OF OPTIMIZED HEAT SHIELDS DESIGNED FOR EARTH ENTRY

by

Jamie G. Meeroff

Thesis submitted to the Faculty of the Graduate School of the
University of Maryland, College Park in partial fulfillment
of the requirements for the degree of
Master of Science
2010

Advisory Committee:
Professor Mark Lewis, Chair/Advisor
Professor James Baeder
Professor David Akin

ACKNOWLEDGMENTS

I would first like to thank my advisor Dr. Mark Lewis for giving me the opportunity to conduct this research and for providing me with the inspiration to pursue hypersonics when I was a bright-eyed freshman at the University of Maryland. I would also like to express gratitude to Dr. Ryan Starkey for his help in getting me started with research process. I would also like to thank my committee members Dr. David Akin and Dr. James Baeder whose instruction provided the basis of understanding for my work.

I also would like to acknowledge the NASA funding that supported this work in its entirety. This research was supported by the Space Vehicle Technology Institute (SVTI), one of the NASA Constellation University Institute Projects (CUIP), under grant NCC3-989, with joint sponsorship from the Department of Defense. Appreciation is expressed to Dr. Darryll Pines, director of the SVT Institute at the University of Maryland, Claudia Meyer of the NASA Glenn Research Center, program manager of CUIP, and to Dr. John Schmisseur and Dr. Walter Jones of the Air Force Office of Scientific Research, the support of whom is greatly appreciated.

Special thanks must go to my coworkers in the hypersonics group (Neal Smith, Vijay Ramasubramanian, Adam Beerman, Kevin Ryan, and Gillian Bussey) whose insight I could not have done with out. An extra thanks goes to Vijay. His countless hours spent managing the *Skystreak* cluster made all this work possible. Joshua Johnson deserves special mention for his work optimizing blunt-body heat shields. I would also like to thank those at NASA Ames Research Center (namely Mike

Wright, David Hash, Chun Tang, Todd White, and Grant Palmer) who were always available to answer my questions about DPLR and NEQAIR no matter how trivial it seemed to be.

Finally, I would like thank my parents: Jose and Susana, my siblings: Daniel, Myrna, and Diego, and my best friend Jackie Refo. All my life, these people have challenged me to be my best through all adversity. Even when things looked bleak, they stood by me, giving me the strength I needed to push through. Thank you.

TABLE OF CONTENTS

LIST OF TABLES

LIST OF FIGURES

LIST OF SYMBOLS

A	=	Coefficient of power law
	=	Body normal Jacobian matrix
A_p	=	Planform area
a_2	=	Semi-major axis of superellipse
B	=	Body tangent Jacobian matrix
b	=	Exponent of power law
b_2	=	Semi-minor axis of superellipse
C	=	Aerodynamic coefficient
D	=	Drag (N)
d	=	Base diameter
dA	=	Local differential area element (m^2)
E^i	=	i-th feasible direction
e	=	Eccentricity
e_V	=	Vibrational energy
e_V^*	=	Equilibrium vibrational energy at temperature T
e_V^{**}	=	Equilibrium vibrational energy at temperature T_V
$\vec{F}_b$	=	External body force vector
$F_{elastic}$	=	Elastic force
$F_{electric}$	=	Electric force
F^n	=	Body normal flux vector at time n
G^n	=	Body tangent flux vector at time n
$\vec{g}$	=	Gravity vector
g_1, g_2, g_3	=	Radiation correlation parameters
g_w	=	Ratio of wall enthalpy to total enthalpy
h_t	=	Altitude (km)
I	=	Radiative intensity
J	=	Vehicle inertia matrix
	=	Jacobian matrix of coordinate transformation
K_N	=	Knudsen number
k	=	Line relaxation steps
k'	=	Absorption coefficient
L	=	Lift (N)
L/D	=	Lift-to-drag ratio
M_∞	=	Free stream Mach number
m	=	Mass (Kg)
m_1	=	Number of sides of the superellipse
$\hat{n}$	=	Body normal vector
n_1, n_2, n_3	=	Superellipse shape control factors
P	=	elliptical grid generation control function
$P_{elastic}$	=	Elastic power
p	=	Pressure (Pa)
p_{xrs}	=	Cross range (km)

p_{dwn}	=	Down range (km)
Q	=	Heat load
	=	Elliptical grid generation control function
$Q_{elastic}$	=	Rate of elastic power production
$Q_{inelastic}$	=	Energy change due to inelastic collisions
Q_{rad}	=	Radiation energy loss
$\vec{q_t}$	=	Quaternion vector
R	=	Torus radius (m)
R^n	=	Solution changes due to fluxes at time n
r	=	Base radius (m)
r_n	=	Nose radius of blunted cone (m)
r_{sh}	=	Shock radius (m)
S	=	Area of base cross section (m^2)
T	=	Bulk translational temperature (K)
T_e	=	Electrical temperature (K)
T_V	=	Vibrational temperature (K)
T_d	=	Park averaged temperature (K)
t	=	Time
U^n	=	Vector of conserved quantities at time n
u_o	=	Mass averaged velocity
$\vec{V}$	=	Velocity vector
V_∞	=	Free stream velocity (m/s)
v_x, v_y, v_z	=	Velocity vector components in the coordinate directions
$\dot{w}_{sp}$	=	Mass production rate of species sp
w_v	=	Wind angle
$\vec{X}^i$	=	i-th feasible vector of design variables
x, y, z	=	Coordinate values
α	=	Angle of attack (°)
β	=	Sideslip angle (°)
γ_E	=	Trajectory flight path angle (°)
γ	=	Specific heat ratio
Δ_{so}	=	Shock stand off distance (m)
ϵ	=	Surface emissivity constant
η	=	Body tangent coordinate direction in computational domain
η'_V	=	Thermal conductivity for vibrational energy
θ_c	=	Half-cone angle (°)
θ_s	=	Half-spherical segment angle (°)
ν_1, ν_2	=	Superellipse parameters
ξ	=	Body normal coordinate direction in computational domain
ρ	=	Density (kg/m^3)
σ	=	Stefan Boltzmann constant
τ	=	Shear stress tensor
τ_{T-V}	=	T-V relaxation time
τ_{e-V}	=	e-V relaxation time

ϕ	=	Sweep angle (radians)
Ω_q	=	Vehicle tracking standard update matrix
ω_b	=	Body rotation rate (rads/sec)

Superscripts

i	=	Component of orthogonal coordinate direction
j	=	Component of orthogonal coordinate direction
n	=	Time step

Subscripts

1	=	Before normal shock
	=	First feasible direction
2	=	After normal shock
	=	Second feasible direction
A	=	Axial force
cg	=	Center of gravity
$conv$	=	Convective
D	=	Drag
E	=	Entry interface (at $h_t = 122$ km)
e	=	Electron
eff	=	Effective
H	=	Horizontal component
i	=	Body normal direction
	=	Surface coordinate direction
j	=	Body tangential direction
	=	Surface coordinate direction
L	=	Lift
m	=	Pitching moment (N-m)
max	=	Point of maximum heat transfer
N	=	Normal force
o	=	Stagnation quantity
p	=	Pressure
rad	=	Radiative
ref	=	Reference
s	=	Stagnation point
sl	=	Shock layer
sp	=	Species number
T	=	Torus
tot	=	Total
V	=	Vertical component
	=	Vibrational
w	=	Wall
Y	=	Side force
∞	=	Free stream

Acronyms

CAD	=	Computer Aided Design
CFD	=	Computational Fluid Dynamics
CFL	=	CourantFriedrichsLewy number
CEV	=	Crew Exploration Vehicle
DES	=	Differential evolutionary Scheme
DOR	=	Design Optimization Tools
DPLR	=	Data Parallel Line Relaxation
GSLR	=	Gauss-Seidel Line Relaxation
MMFD	=	Modified Method of Feasible Directions
MPI	=	Message Passage Interface
MSL	=	Mars Science Laboratory
MUSCL	=	Monotone Upstream-centered Schemes for Conservation Laws
NASA	=	National Aeronautics and Space Administration
NEQAIR	=	Non-equilibrium Air Radiation
POST	=	Program to Optimize Simulated Trajectories
SCEBD	=	Self-Consistent Effective Binary Diffusion
UPTOP	=	University of Maryland Trajectory optimization Program

Chapter 1

Introduction

1.1 Motivation

A key aspect in mankind's exploration of space has been the safe delivery of human beings or sensitive equipment to the surface of a planetary body. In order to complete this objective, a vehicle must endure intense aerothermodynamic loads on its forward surfaces that must be absorbed or dissipated using a thermal protection system. Since Allen and Eggers showed the benefits of using a blunt body to defray the adverse heat loads of entry in the 1950's,[1] all NASA missions involving atmospheric penetration have employed some manner of axisymmetric, blunt heat shield. The manned capsule missions of the 1960's and early 1970's (Mercury, Gemini, and Apollo) all employed a spherical segment, ablating heat shield while the Martian Viking and Pathfinder missions both used a slightly more complex spherically blunted cone geometry to deliver their hardware to the surface of the Red planet. While these designs have served well in their various missions, the improved ability to handle heat loads often comes at the price of poor aerodynamic performance, particularly in regards to L/D (which correlates to less flexibility and safety in landing). There is considerable utility in an optimized shape, neither necessarily axisymmetric nor entirely blunt, that balances thermodynamic loads with aerodynamic performance in an ideal fashion.

To that end, previous work at the University of Maryland introduced a single design point optimization[2] using modified Newtonian impact theory to add newer shapes, such as those with elliptical and polygonal base cross sections, to the design space for entry vehicles. Generally, higher L/D ratios are generated by employing a parallelogram cross section with more of a nosecone-like axial profile. Coupling trajectory analysis allowed the optimizer to explore time dependent characteristics such as heat load, cross range, and deceleration loads for an entire entry profile. Optimized vehicle and trajectory pairs have been generated using this method for both Lunar return[3,4] (11 km/s) and Mars return[4,5] (12.5 km/s) mission profiles.

The present work uses computational fluid dynamic solutions in order to test the underlying assumptions of the optimization process as well as to explore regions of the flow field not necessarily covered by the simple surface inclination methods employed in their original derivation. This is done to provide a more robust analysis of the conclusions in the works by Johnson.[2–6] The effect of changing the shoulder radius and edge sharpness of optimized geometries on the resulting aerothermodynamics is detailed. Slender, rounded polygons and other unconventional shapes generated for earth entry at extra-orbital speeds are examined in order to produce a clearer picture of the hypersonic aerothermodynamic environment experienced by these vehicles, and to determine if the boundaries of the current design space are valid or need to be altered. Preliminary uncoupled radiation solutions are also explored for select shapes to understand better the full heating profile of these types of geometries. Ultimately, the scope of this work will be to enhance the understanding of the design space for a lower-order optimization method using higher fidelity computational fluid dynamics, so that more viable results can be generated in future studies.

1.2 Previous Work

The goal of this work is to analyze the merits of particular heat shield design optimized for certain favorable aerothermodynamic characteristics, not to add to the design space for re-entry vehicles. As such, this section will not delve into the history of blunt body entry, but rather provide a general overview of the process of Johnson, et al.[2–6] in which optimized blunt body geometries were developed for certain design parameters. For a more detailed discussion as to what motivated the particular choices that make up the optimization model please see Refs. [5] and [6]. The aforementioned optimization procedure involves four main aspects: (1) choosing a geometry, (2) determining the aerodynamics, (3) calculating the heating profile, and (4) finding the optimum balance of (1)-(3).

1.2.1 Heat Shield Geometries

The heat shield shapes examined in this study were defined by Johnson, et al.[2] and are formed by sweeping an axial profile (one of three different geometric patterns) around the axis of an elliptical base cross section. The coordinate system used in this work is shown in Figure 1.1. Where ϕ is the rotation angle of the cross section and ω is a sweep angle for the axial profile.

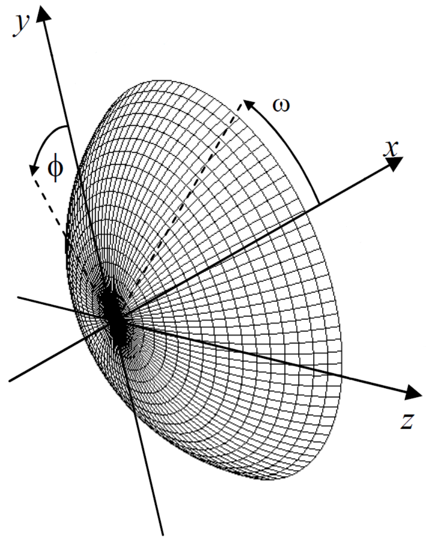

Figure 1.1: Fixed-body coordinate system shown on a 60°axisymmetric spherical segment heat shield

1.2.1.1 Base Cross Section

The base is controlled by Gielis' superformula of the superellipse[7] with $0 \leq \phi \leq 2\pi$ shown as:

$$r(\phi) = \left[\left|\frac{\cos(\frac{1}{4}m_1\phi)}{\nu_1}\right|^{n_2} + \left|\frac{\sin(\frac{1}{4}m_1\phi)}{\nu_2}\right|^{n_3}\right]^{-1/n_1} \tag{1.1}$$

This equation has the ability to produce a wide range of eccentric concave or convex with round or sharp edges solely by varying the individual parameters. Here, the m_1 parameter corresponds to the number of sides of the superellipse. All cases studied in this work use a value of $m_1 = 4$, as it has been shown that this particular value produces geometries with the highest L/D.[2] For this value of m_1, the n_1 modifier must be set to 1 to form viable designs. In order to produce closed shapes, be they sharp or round edged, both ν_1 and ν_2 must also be set to unity and n_3 must equal n_2. The n_2 parameter controls the concavity and edge sharpness of the base. When $n_2 = 2$ the base is an ellipse (regardless of the value of m_1 or n_1). The base is convex when $n_2 < 2$ and concave when $n_2 > 2$. Since convex heat shields may be infeasible to efficiently implement, this work only considers shapes with $n_2 \leq 2$. A sample of the range of shapes Eq. 1.1 is able to create by varying n_2 is shown in Figure 1.2.

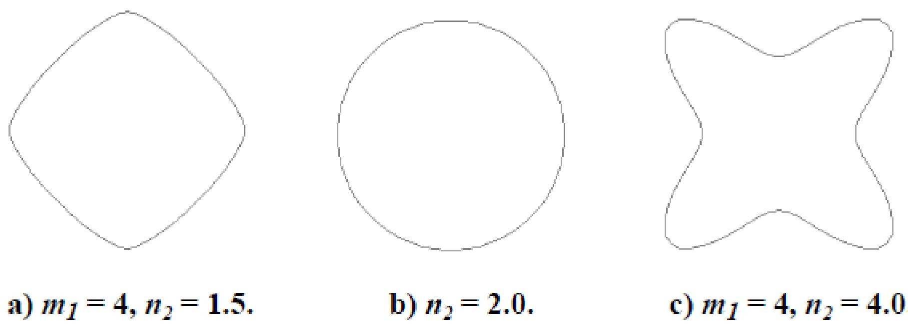

Figure 1.2: Range of shapes produced by Eq. 1.1, from ref [5]

Traditional definitions of eccentricity do not apply here as $\nu_1 = \nu_2 = 1$. Still, "eccentric" shapes can be generated by defining a new set of semimajor and semiminor axes based on an input eccentricity parameter, e, as shown in the following equations:

$$a_2 = \begin{cases} b_2(1-e^2)^{\frac{1}{2}} & -1 < e < 0 \\ 1 & 0 \leq e < 1 \end{cases} \tag{1.2}$$

$$b_2 = \begin{cases} 1 & -1 < e < 0 \\ a_2(1-e^2)^{\frac{1}{2}} & 0 \leq e < 1 \end{cases} \tag{1.3}$$

Here e is fixed between -1 and 1, and prolate and oblate shapes are produced when $e > 0$ and $e < 0$ respectively. By using these new values of semimajor and semiminor axes to scale the Cartesian components of a proportioned (to a desired reference radius) version of the superformula of the superellipse, a wide range of elliptic, rounded edge bases may be produced as shown in Figure 1.3.

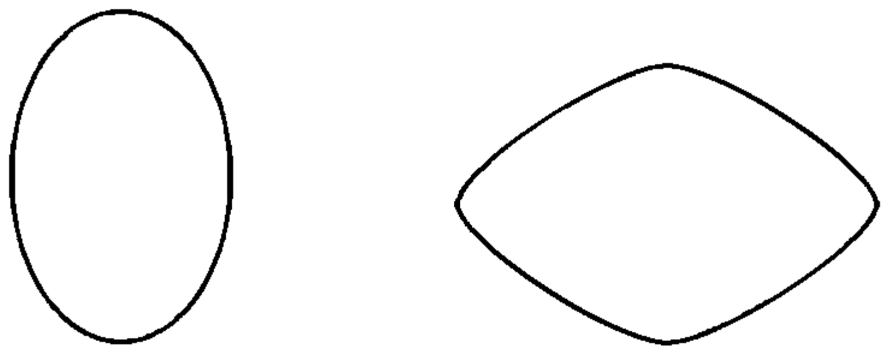

(a) $n_2 = 2.0$, $e = .75$ (b) $n_2 = 1.5$, $e = -.75$

Figure 1.3: Example of oblate and prolate bases

1.2.1.2 Axial Profiles

The heat shield axial profile was defined by Johnson[4,6] as the portion of the vehicle that protrudes from the base. Three different axial shapes were used to generate the geometries in the optimizer design space: (1) a spherical segment, (2) a spherically blunted cone, and (3) a power law. Once chosen, axial profiles are then swept about the contour of the base cross section to construct the full 3-D geometry. Since the base of the heat shield is not axisymmetric, the axial profiles need to be scaled to the local radius of the base at a given particular sweep angle. Thus the axial profiles can only be described as the shapes below at $\phi = 0$. More generally, the axial shape at a given rotation angle is a scaled version of the three classes of profiles presented in this section.

The spherical segment was defined as the section of sphere encompassed by a spherical segment angle θ_s in which a plane parallel to the yz-plane divides the sphere. The Apollo Command Module employed a spherical segment as its heat shield, with $\theta_s = 25°$. A spherically blunted cone was, simply, a cone with its tip replaced by a spherical nose. This profile was defined by the cone angle (θ_c) and by the ratio of nose radius to base diameter (r_n/d).An axisymmetric spherically blunted cone heat shield was used by the NASA Viking spacecraft to safely traverse the Martian atmosphere. Finally, the power law axial profile was defined by the equation:

$$y = Ax^b \tag{1.4}$$

Where the A parameter provides a measure of bluntness for the shape while the b parameter transforms the shape from a sharp cone ($b = 0.01$) to a flat surface ($b = 1.0$). Figure 1.4 shows examples of these three kinds of axial profile. It should be noted, however, that in this work, no heat shields with an axial profile of a power law are explored, as optimized designs with that profile mimicked designs that used the other axial profiles.

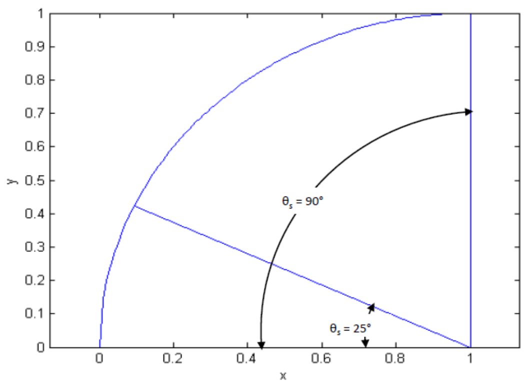

(a) Spherical Segment

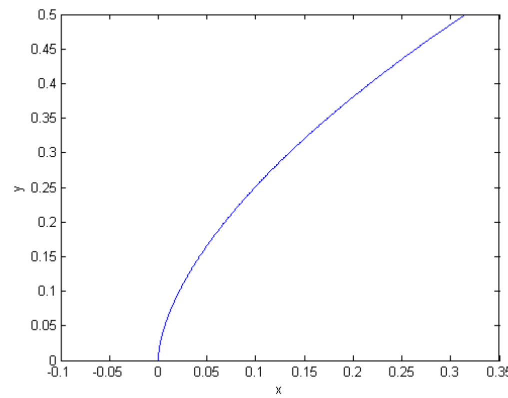

(b) Power Law ($A = 1$, $b = 0.6$)

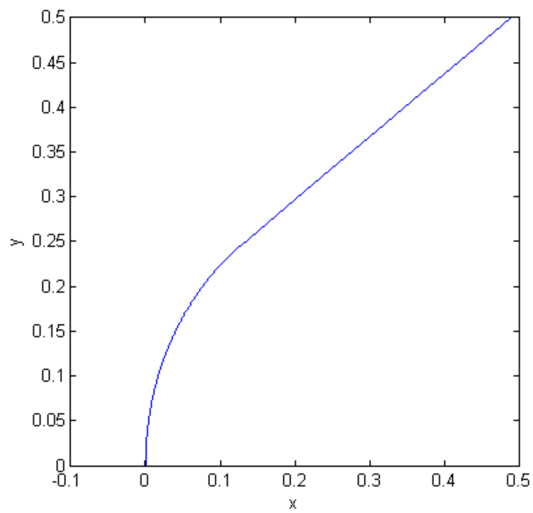

(c) Blunted Cone ($r_n/d = 0.3$, $\theta_c = 35°$)

Figure 1.4: Axial Shapes

1.2.2 Aerodynamic Model

The aerodynamic characteristics of a certain design were calculated based on a modified Newtonian surface pressure distribution. Figure 1.5 shows the conventions for α (angle of attack) and β (sideslip angle) used for all aerodynamic calculations.

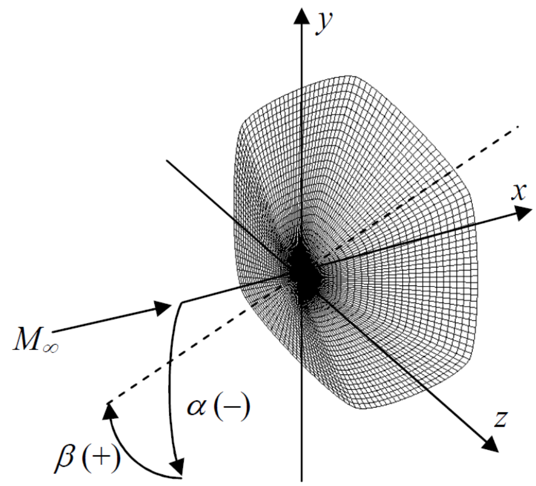

Figure 1.5: Freestream coordinate system for α and β

Newtonian theory assumes that component of a particles momentum normal to a surface is destroyed when impinging upon that surface, while its tangential momentum is conserved.[8–10] The pressure coefficient, in Newtonian theory, is given as:

$$C_p = \begin{cases} C_{p,max}\left(\frac{\vec{V_\infty}\cdot\hat{n}}{\vec{V_\infty}}\right)^2 & \vec{V_\infty}\cdot\hat{n} < 0 \\ 0 & \vec{V_\infty}\cdot\hat{n} \geq 0 \end{cases} \tag{1.5}$$

where $\vec{V_\infty}\cdot\hat{n} \geq 0$ holds in vehicle's shadow region, meaning that the normal component of velocity is either nonexistent or moving away from the body. Applying Equation 1.5 locally, you get (for any point (x, y, z) on the body):

$$C_p = C_{p,max}(V_x n_x + V_y n_y + V_z n_z)^2 \tag{1.6}$$

where V_x, V_y, V_z and n_x, n_y, n_z are the components of the free stream velocity and local normal vector respectively. In simple Newtonian theory, it is assumed that $C_{p,max} = 2$, whereas modified Newtonian theory uses the Rayleigh pitot tube formula[11] which relates stagnation pressure after a shock to the freestream pressure as:

$$\frac{p_{0,2}}{p_\infty} = \left(\frac{1-\gamma+2\gamma M_\infty^2}{\gamma+1}\right)\left(\frac{(\gamma+1)^2 M_\infty^2}{4\gamma M_\infty^2 - 2(\gamma-1)}\right)^{\gamma/\gamma-1} \tag{1.7}$$

This equation, when normalizing by dynamic pressure (q_∞), yields:

$$C_{p,max} = \frac{2}{\gamma M_\infty^2}\left(\frac{p_{0,2}}{p_\infty} - 1\right) \tag{1.8}$$

Integrating Equation 1.6 times a local area element (dA) and a component of the body normal vector(n_x, n_y, n_z) over the surface using Simpson's rule and then dividing by the total planform area (A_p) provides the non dimensional normal, axial, and side forces (C_N, C_A, C_Y). These generalized coefficients can be related to lift and drag by:

$$C_{L,V} = C_N \cos(\alpha) - C_A \sin(\alpha) \tag{1.9}$$

$$C_{L,H} = C_Y \cos(\beta) - C_A \cos(\alpha) sin(\beta) \tag{1.10}$$

$$C_L = \sqrt{(C_{L,V})^2 + (C_{L,H})^2} \tag{1.11}$$

$$C_D = C_N \sin(\alpha) + C_Y \sin(\beta) + C_A \cos(w_v) \tag{1.12}$$

Where w_v is the wind angle defined as:

$$w_v = \arctan\left(\frac{\sqrt{(V_y)^2 + (V_z)^2}}{V_x}\right) \tag{1.13}$$

In this work, analysis is done on heat shields at design points predicted to deliver peak instantaneous heating. At these locations on a particular trajectory, the vehicle is traveling at such high velocities that it can reasonably be assumed that:

$$v_x, v_y >>> v_z \tag{1.14}$$

Equation 1.14 essentially means that, in general, $\beta = 0°$, or that there is no sideslip. With this condition and the x-y plane symmetry of the geometries (true in this work, because $m = 4$), the side force, or C_Y will also be equal to 0. As such, lift and drag now become:

$$C_L = C_{L,V} = C_N \cos(\alpha) - C_A \sin(\alpha) \tag{1.15}$$

$$C_D = C_N \sin(\alpha) + C_A \cos(\alpha) \tag{1.16}$$

A similar process was used to generate aerodynamic moment coefficients for pitching, rolling, and yawing; but, since stability analysis is not performed in this work, those equations are not included here.

1.2.3 Heating Models

The strength and shape of a local bow shock strongly affects the resulting heat transfer delivered to a blunt body in a hypersonic flow. Since conduction through a shock layer is negligible, only convective and radiative heat transfer at the stagnation point were considered in developing the heating model for the optimization process. Convective heat flux is related to a velocity gradient imposed by the body's surface pressure distribution, while radiative heat flux is controlled by the thickness of the resulting bow shock layer. The instantaneous heat flux is defined as a power density in the form of heat per unit area (W/cm^2) and can be integrated along a trajectory, if one exists, to determine a heat load. Though the presence of dissociated and ionized air in a hypersonic shock layer will cause some coupling between these two modes of heat transfer, the heat transfer model employed neglects any coupling effects. It should also be noted here that for all altitude dependent free stream quantities, the 1976 Standard Atmosphere[12] was used.

1.2.3.1 Convection

Convective heat transfer at a point is related to the gradients of velocity around that point, which are, in turn, controlled by the pressure distribution. As shown in section 1.2.2, the local pressure distribution is a function of the geometry of body in the flow. More specifically, a smaller local radius of curvature will generate larger velocity gradients and, thus, a greater amount of heating.[13]

To account for stagnation point convective heat flux, the model of Tauber and Menees[14] was used. The most general form of this model is:

$$q_{s,conv} = (1.83x10^{-8}) r_n^{-0.5} (1 - g_w) \rho_\infty^{0.5} V_\infty^3 \qquad (1.17)$$

Where g_w is the ratio of wall enthalpy to total enthalpy (assumed zero here) and r_n is the local nose radius (obvious for a spherical segment or a spherically blunted cone, but some manipulation was needed to derive an effective nose radius for power law geometries). This correlation assumes equilibrium flow conditions and a fully catalytic surface, which, in theory, produced more conservative heat flux predictions.[8]

This relationship also follows the Fay and Riddell[15] formulation which purports that stagnation point heat flux is proportional to the inverse square root of the local nose radius.

1.2.3.2 Radiation

Radiative heat flux is controlled by three primary factors: (1) nose radius (r_n), (2) shock stand off distance (the farther away from the body the shock is, the larger the radiative heat transfer will be),[13] and (3) angle of attack (α). These parameters were combined to form an effective nose radius upon which to apply the following semi-empirical radiative heat transfer relations. For a sphere at $V_\infty < 9000$ m/s the correlation for radiative heat transfer is:

$$q_{s,rad} = r_{eff} g_1 (3.28084x10^{-4} V_\infty)^{g_2} \left(\frac{\rho_\infty}{\rho_{sl}}\right)^{g_3} \tag{1.18}$$

Where $g_1 = 372.6$, $g_2 = 8.5$, and $g_3 = 1.6$ for $V_\infty < 7620$ m/s[8] and $g_1 = 25.34$, $g_2 = 12.5$, and $g_3 = 1.78$ for 7620 m/s$< V_\infty < 9000$ m/s.[16] For a sphere at $V_\infty \geq 9000$ m/s, the following relation from Tauber and Sutton[17] were applied:

$$q_{s,rad} = 4.376x10^4 r_{eff}^H \rho_\infty^{1.22} f(V_\infty) \tag{1.19}$$

where $H = 1.072x10^6 V_\infty^{-1.88} \rho_\infty^{-0.325}$

where the value for $f(V_\infty)$ was taken from curve fits from tabulated values[17] as:

$$f(V_\infty) = \begin{cases} -3.93206793x10^{-12}V_\infty^4 + 1.61370008x10^{-7}V_\infty^3 & \\ -2.43598601x10^{-3}V_\infty^2 + 16.1078691V_\infty & \\ -39494.8753 & 9000m/s \leq V_\infty \leq 11500 \text{ m/s} \\ 1.00233100x10^{-12}V_\infty^4 + 4.89774670x10^{-8}V_\infty^3 & \\ -8.42982517x10^{-4}V_\infty^2 + 6.255525796V_\infty & \\ -17168.3333 & 11500m/s \leq V_\infty \leq 16000 \text{ m/s} \end{cases} \tag{1.20}$$

Since the above relations are for spheres and the optimized geometries can be other shapes, the effective nose radius in these equations needed to be related back to the actual nose radius. To find this radius, first, the shock strength (ρ_2/ρ_1) was calculated using the method of Tannehill,[18] which employs empirical curve fits for the specific heat ratio (γ) behind the shock . Then, the semi-empirical method of Kaattari[19,20] was employed to determine the physical shock stand-off distance (Δ_{so}). In this method, shock stand off distance is related to the curvature of the shock by the follow equation:

$$\frac{\Delta_{so}}{r_{sh}} = \frac{\sqrt{1 + 4G\left(\frac{r_{sh}}{r_n}\right)} - 1}{2\left(\frac{r_{sh}}{r_n}\right)} \tag{1.21}$$

Where G is determined by curve fits of a function of (ρ_2/ρ_1) and γ. The ratio of r_n to r_{sh} was found by manipulating a combination of further empirical curve fits and the geometry of the blunt body itself, thus allowing Δ_{so} to be backed out. Finally, the empirical curve fit of Reid[21] was applied as shown:

$$\frac{\Delta_{so}}{r_{eff}} = \left(\frac{(\frac{\rho_2}{\rho_1} - 1)^2}{\frac{\rho_2}{\rho_1} - \sqrt{\frac{2\rho_2}{\rho_1} - 1}} - 1 \right) \tag{1.22}$$

This equation defined an effective radius, which essentially relates any shape to an equivalent sphere, that was used to solve Equations 1.18 and 1.19.

In this thesis, analysis is done at trajectory points where peak instantaneous heating is predicted to occur. At super-orbital entry velocities, peak heating will often occur at $V_\infty > 9000 m/s$; therefore, radiation results in this study can only directly be related to values determined from Equation 1.19, the Tauber and Sutton model.

1.2.4 Optimization Methods

This section will briefly delineate the blunt-body optimization procedures developed by Johnson, et al.[2–6] by introducing the fundamentals behind the optimization methods, exploring the objective functions and constraints used, displaying sample geometries, and by discussing the conclusions drawn from these the results for the two separate approaches used to find ideal shapes. For a robust description of the approaches, see Refs. [5] and [6].

1.2.4.1 Single Design Point Optimization

Initially, Johnson sought to derive optimum blunt body heat shield geometries using a gradient based algorithim[2,6] at a single design trajectory point, Apollo 4 peak heating (h = 61 km and M_∞ = 32.8) . Optimizations were done using

Vanderplaats Research & Development, Inc.'s DOT software,[22] which enacted the modified method of feasible directions (MMFD) to minimize or maximize specific objective functions subject to specific inequality constraints and vehicle design side constraints. MMFD works by, first, choosing an initial feasible design, $\vec{X}^1$. Then, a new (in this case, second) search direction, E^2, is formulated from the gradient of the objective function and constraints. A one dimensional search is then conducted to find a scalar, a^* that will minimize the particular objective function in question. The scalar is multiplied by the direction and added to the previous vector of design variables to generate a new $\vec{X}$ of design variables. This procedure continues until convergence and the Kuhn-Tucker conditions[22] are satisfied.

Objective functions used were maximizing L_V/D, maximizing $(L_V/D)/q_{s,tot}$, minimizing $q_{s,tot}$, and minimizing $C_{m,cg,\alpha}$. Optimizations were performed on each objective function for all three different choices of axial profile. The geometric side constraints used are shown in Table 1.1. Most notably, the n_2 parameter has a lower bound of 1.3, which is meant to prevent the generation of shapes with sharp leading edges. The optimization also used inequality constraints for stability and heat flux to prevent certain optimizations from producing entirely infeasible shapes. For example, when optimizing for L_V/D, these constraints ensured that stagnation heat flux would not exceed 3000 W/cm^2.

Figures 1.6 and 1.7 are examples of optimized shapes using this method. Generally, this process showed that high L/D can be achieved by four-sided, rounded edge polynomial cross sections and that it was indeed possible to generate shapes with high lift to drag ratios while keeping peak stagnation point heating below 1000

W/cm^2, less than what was required for NASA's most recent space capsule design (Orion). Still, the design space used in this study often contained a number of local optima, and optimizations were only performed at a single design point; as such, there was no way to determine what vehicle truly represented the ideal.

Table 1.1: Design variables and side constraints used in gradient based optimization

Spherical segment	Spherically blunted cone	Power law
	$55.0° \leq \theta_c \leq 89°$	
$5.0° \leq \theta_s \leq 89.0°$	$0.15 \leq r_n/d \leq 2.00$	$0.900 \leq A \leq 10.000$
$1.3 \leq n_2 \leq 4.00$	$1.3 \leq n_2 \leq 4.00$	$1.3 \leq n_2 \leq 4.00$
$-0.968 \leq e \leq 0.968$	$-0.968 \leq e \leq 0.968$	$-0.968 \leq e \leq 0.968$
$-30° \leq \alpha \leq 30°$	$-30° \leq \alpha \leq 30°$	$-30° \leq \alpha \leq 30°$

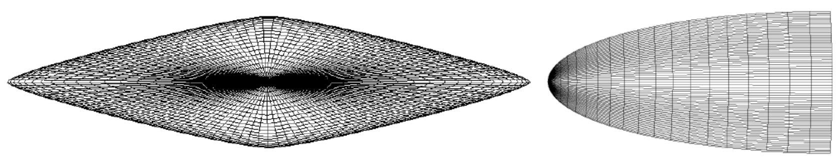

Figure 1.6: Spherical Segment with $n_2 = 1.30$, $e = -.0968$, $\theta_s = 89.0°$, and $\alpha = 18°$ optimized for maximum $(L_v/D)/q_{s,tot}$

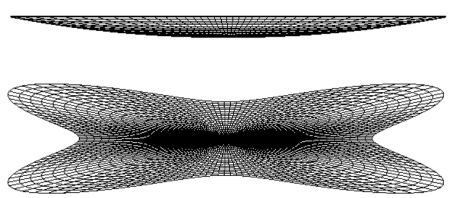

Figure 1.7: Spherical Segment with $n_2 = 4.00$, $e = .0968$, $\theta_s = 15.9°$, and $\alpha = -12°$ optimized for minimum $q_{s,tot}$

1.2.4.2 Coupled Vehicle/Trajectory Optimization

In order to generate more robust optimal solutions, a coupled vehicle/trajectory analysis was performed.[3–5] Generating trajectories allowed for the calculation of time dependent parameters such as heat load and downrange distance. These trajectories were optimized using the University of Maryland, College Park Trajectory Optimization Program(UPTOP),[23] which employs a 4th-order Runge-Kutta routine to propagate the three-degrees-of-freedom point mass equations of rigid-body motion give as:[23–25]

$$\frac{d\vec{p}}{dt} = \vec{V} \tag{1.23}$$

$$\frac{d\vec{V}}{dt} = \frac{B}{m}\vec{F_b} + \vec{g} \tag{1.24}$$

$$\frac{d\vec{\omega_b}}{dt} = (J^{-1}\Omega_b J)\vec{\omega_b} + J^{-1}\vec{T_b} \tag{1.25}$$

$$\frac{dm}{dt} = -\left(\frac{dm}{dt}\right)_{fl} \tag{1.26}$$

$$\frac{d\vec{q_t}}{dt} = -\frac{1}{2}\Omega_q\vec{q_t} \tag{1.27}$$

where ρ, V, and g are given in an inertial reference frame and ω, body rotation rate, is specified in a vehicle coordinate system. UPTOP uses a differential evolutionary scheme (DES)[26] to find an ideal solution, where designs, as in nature,[27] are evolved through generations based on mutation and cross-over factors until an optimum is found. UPTOP compared favorably to the Program to Optimize Simulated Trajectories (POST),[28] NASA's primary trajectory optimization code, for an optimal Space Shuttle ascent trajectory through main engine cutoff.[4] Multiple objective functions were used to find a set of non-dominated solutions, or a Pareto frontier, to a given problem. Figure 1.8 shows an example of a Pareto frontier in which heat load ($Q_{s,tot}$) is minimized and downrange (p_{dwn}) is maximized concurrently. Essentially, the Pareto frontier is set of solutions in which one design may be better than another with respect to one of the objective functions, but not all of them.[27] The optimal solution lies on this Pareto frontier and balances all desired objective functions in an ideal fashion

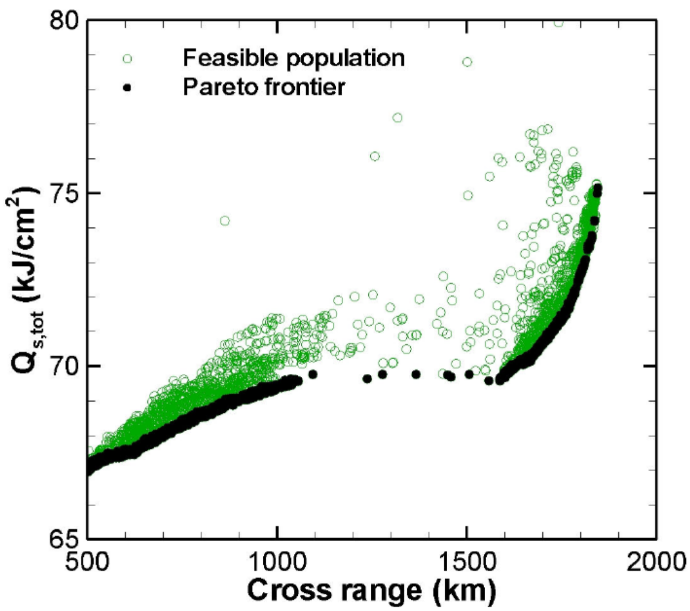

Figure 1.8: Pareto frontier example for a spherical segment ($L/D = 0.5$, $V_E = 12.5$ km/s)

Optimizations were performed at both lunar return ($V_E = 11$ km/s) and Mars return ($V_E = 12.5$ km/s) using two multi-objective functions sets: (1) maximizing cross range p_{xrs} (to provide for more abort scenarios) while minimizing stagnation point heat load $Q_{s,tot}$ (so that heat shield mass can be reduced) and (2) maximizing down range p_{dwn} while minimizing stagnation point heat load $Q_{s,tot}$. Trajectories were limited to six bank angle (ϕ_b) changes for $L/D = 0.3$ and 0.5 and ten changes for $L/D = 1.0$. Trajectories had to also be chosen to possess robust entry corridors, allowable regions of entry flight path angle γ_E, in order to provide for suitable off-design survivability of individual designs. Finally, lower and upper mass constraints were set in order to bracket all possible blunt-body solutions.

Table 1.2 shows the geometric side constraints used for this particular optimization process. It should be noted that for lunar return, only spherical segment geometries were considered while both spherical segments and spherically-blunted cones were examined for Mars return. The other axial profiles were not used because optimization using those shapes produced designs that mimicked other geometries, thus not introducing new heat shields, but rather reproducing already generated ones. Another notable feature of these geometric constraints is that the n_2 sharpness parameter is bounded below by 1.3, which allows for rounded parallelogram cross sections, and above by 2.0, which prevents any concave shapes from being introduced.

Furthermore, Table 1.3 shows the trajectory and aerodynamic constraints used. The constraints allowed for sensible trajectories and for general aerodynamic stability. Mach number and altitude final conditions are based on suitable values for parachute deployment, and deceleration loads (n_{max}) were limited to values less than what was experienced on Apollo 10 ($7g$).[29,30]

Figures 1.9 and 1.10 show examples of vehicles and corresponding trajectories optimized using this approach for both lunar and Mars return respectively. Generally, it was found that shapes with a larger drag area, specifically $C_D S$ (drag

Table 1.2: Design variable constraints used in vehicle/trajectory optimization

L/D	$V_E = 11.0$ km/s L/D specific design variables	$V_E = 12.5$ km/s L/D specific design variables
0.3, 0.5	$5.0° \leq \theta_s \leq 89.0°$ $-0.968 \leq e \leq 0.968$ $-30° \leq \alpha \leq 30°$	$5.0° \leq \theta_s \leq 89°,\ L/D=0.3$ $20.0° \leq \theta_s \leq 89°,\ L/D=0.5$ $55.0° \leq \theta_c \leq 89.0°$ $0.15 \leq r_n/d \leq 2.0$ $-0.968 \leq e \leq 0.968$ $-30° \leq \alpha \leq 30°$
1.0	$50.0° \leq \theta_s \leq 89°$ $-0.968 \leq e \leq -0.95$ $0° \leq \alpha \leq 30°$	$50.0° \leq \theta_s \leq 89°$ $-0.968 \leq e \leq -0.95$ $0° \leq \alpha \leq 30°$
Common design variables		
	$1.3 \leq n_2 \leq 2.00$ $5s \leq t_1 \leq 55s$ $t_1+10s \leq t_2 \leq t_1+55s$ $t_2+10s \leq t_3 \leq t_2+55$ $t_3+10s \leq t_4 \leq t_3+55s$ $t_4+10s \leq t_5 \leq t_1+3605s$ $t_5+10s \leq t_4 \leq t_1+3605s$	$0.27 \leq L/D \leq 0.33$ $0.47 \leq L/D \leq 0.53$ $0.95 \leq L/D \leq 0.1.05$ $0° \leq \phi_{b,all} \leq 180°$ For $L/D = 0.3\&0.5$ $all = 0, 1, 2, \cdots, 5, 6$ For $L/D = 1.0$ $all = 0, 1, 2, \cdots, 9, 10$

Table 1.3: Trajectory/aerodynamic constraints vehicle/trajectory optimization

Optimization constraints	
Trajectory	Aerodynamic/Geometric
	$M_{\infty,f} = 2$
$t_f \leq 3600s$	$C_{m,cg,\alpha} \leq -0.001$
$n_{max} \leq 5g$	$C_{n,cg,\beta} \geq 0.001$
$h_t \leq 1220km$	$sign(C_{L,V})C_{l,cg,\beta} \leq 0.01$
$10km \leq h_{t,f} \leq 45km$	$\|\alpha\| \leq \|\epsilon + 1°\|$

coefficient times reference area), can decelerate at a higher altitude, in a less dense part of the atmosphere, and thus produce the lowest heat loads. Also increases in mass were shown to correlate as an almost linear increase to heat load. For lunar return, dramatic improvements in heat loads and cross range over the Orion CEV design at $L/D = 0.27$ were shown by using 5° spherical segment with a highly oblate cross section ($e = -.0968$) due mostly to higher drag area and L/D.

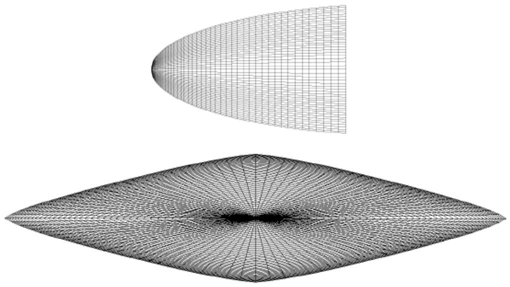

(a) Geometry

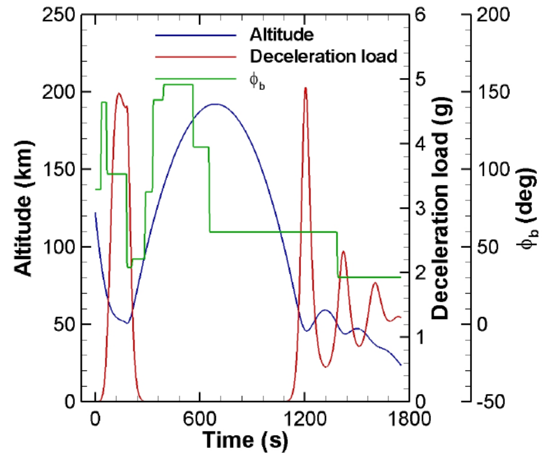

(b) Trajectory

Figure 1.9: Spherical segment with $\theta_s = 75.7°$, $n_2 = 1.31$, and $e = -0.967$ optimized for Lunar Return ($V_E = 11km/s$)

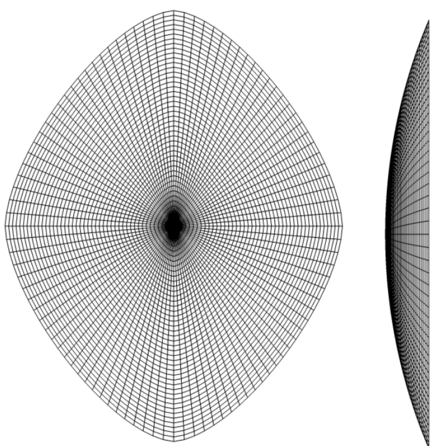

(a) Geometry

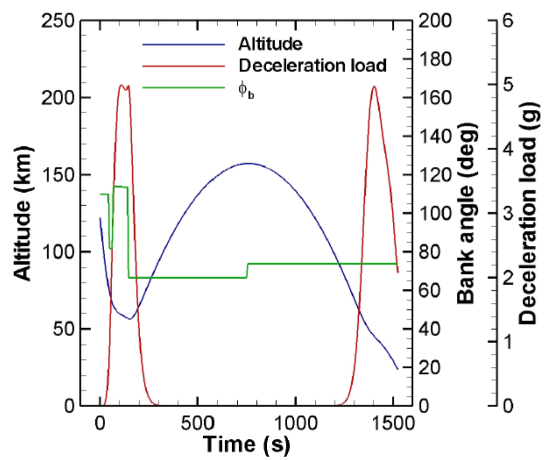

(b) Trajectory

Figure 1.10: Spherical segment with $\theta_s = 23.7°$, $n_2 = 1.66$, and $e = 0.621$ optimized for Lunar Return ($V_E = 12.5$ km/s)

1.3 Objectives and Contributions

The aim of this thesis is to analyze the merit of the aforementioned models to truly attain an optimum blunt body heat shield solution. A high fidelity CFD package, DPLR, is employed to explore these optimized heat shield designs in full detail. The ability of stagnation point relations and semi-empirical correlations to fully predict the volatile environment of planetary re-entry are probed in order to see how well they stand up when the full flow physics is considered. Ultimately, this work aspires to find areas of possible improvement of the above optimization model, weather it be in the constraints and equations themselves, or by illuminating areas of the flow-field not covered by the lower-order approach (i.e. off stagnation point heating). As CFD can be especially costly, especially in high temperature environment like re-entry, certain parts of the lower-order model, such as the trajectory integrated variables of heat load and downrange, could not be analyzed with the higher order simulation. Still, the results presented here provide invaluable detail to the design space of a lower-order heat shield optimization process.

Some important results of this thesis include: (1) that the low-order optimization approach does produce reasonable initial results for blunt-body aerothermodynamics (especially in regards to the aerodynamic coefficients), (2) that high off stagnation point convective heating in parallelogram base designs implies the need to further constrain the n_2 parameter to something higher than 1.3, (3) that the semi-empirical relation used to predict convective and radiative heat transfer break down when used on more eccentric shapes rather than just spheres, and (4) that, when practical matters are considered, a simple axisymmetrical spherical segment blunt body heat shield provides near optimal performance for both lunar and Mars return without the need to manufacture exotic shapes. These results come out of extensive benchmarking of the computational tools (Chapter 2) using the Apollo capsule at Apollo 4 peak heating conditions as a test subject (Chapter 3). A geometry from the single point optimization procedure[2,6] is then examined (Chapter 4) parametrically to fully understand the effects of changing certain geometric parameters. Chapter 5 looks at optimized shapes for lunar[3,4] and Mars[4,5] return, and explore how these designs hold up in a fully realized flow. Finally, Chapter 6 contains gathers all important conclusions in full detail and provides a summary of this work's important contributions to the state of the art.

Chapter 2

Computational Tools

This chapter provides an overview of the various computational resources employed to simulate blunt body re-entry flows. Only pre-existing software was used; however, modifications were necessary, especially to ensure that the flow solver would properly function on the specific hardware found at the University of Maryland, College Park. Essentially, a blunt-body CFD run involves taking the geometric parameters from the optimizer (as described in Chapter 1), creating a volume mesh from those parameters, converging a hypersonic solution using the CFD flow solver, post-processing to examine the results, and then, finally, calculating the thermal effects due to shock layer radiation (if necessary). This general work-flow pattern is shown in Figure 2.1. The dotted line connecting DPLR, the flow solver, to NEQAIR, the radiation solver, signifies that, though radiation and convection are considered uncoupled in this work, there is a process by which the two heating regimes can be loosely coupled. The individual components used in this work (in the rectangles outside the dotted box) are described in the following sections.

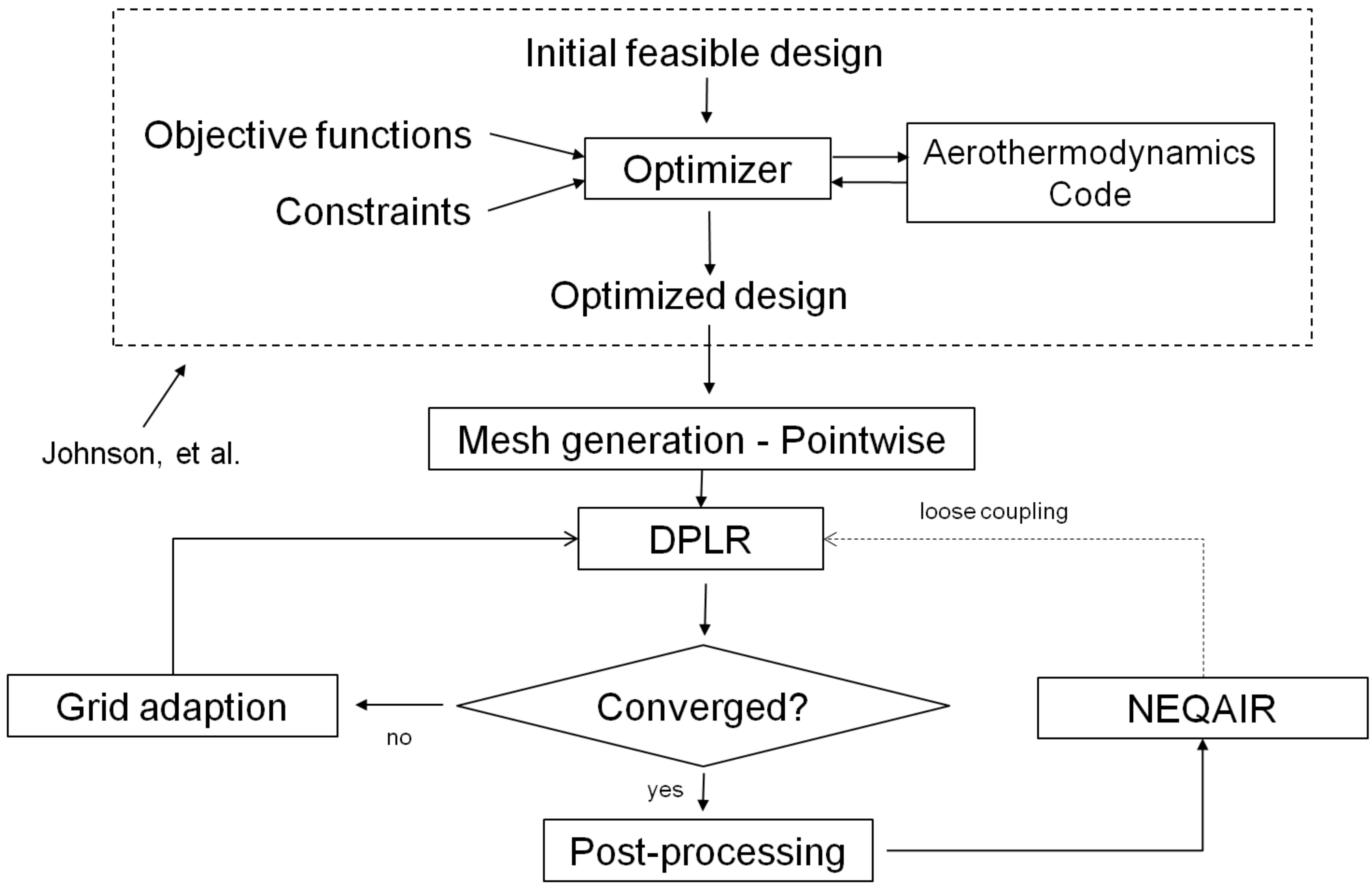

Figure 2.1: Generalized work-flow pattern for blunt-body simulations

2.1 Flow Solver

The high temperature environment of re-entry is modeled using the Data Parallel Line Relaxation (DPLR) code[31] developed at NASA Ames Research Center. DPLR is a Fortran 90 structured multiblock hypersonic continuum code that utilizes the Message Passage Interface (MPI) to spread its workload over multiple computer processors. DPLR was chosen because of its ability to accurately and efficiently model blunt body re-entry at orbital[32] and extra-orbital velocities,[33] and because it was far better suited to the hardware found at the University of Maryland, College Park than other hypersonic continuum solvers, like LAURA.[34,35] Both DPLR V3.05 and V4.0 are used in this work. There is backwards compatibility between the two versions as no changes were made to the parts of the flow solver used in this work during the upgrade.

2.1.1 Nonequilibrium Flow Model

The flow is modeled in DPLR using the chemically reacting conservation equations equations (derived assuming continuum flow and that translational temperature T, vibrational temperature T_V, and electron temperature T_e are all different) shown in general form as:[36,37]

a) Species Continuity

$$\frac{\partial \rho_{sp}}{\partial t} = \frac{\partial}{\partial x^j}(\rho_{sp} u_o^j + \rho_{sp} V_{sp}^j) = \dot{w}_{sp} \tag{2.1}$$

where sp is an individual species, x^j is j^{th} component of the orthogonal coordinate directions, $\dot{w}_{sp}$ is the mass production rate of a species sp per unit volume, ρ_{sp} is the mass density of species sp, u_o^j is the j^{th} component of mass averaged velocity, and V_{sp}^j is the j^{th} component of the species mean velocity.

b) Overall Continuity

$$\frac{\partial \rho}{\partial t} + \frac{\partial}{\partial x^j}(\rho u_o^j) = 0 \tag{2.2}$$

where ρ is the sum of the individual species densities.

c) i^{th} Direction Species Momentum Conservation

$$\begin{aligned}
&\frac{\partial}{\partial t}(\rho_{sp} u_{sp}^i) + \frac{\partial}{\partial x^j}(\rho_{sp} u_o^i u_o^j) + \frac{\partial}{\partial x^j}(\rho_{sp} u_o^i V_{sp}^j + \rho_{sp} u_o^j V_{sp}^i) \\
&+ \frac{\partial p_{sp}}{\partial x^i} - \frac{\partial \tau_{sp}^{ij}}{\partial x^j} = F_{elastic,sp}^i + F_{electric,sp}^i
\end{aligned} \tag{2.3}$$

where $\tau^{i,j}$ is the shear stress, $F_{electric}$ is the electric force (a function of electric field), and $F_{elastic}$ is the force generated by elastic collisions between molecules (from kinetic theory).

d) i^{th} Direction Overall Momentum Conservation

$$\frac{\partial}{\partial t}(\rho u_o^i) + \frac{\partial}{\partial x^j}(\rho_{sp} u_o^i u_o^j) + \frac{\partial p}{\partial x^i} - \frac{\partial \tau^{ij}}{\partial x^j} = \sum_{sp} F_{elastic,sp}^i \tag{2.4}$$

where $\tau^{i,j}$, p, and $F_{elastic}$ are now summed over all species.

e) Electron (denoted by e subscript) Energy Conservation

$$\begin{aligned}
&\frac{\partial}{\partial t}\left[\rho_e\left(\frac{1}{2}u_o^2 + u_o^i V_e^i + e_e\right)\right] + \frac{\partial}{\partial x^j}\left[\rho_e u_o^j\left(\frac{1}{2}u_o^2 + e_e\right)\right] \\
&+ \frac{\partial q_e^j}{x^j} + \frac{\partial}{\partial x^j}\left(\frac{1}{2}\rho_e u_o^2 V_e^j + \rho_e u_o^j u_o^i V_e^i\right) + \frac{\partial}{\partial x^i}(u_o^i p_e) \\
&- \frac{\partial}{\partial x^j}(u_o^i \tau_e^{i,j}) = P_{electric,sp} + Q_{elastic,sp} + Q_{inelastic,sp}
\end{aligned} \tag{2.5}$$

where e_e is the energy per unit mass of an electron, $P_{electric}$ is a power supplied by an electric field on charged particles, $Q_{elastic}$ is the rate of energy due to elastic collisions, and $Q_{inelastic}$ is the energy change due to inelastic collisions (including radiation).

f) Species Vibrational Energy Conservation

$$\frac{\partial}{\partial t}(\rho_{sp}e_{V,sp}) + \frac{\partial}{\partial x^j}(\rho_{sp}e_{V,sp}u_o^j) = \frac{\partial}{\partial x^j}\left(n'_{V,sp}\frac{\partial T_V}{\partial x^j}\right)$$
$$-\frac{\partial}{\partial x^j}(\rho_{sp}e_{V,sp}V_{sp}^j) + \rho_{sp}\frac{e_{V,sp}^*(T) - e_{V,sp}}{\tau_{T-V,sp}} + \rho_{sp}\frac{e_{v,sp}^{**}(T_e) - e_{V,sp}}{\tau_{e-V,sp}} \tag{2.6}$$

where $e_{V,sp}$ is the vibrational energy for a species sp, $n'_{V,sp}$ is the thermal conductivity for vibrational energy, $\tau_{T-V,sp}$ and $\tau_{e-V,sp}$ are the T-V and e-V relaxation times for a species sp respectively, and $e^*_{V,sp}$ and $e^{**}_{V,sp}$ are the equilibrium vibrational energy of species sp at T and T_e respectively.

g) Overall Energy Conservation

$$\frac{\partial}{\partial t}\left[\rho\left(\frac{1}{2}u_o^2 + e\right)\right] + \frac{\partial}{\partial x^j}\left[\rho_e u_o^j\left(\frac{1}{2}u_o^2 + e\right)\right]$$
$$+\frac{\partial q^j}{x^j} + \frac{\partial}{\partial x^i}(u_o^i p) - \frac{\partial}{\partial x^j}(u_o^i \tau^{i,j}) = P_{electric} + Q_{rad} \tag{2.7}$$

where e is the total thermodynamic energy per unit mass, q^j is the j^{th} component of the overall heat-flux vector, and Q_{rad} is the radiation loss.

The above equations are further simplified, by choosing the appropriate simplifications within DPLR itself. Due to the high velocities experienced upon Lunar and Mars return, an 11 species (N_2, O_2, NO, NO+, O_2+, N, O, N+, O+, e), 19 reaction finite rate chemistry model for air from Park[38] is considered in order to capture the effects of ionization caused by thermal and chemical nonequilibrium expected after the bow shock. The flow is assumed to be in thermal nonequilibrium using the two-temperature model of Park[39] which uses an averaged temperature, defined as:

$$T_d = \sqrt{T T_V} \tag{2.8}$$

to control dissociation rates. Ionization reactions are governed by bulk translational temperature, T, as in the work by Olynick et al.,[40] and translational and vibrational energy modes are modeled by a Landau-Teller formulation, which uses relaxation times from Milikan and White.[41] Viscous transport and thermal conductivity are modeled using the mixing rules of Gupta et al.,[42] while species diffusion coefficients are calculated using the self-consistent effective binary diffusion (SCEBD) method of Ramshaw.[43] Only the three dimensional laminar versions of the governing equations are considered in this work, which is a reasonable assumption for blunt-bodies entering Earth's atmosphere. Since many different materials exist for use in thermal protection, a super-catalytic boundary condition is used for the heat shield surface. A super-catalytic surface assumes that the chemical composition of the body is identical to that in the freestream, resulting in conservative heating estimates useful for design studies. Consequently, this also means that material response is neglected, as no specific surface material is chosen. The heat-shield surface is also assumed to be in radiative equilibrium, in which energy incident to the surface is radiated back into the freestream based on the equation:

$$q_w = \epsilon \sigma T_w^4 \tag{2.9}$$

where ϵ is the surface emissivity (a constant 0.85 in this work) and σ is the Stefan-Boltzmann constant. This model provides accurate heating predictions, especially for the non-ablating heat-shields explored in this work. Various other boundary conditions, such as periodic or symmetric, can be employed at other mesh boundaries, but the flow at surfaces through which air exits must be supersonic. Due to limitations in the DPLR software, shock layer radiation is neglected in the flow solver; however, uncoupled contributions to the total surface heat flux from the radiating shock layer are calculated, in some cases, with the NEQAIR software package (see Section 2.3).

2.1.2 Numerical Model

DPLR is a fully three-dimensional implicit, upwind Navier Stokes solver that takes into account the physical models discussed above. Euler fluxes are computed using a modified form of Steger-Warming flux vector splitting method developed by MacCormack and Candler,[44] which has less dissipation than the original scheme. Third order spatial accuracy is maintained by a MUSCL (Monotone Upstream-centered Schemes for Conservation Laws) extrapolation with a minmod limiter.[45] A central differencing approach is used to ensure second order accuracy of the viscous fluxes. Time-marching is achieved with the data-parallel line relaxation method(DPLR),[31] which gives the flow solver its name. The DPLR method is essentially a modified version of McCormack's Gauss-Seidel line relaxation(GSLR)[46] in that it uses line relaxation steps instead of Gauss-Seidel sweeps for more efficient parallelization.

The best way to illustrate how the DPLR method works is by applying it to the two-dimensional fully implicit inviscid form of the Navier Stokes equations,[31] defined as:

$$\frac{U^{n+1} - U^n}{\Delta t} + \frac{\partial F^{n+1}}{\partial \xi} + \frac{\partial G^{n+1}}{\partial \eta} = 0 \tag{2.10}$$

where n is a time step, U is the vector of conserved quantities, and F and G are the flux vectors in the body normal (ξ) and body tangential (η) directions. The fluxes can be linearized by:

$$\begin{aligned} F^{n+1} &\approx F^n + \left(\frac{\partial F}{\partial U}\right)^n (U^{n+1} - U^n = F^n + A^n \delta U^n) \\ G^{n+1} &\approx G^n + \left(\frac{\partial G}{\partial U}\right)^n (U^{n+1} - U^n = G^n + B^n \delta U^n) \end{aligned} \tag{2.11}$$

where A and B are the Jacobian matrices of the flux vectors. The fluxes are now split based on the sign of the eigenvalues of the Jacobian matrix as:

$$\begin{aligned} F_+ + F_- &= A_+ U + A_- U = F \\ G_+ + G_- &= B_+ U + B_- U = G \end{aligned} \tag{2.12}$$

which allows Equation 2.10 to written in an upwind finite volume form as:

$$\begin{aligned} &\delta U^n_{i,j} + (\Delta t / V_{i,j})[(A_{+i+\frac{1}{2},j} S_{i+\frac{1}{2},j} \delta U_{i,j} - A_{+i-\frac{1}{2},j} S_{i-\frac{1}{2},j} \delta U_{i-1,j}) \\ &-(A_{-i-\frac{1}{2},j} S_{i-\frac{1}{2},j} \delta U_{i,j} - A_{-i+\frac{1}{2},j} S_{i+\frac{1}{2},j} \delta U_{i-1,j}) \\ &+(B_{+i+\frac{1}{2},j} S_{i+\frac{1}{2},j} \delta U_{i,j} - B_{+i-\frac{1}{2},j} S_{i-\frac{1}{2},j} \delta U_{i-1,j}) \\ &-(B_{-i-\frac{1}{2},j} S_{i-\frac{1}{2},j} \delta U_{i,j} - B_{-i+\frac{1}{2},j} S_{i+\frac{1}{2},j} \delta U_{i-1,j}) = \Delta t R^n_{i,j} \end{aligned} \tag{2.13}$$

where $R^n_{i,j}$ is the solution change due to fluxes at time n, $S_{i,j}$ is the surface area of face i, j, and $V_{i,j}$ is the cell volume. The DPLR method is formed by, first, moving the body normal terms in Equation 2.13 to one side, resulting in:

$$\hat{B}_{i,j}\delta U_{i,j+1} + \hat{A}_{i,j}\delta U_{i,j} - \hat{C}_{i,j}\delta U_{i,j-1} = -\hat{D}_{i,j}\delta U_{i+1,j} + \hat{E}_{i,j}\delta U_{i-1,j} + \Delta t R^n_{i,j} \quad (2.14)$$

where the hatted matrices are defined as:

$$\hat{A}_{i,j} = I + (\Delta t/V_{i,j})(A_{+i+\frac{1}{2},j}S_{i+\frac{1}{2},j} - A_{-i-\frac{1}{2},j}S_{i-\frac{1}{2},j} + B_{+i+\frac{1}{2},j}S_{i+\frac{1}{2},j} - B_{-i-\frac{1}{2},j}S_{i-\frac{1}{2},j})$$

$$\begin{aligned}
\hat{B}_{i,j} &= (\Delta t/V_{i,j})(B_{-i+\frac{1}{2},j}S_{i+\frac{1}{2},j}) \\
\hat{C}_{i,j} &= (\Delta t/V_{i,j})(B_{+i-\frac{1}{2},j}S_{i-\frac{1}{2},j}) \\
\hat{D}_{i,j} &= (\Delta t/V_{i,j})(A_{-i+\frac{1}{2},j}S_{i+\frac{1}{2},j}) \\
\hat{E}_{i,j} &= (\Delta t/V_{i,j})(A_{+i-\frac{1}{2},j}S_{i-\frac{1}{2},j})
\end{aligned} \quad (2.15)$$

Then, the k_{max} line relaxation steps are applied, by first solving a block tridiagonal system, formed by neglecting the implicit terms in 2.14, for $\delta U^{(0)}_{i,j}$ as:

$$\hat{B}_{i,j}\delta U^{(0)}_{i,j+1} + \hat{S}_{i,j}\delta U^{(0)}_{i,j} - \hat{C}_{i,j}\delta U^{(0)}_{i,j-1} = \Delta t R^n_{i,j} \quad (2.16)$$

then, for $k = 1 : k_{max}$:

$$\begin{aligned}
\hat{B}_{i,j}\delta U^{(k)}_{i,j+1} + \hat{S}_{i,j}\delta U^{(k)}_{i,j} - \hat{C}_{i,j}\delta U^{(k)}_{i,j-1} &= -\hat{D}_{i,j}\delta U^{(k-1)}_{i+1,j} + \hat{E}_{i,j}\delta U^{(k-1)}_{i-1,j} + \Delta t R^n_{i,j} \\
\delta U^n_{i,j} &= U^{k_{max}}_{i,j}
\end{aligned} \quad (2.17)$$

Essentially, this method requires one LU substitution (for solving Equation 2.16) and $k_{max} + 1$ back substitutions for a single iteration in time. The hatted matrices only need to be calculated once for each relaxation sweep, and each relaxation step can be done in parallel if body normal information is stored locally.

In the DPLR software itself, the above method is applied to the fully viscous three-dimensional Navier-Stokes equations, which makes the equations slightly more complicated; but, the fundamentals behind the method are the same. Convergence, in DPLR, comes when the L_2 norm of a conserved variable (in this work, total density ρ is used) reaches a sufficiently low level, which essentially means the solution is not changing between time steps and has reached a quasi-steady state. DPLR has the ability to simulate an unsteady flow, but since the heat shields studied in this work are examined at specific trajectory points, this feature is not used.

2.1.3 Work-flow

A typical DPLR simulation for a given blunt-body heat shield case is given as follows. First, a Plot3D volume grid is read into the software using a built in pre-processing package, called *fconvert*. This package converts the mesh into something that DPLR can understand while also breaking it down into smaller blocks. The size and number of these blocks are chosen by the user to divide the computation as evenly and as efficiently as possible over the available computational nodes to ensure rapid convergence. Essentially, whichever node has the most amount of work assigned to it will dictate the convergence time of a given run. Once the grid is sufficiently divided, DPLR itself is invoked, using options supplied in an input file, which contains a CFL number schedule to control the time steps of the simulation. A first run of DPLR will often be run on an un-adapted mesh using a simpler gas model (i.e. one with 5 species instead of 11) in order to quickly generate a baseline solution. Once this initial solution is converged, the mesh is smoothed using the built-in adaption techniques of Saunders,[47] which reshapes a volume grid based on Mach number contours. Then, the more complicated gas model is applied, and DPLR is run a few more times (usually four or five) to convergence, adapting the grid before each run. Once the solution has reached a quasi-steady state, it is considered converged (see previous section). Finally, a built-in post-processor, called *Postflow* is used to extract the pertinent flow characteristics on any part of the volume mesh for view in any graphical interpreter, such as Tecplot. *Postflow* also has the ability to integrate flow variables over surfaces, which is useful in generating non-dimensional aerodynamic coefficients for lift and drag (as long as the proper reference quantities are defined).

2.1.4 Code Modifications and Validation

DPLR was written primarily for use on the *Columbia* supercomputing cluster at NASA Ames Research Center; as such, it was necessary to alter the software's source code for proper function on a cluster at University of Maryland, College Park (more detail on both clusters can be found in Section 2.4). The changes, while not trivial, amount mostly to differences in semantics used by various Fortran 90 compilers. That being said, validation cases were run using the modified version of DPLR (the changes were identical for both DPLR version 3.05 and DPLR version 4.0) using a series of sample files distributed with the DPLR software package. Table 2.1 shows the different compiler/architecture sets used in this validation study.

All sample cases generated the exact same results for all the compilers/architectures used. For example, figures 2.2 and 2.3 show Mach contours on the symmetry plane for the Mars Science Laboratory(MSL) and surface skin friction coefficients for a 2-D cylinder respectively. Essentially, these results suggest that no errors were introduced into the code by the modifications made to the source.

Table 2.1: Compilers and architectures used in DPLR validation study

Compiler	MPI Package	Platform	Cluster Name
Pathscale[48]	Open MPI[49]	AMD 64 bit	*Skystreak* (UMD)
Intel Fortan[50]	Open MPI	Intel 32 bit	*Columbia*
Gnu-Fortan[51]	Open MPI	Intel 32 bit	-
Portland Group Fortan[52]	LAM/MPI[53]	AMD 64 bit	-

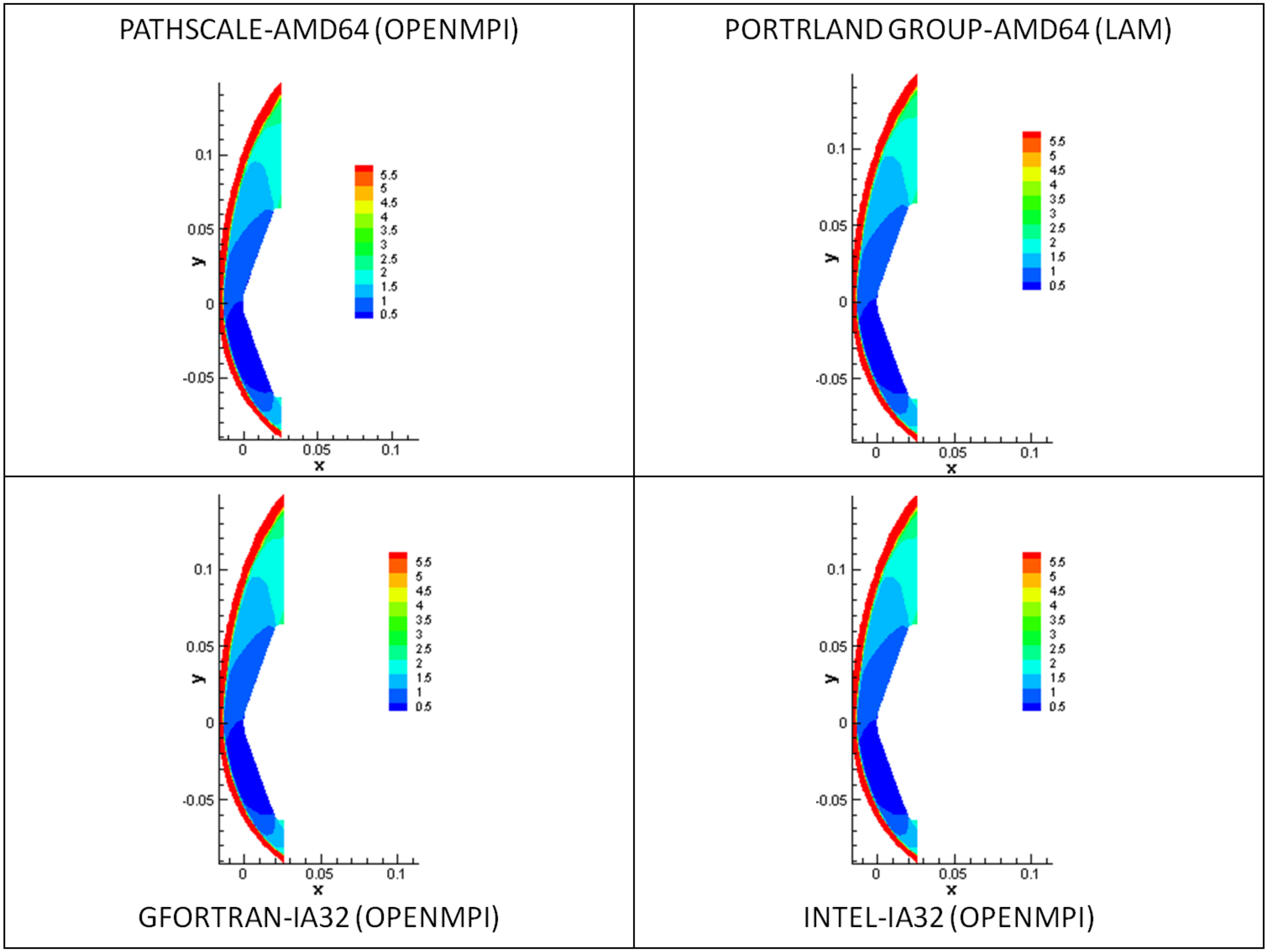

Figure 2.2: Mach number contours on symmetry plane for MSL

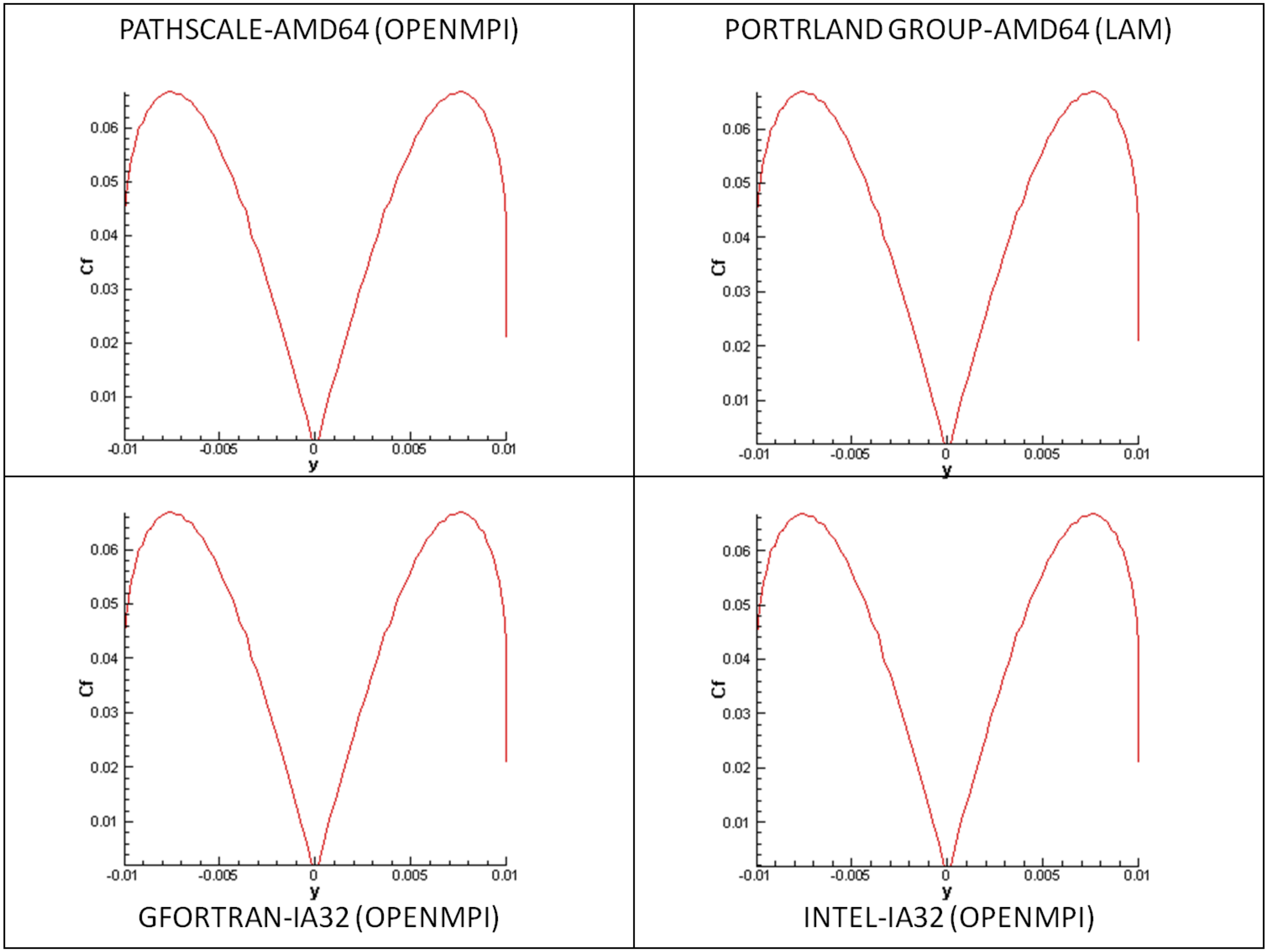

Figure 2.3: Surface skin friction coefficients on a 2-D cylinder

2.2 Grid Generation

Topologies are created using the commercially available elliptic grid generation package, Pointwise.[54] This package is an upgrade to the commonly used Gridgen[55] software in the sense that it has a more streamlined graphic user interface (GUI) and enhanced undo capabilities. The later feature is especially useful, since grid generation will often devolve into a trial-and-error procedure where multiple meshes are created until one "looks" right A good "looking" mesh will often have orthogonality near its the boundaries and have no adverse stretching in its cells). Pointwise can create both structured and unstructured meshes, but only structured grids can be input to DPLR. Once a surface grid is created, Pointwise can improve the quality of the mesh by using different control functions (Laplace, Middlecoff-Thomas,[56] and Steger-Sorenson[57]) to iteratively solve Poisson's elliptical partial differential equations given, in the computational domain, by:[58]

$$\begin{aligned} \alpha x_{\xi\xi} - 2\beta x_{\xi\eta} + \gamma_{\eta\eta} &= -J^2(Px_\xi + Qx_\eta) \\ \alpha y_{\xi\xi} - 2\beta y_{\xi\eta} + \gamma_{\eta\eta} &= -J^2(Py_\xi + Qy_\eta) \end{aligned} \tag{2.18}$$

with:

$$\alpha = x_\eta^2 + y_\eta^2 \qquad \beta = x_\xi x_\eta + y_\xi y_\eta \qquad \gamma = x_\xi^2 + y_\xi^2$$

where (x, y) are the Cartesian coordinates of the mesh, (ξ, η) are the transformed mesh points in the computational domain, J is the Jacobian of the transformation from Cartesian to computational domain ($J = x_\eta y_\xi - x_\xi y_\eta$), and P and Q are source terms that provide control over internal mesh spacing. Pointwise also employs various methods of hyperbolic extrusion in order to generate smooth three dimensional volume meshes. Simple normal extrusion is often sufficient for generating three-dimensional blunt-body topologies.

2.2.1 Work-flow

The process for creating a blunt-body mesh for an optimized heat shield is as follows. First, a Matlab script is used to generate the two profiles (axial and base cross-section) defined in Section 1.2.1 based on the geometric parameters given by the optimizer. These profiles are fed into a computer aided drafting (CAD) software package, called Rhino.[59] Here, the axial profile is rail revolved around the base cross section to create the full three-dimensional surface. This surface is exported in ".iges" format to be read into Pointwise as a database. This database is crucial as it allows for grid elements to be resized without losing important geometric information. A surface grid is created using this database as a reference, and it is sized and broken down into blocks depending on the needs of the given problem. Once the surface grid is completed, the elliptical solver is run to a desired smoothness using whatever control functions provide the best solution for the given geometry. Finally, a volume is extruded from the surface hyperbolically, with user prescribed boundary conditions and spacing, to form the grid to be exported to DPLR (in Plot3D format).

2.2.2 DPLR-specific Grid Generation Concerns

There are certain known issues that need to be carefully considered when crafting a blunt-body topology in order to prevent spurious results in DPLR. First, a geometry created by simply sweeping an axial profile around the central axis of a base cross section will produce a singularity at the nose of the resulting vehicle. This singularity may introduce unwanted errors into DPLR (a finite volume solver) as cells extruded from that point will have vanishing volume. In order to remove this singularity, all grids are patched elliptically in the nose region as shown in Figure 2.4. Also, in order to prevent poor shock capturing, all grids use finer spacing in highly curved areas (i.e. shoulder regions) as shown in figure 2.5. Finally, DPLR requires a sufficiently small body normal spacing near the wall in order for the hypersonic boundary layer to be captured. To this end, all meshes have 80 body normal points with a near wall spacing of 1.0 x 10^{-6} m.

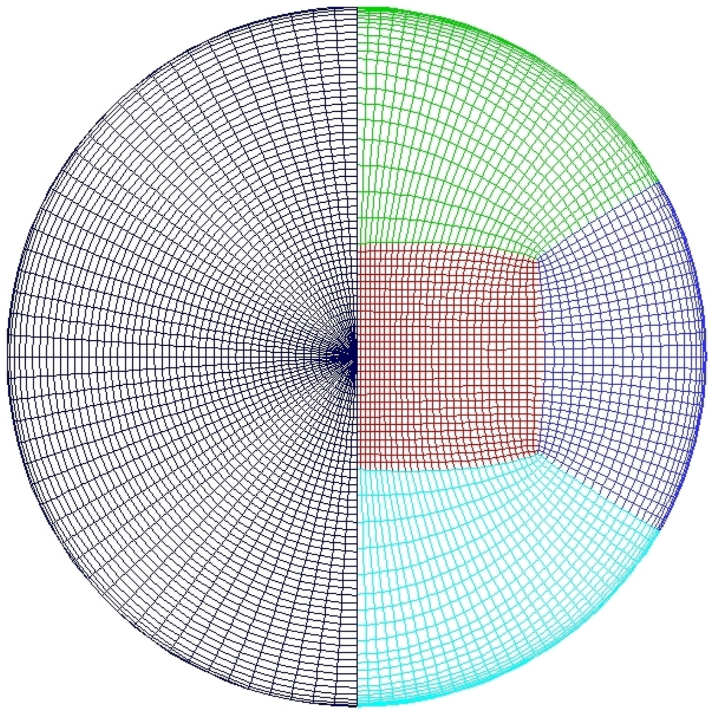

Figure 2.4: Nose patching as shown on the Apollo heat-shield

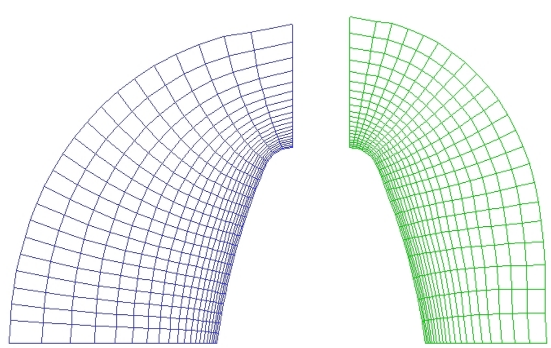

Figure 2.5: Edge spacing for the Apollo heat-shield

2.3 Shock Layer Radiation Solver

As DPLR lacks a method for internally calculating shock layer radiation, an external code is used to calculate the influence of the radiating flow field on a given a blunt-body. In this work, the Nonequilibrium Air Radiation (NEQAIR)[60] code is used. Radiation is only calculated in an uncoupled sense, in that results from NEQAIR are not fed back into DPLR. Essentially, radiation is calculated using only the fully developed solution from DPLR, which is equivalent to applying an optically thin assumption, in that no radiation is absorbed by the shock layer itself. It is possible to loosely couple these two software packages, via the radiation term in the conservation of energy equations as in the work by Pace[61] for axisymmetric test cases. This procedure involves iteratively creating new radiation solutions based on DPLR solutions updated with NEQAIR data. Full three dimensional cases using this approach can be incredibly costly; and, since the work of Johnson presents radiation and convection in an uncoupled sense, it is reasonable, for the sake of an apples-to-apples comparison, to do the same here.

2.3.1 Radiation Model

NEQAIR works by solving the radiative transport equation (RTE), given by:[38]

$$\frac{dI}{ds} = \epsilon - k'I \tag{2.19}$$

where I is a radiative intensity, ϵ and k' are emission and absorption coefficients respectively, and s is path known as a line-of-sight. To compute these coefficients, NEQAIR uses spontaneous emission, absorption, and stimulated emissions due to changes in energy states computed along a line-of-sight for every chemical species present. Bound-free and free-free radiation is also considered.[60] To determine the electronic state distribution, the quasi-steady state method of Park[38] is used, which considers electron impact excitation, de-excitation, and recombination in forming a model for the population. The solution of the radiative transport equation is vastly simplified, within NEQAIR, by applying the tangent-slab approximation. This model essentially makes the problem one-dimensional by assuming the radiating shock layer to be an infinitely long slab of radiating gas parallel to the body at a specified point. As such, emission and absorption can be neglected in the body parallel direction, leaving only the body normal (line of sight) direction upon which to integrate the intensities in the RTE. This model produces heating estimates that are 5-15% greater that what would be predicted by models that include surface curvature,[62] with the advantage of significant cost savings.

2.3.2 Work-flow

A NEQAIR solution is generated as follows. First, species concentrations and temperatures are extracted for the final volume mesh of a converged blunt-body solution using the built in post-processor in DPLR. Then lines-of-sight, discretized to a set number points, are created linearly from surface nodes to the outer boundary of the volume grid. Thermodynamic properties are interpolated from the converged DPLR solution onto corresponding points along these lines-of-sight. Example lines-of-sight are shown in Figure 2.6, generated for the Apollo heat shield. Here, 2,667 lines of sight are needed to cover the part of the vehicle's surface needed for the simulation (symmetry dictates that only half of the heat shield is needed). Finally, NEQAIR is run to integrate the transport equation, along each line of sight, to calculate the radiative heat flux at the originating surface node point due to radiative phenomena. For example, the topology in Figure 2.6 needs 2,667 separate invocations of NEQAIR to form a complete solution.

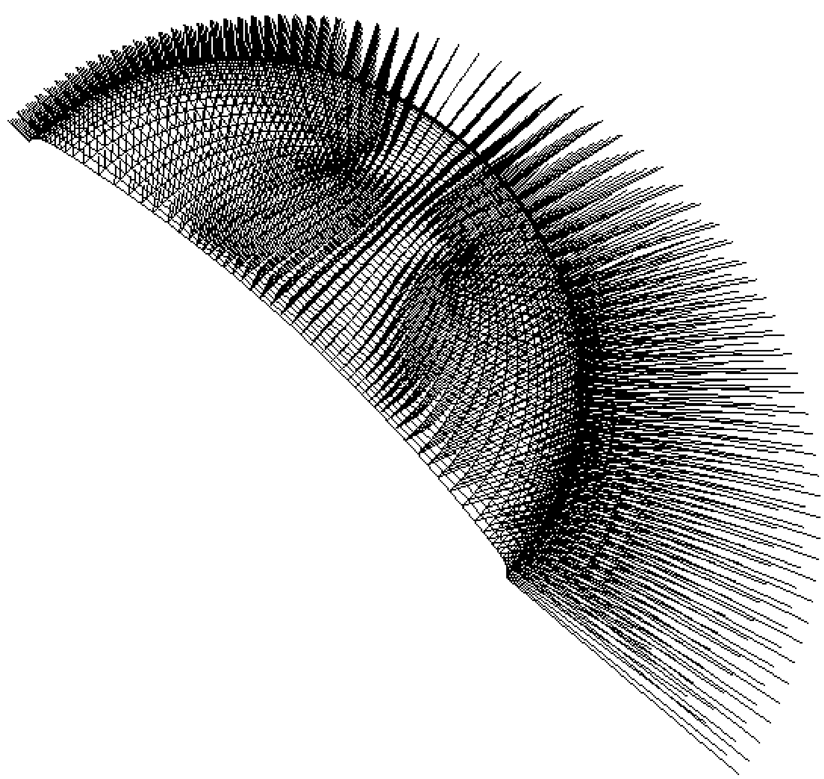

Figure 2.6: Lines-of-sight for an Apollo heat-shied

2.4 Hardware

The above computational tools, namely DPLR and NEQAIR, need a supercomputing environment in which to conduct their simulations. Two separate platforms are used primarily in this work: the (1) *Skystreak* cluster at the University of Maryland and (2) the *Columbia* cluster at NASA Ames Research Center. *Skystreak* , upon which most DPLR simulations are run, is a Gentoo Linux based system that consists of 7 dual processor 32-bit AMD Opteron nodes and 7 dual processor 64-bit Opteron nodes. This setup allows for a maximum 14 computational nodes per problem; and, in turn, DPLR solutions require, in general, 840 to 4360 CPU hours to reach final convergence (after multiple individual runs of DPLR). *Skystreak* uses the PathScale[48] suite for Fortran compiling and OpenMPI[49] is for parallelization.

The *Columbia* supercomputer, used for NEQAIR simulations and some DPLR grid resolution cases, is capable of 88.88 teraflops per seconds using 13,312 total computational cores and a SUSE Linux operating system. It is made of 17 Altix 3700 (512 cores each) nodes and 4 Altix 4700 nodes (3584 total cores) nodes. Intel Fortran[50] and OpenMPI form the compilation environment on *Columbia*. Typical NEQAIR runs using this cluster take approximately 15 minutes per line of sight, while DPLR solutions run on the order of what is experienced on *Skystreak* with the bonus that more processors can be expended on a given problem.

Chapter 3

Apollo 4 Benchmarking

This chapter explores benchmark DPLR solutions using the Apollo heat-shield at Apollo 4 (AS-501)[36,63] peak heating conditions in order to better understand potential issues that may be encountered with DPLR using more sophisticated shapes. To that end, the baseline Apollo heat shield torus is altered parametrically to fully comprehend the effects of certain geometric features, particularly edge radius, since shapes generated using the procedure outlined in Chapter 1 do not posses this attribute.

3.1 Baseline Geometry and Design Point

The baseline Block 1 Apollo command module geometry is shown in Figure 3.1. The forebody of the Apollo command module during re-entry, or the portion of the vehicle that is composed of the heatshield, is a 23° half-angle spherical segment blended into a torus with radius $R_T = 0.196$ m that extends for 133.9°. The afterbody is a 33° conical frustum with a cylindrical cap (for the purposes of this work, the outer mold line of the Apollo capsule is assumed to posses a spherical cap with radius $R = 0.231$ m). For basic stability comparisons, the center of gravity is taken at, with respect to the nose of the vehicle, at $x_{cg} = 1.35$ m, $y_{cg} = 0.00$ m, $z_{cg} = -0.137$ m, consistent with what was used for wind-tunnel tests.[64]

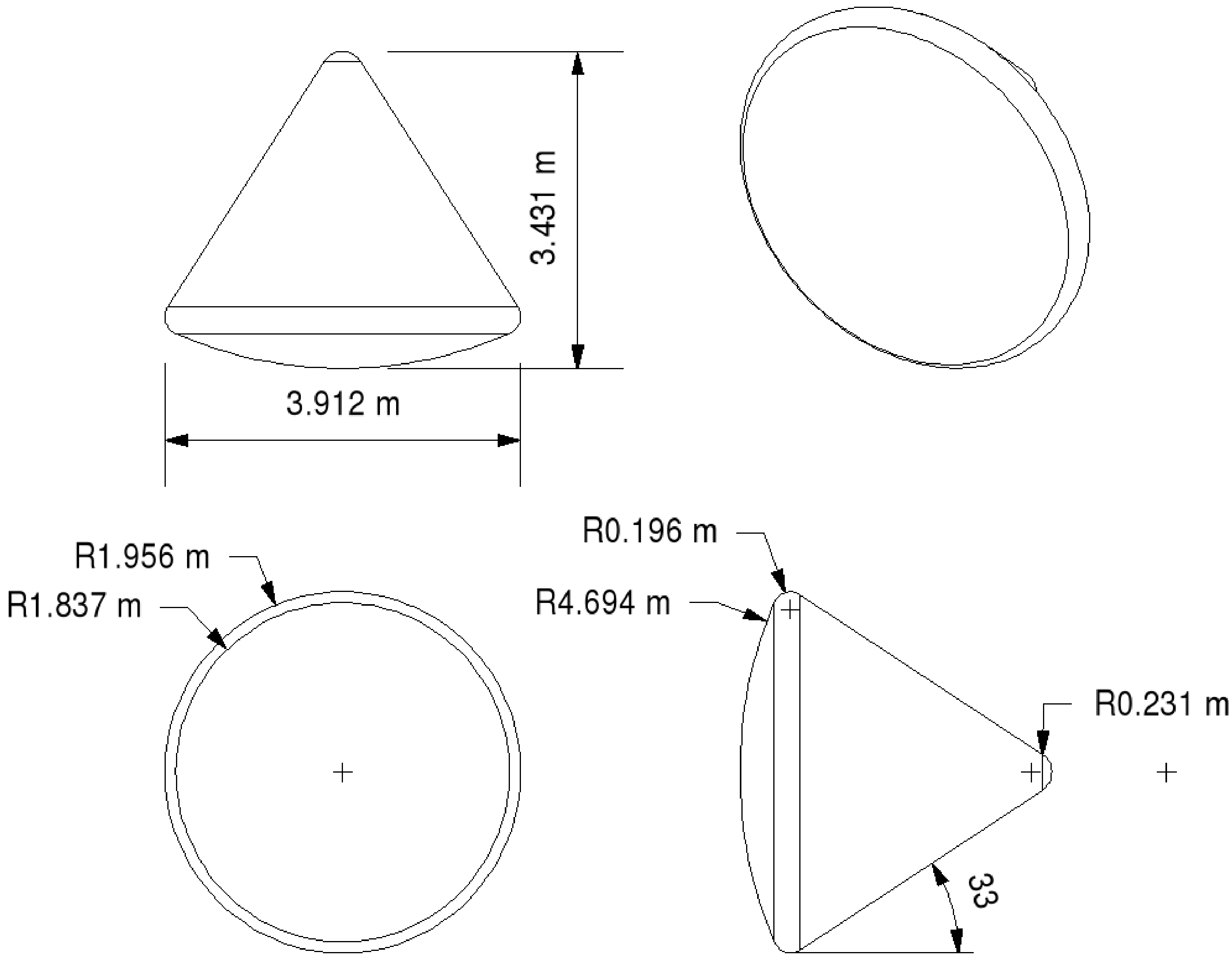

Figure 3.1: Apollo command module dimensions

.

For computational purposes, a four-block singularity free mesh with 195,840 grid cells (80 points body normal) is used as shown in Figure 3.2. The grid consists of the Apollo heat-shield cut off at its widest extent, retaining only the forebody and neglecting everything in the afterbody. Because this geometry, and all subsequent geometries considered, is symmetric about the x-y plane, only half the heat shield needs to be included computationally, thus saving on computational costs. The baseline DPLR simulations of this mesh are conducted at Apollo 4 peak heating conditions,[63] experienced at an altitude of 61 km, $M_\infty = 32.8$, and $\alpha = -25°$.

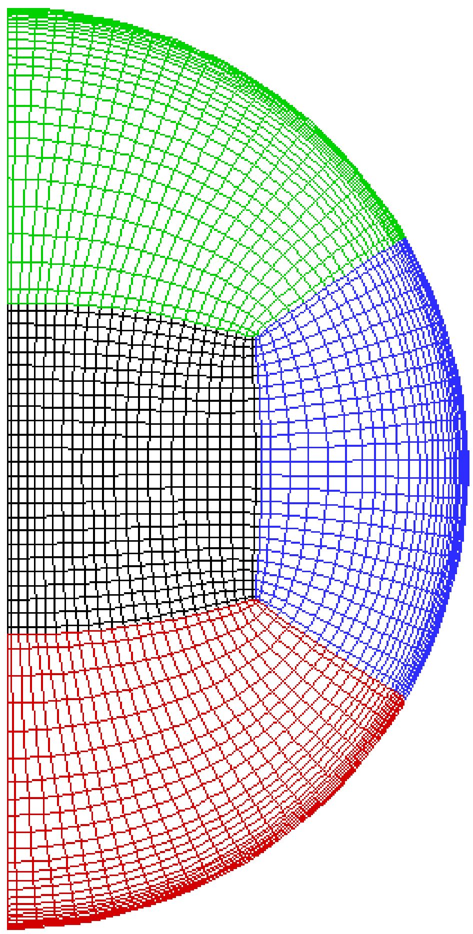

(a) Surface

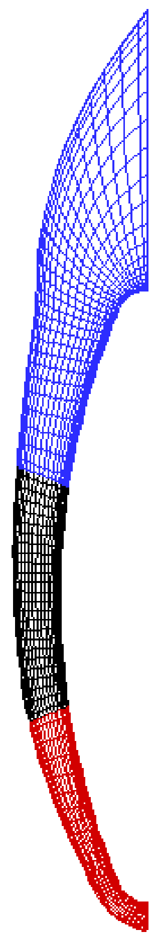

(b) Symmetry Plane (every other point)

Figure 3.2: Apollo heat shield CFD mesh

3.2 Baseline DPLR Results

Figure 3.3 shows Mach contours on the symmetry plane and pressure contours on the surface for the baseline Apollo 4 case. Lift and drag coefficients are calculated as 0.465 and 1.220 respectively, yielding an L/D ratio of 0.381 which is very close to the ratio of 0.375 predicted by flight data[65] at this particular Mach number. Using the center of mass defined above, the moment coefficient, $C_{m,cg}$, is 0.016 which matches well with high speed wind tunnel data.[64] Figure 3.4 shows the total wall heat flux on the vehicle's surface along its plane of symmetry. Peak convective heating occurs on the windward (the part of the vehicle pointing into the wind when at angle of attack) heat shield edge, away from the stagnation point with a value of approximately 371 W/cm^2, 1.68 times the stagnation point value. This result is consistent with a combination of the observation by Lee and Goodrich[36] that the maximum convective heat flux, at zero angle of attack, is 60% larger than at the stagnation point and the 1.06 correction suggested by Bertin[8] to account for sonic line movement when the vehicle is pitched. Table 3.1 shows a comparison of the present calculated convective heating rates with past work. The lower-order approach underestimates computational solutions by 30% for both peak and stagnation point convective heat flux. These under-predicted values by the lower-order method compared to DPLR solutions can be attributed to the failure of the later approach to account for boundary layer blowing. In fact, the classic Fay and Riddell[15] solution, which does account for boundary layer physics, as calculated by Park[66] is almost identical to the DPLR result. Still, for those solutions in which radiation is coupled to the convective heat fluxes, estimates over-predict DPLR solutions by up to 65%.

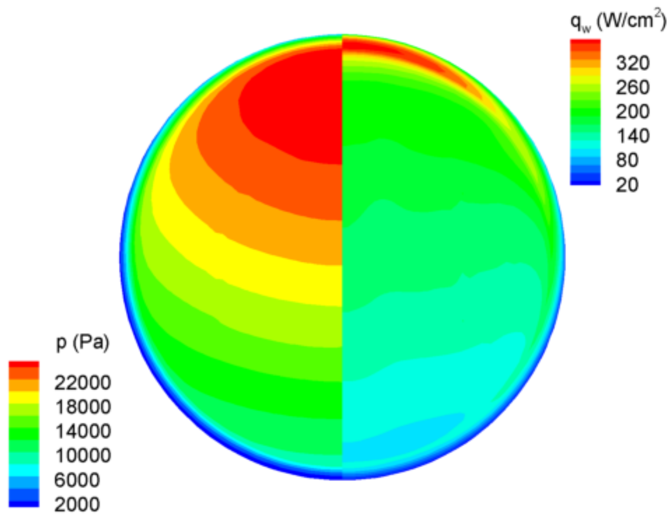

(a) Surface

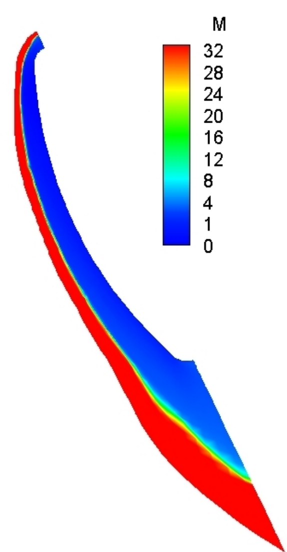

(b) Symmetry Plane

Figure 3.3: Pressure/convective heating contours on surface and Mach contours in symmetry plane for Apollo 4 at peak heating conditions

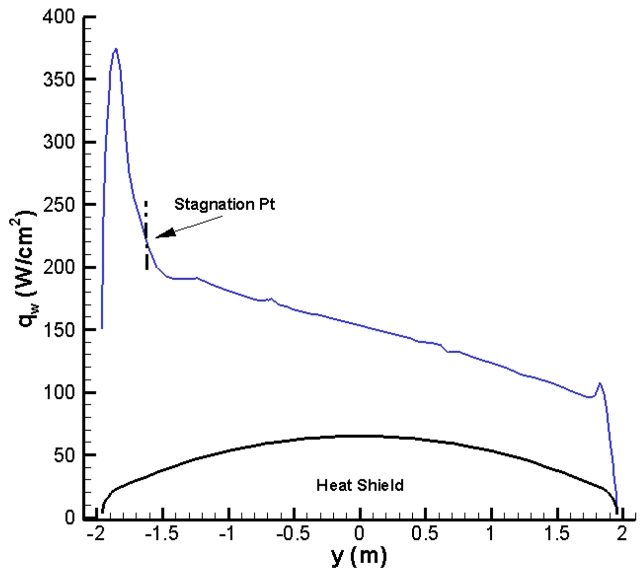

Figure 3.4: Symmetry line heating profile for Apollo 4 at peak heating conditions

Table 3.1: Apollo 4 peak and stagnation point convective heating

Author	$q_{max,conv}$(W/cm^2)	%Diff	$q_{s,conv}$(W/cm^2)	%Diff
Present work	371	-	221	-
Johnson et al.[2]	260	-29.9	154	-30.3
Pavlovsky and Leger[67]	266[a]	-28.3	-	-
Fay and Riddell[15]	-	-	230	4.1
Park[66]	-	-	363	64.3
Curry and Stephens[68]	-	-	339	53.4
Bartlett et al.[69]	-	-	289	30.8
Ried et al.[21]	-	-	227	2.7

[a] After subtracting q_{rad} from Tauber and Sutton[17]

At high entry velocities, shock layer radiation becomes significant for blunt bodies due to ionization and dissociation;[69] and, as of now, DPLR has only limited internal methods for calculating the heating impact from the shock layer. Since the lower-order approach does not couple convective and radiative heat transfer, comparing the convective heat flux is an informational point of comparison between the two aerothermodynamic calculations, yet, if accuracy is required, the present solutions would need to be coupled to an external shock layer radiation code. The true nature of the coupling between radiative and convective heat transfer (as evidenced by the spread in estimates by Park, Bartlett et al., and Reid et al.) are not well understood for these high temperature environments; as such, it is reasonable to leave the two heating regimes uncoupled until, at least, more flight data is accrued and better correlations are derived. Essentially, though DPLR convective heat transfer results are not entirely accurate (in that shock layer radiation is neglected), the observation that peak heating is not at the stagnation point, and is, in fact, significantly higher shows that computational solution yields results that are, in the least, qualitatively significant.

3.3 Grid Resolution

Solutions for the Apollo heat shield at Apollo 4 (AS-501) peak heating conditions, experienced at an altitude of 61 km, $M_\infty = 32.8$ at $\alpha = -25°$, are compiled on volume meshes with 40, 60, 80, and 160 points in the body normal direction. The 80 point solution is the baseline case used in benchmark DPLR runs. Table 3.2

shows point aerothermodynamic metrics for all these cases, and percent differences are referenced to the highest resolution case (160 points). The lowest resolution case shows the greatest disparity with respect to the finer case, especially, with regards to peak convective heat flux. Here the difference is greater than 10% whereas adding just 20 more body normal points drops the disparity below 1%. Both the 80 point case and 60 point case display errors less than 1% for all aerothermodynamic metrics compared with the finest resolution case; however, not all heat shields have a simple axisymmetric shape like Apollo, nor do these point metrics accurately portray what is happening on the entire surface.

Figure 3.5 shows the convective heat flux on the symmetry plane for all four grid resolution cases. Clearly, the lowest resolution case shows the most erroneous predictions, especially on the leeward side of the vehicle (the portion of the heat shield that points away from the wind when pitched). One interesting note is that all solutions, even the sparsest mesh case, converge at the stagnation point convective heat flux. The 60 and 80 point cases are nearly identical, but with the finer solution portraying slightly better results on the leeward side of the vehicle. In this instance, results reported from an Apollo mesh with 60 points in the body normal would be nearly identical to the baseline; however, since not all heat shields studied here are simple shapes, a slightly larger resolution is a safer choice. In that regard, choosing 80 points for the body normal direction for all heat shield meshes is a prudent one.

Table 3.2: Apollo grid resolution aerothrmodynamics

Parameter	Pts (body normal) 40	60	80*	160
C_L	0.457	0.463	0.463	0.467
$\Delta(\%)$	-2.141	0.463	0.463	-
C_D	1.20	1.22	1.22	1.23
$\Delta(\%)$	-2.44	-0.81	-0.81	
L/D	0.3808	0.3795	0.3795	0.3797
$\Delta(\%)$	0.31	-0.04	-0.04	-
$C_{m,cg}$	0.0159	0.0163	0.0162	0.0161
$\Delta(\%)$	-1.24	1.24	0.62	-
$q_{conv,max}$ (W/cm^2)	416.5	373.4	373.8	370.5
$\Delta(\%)$	12.42	0.78	0.89	-

*Baseline dimension for all DPLR solutions

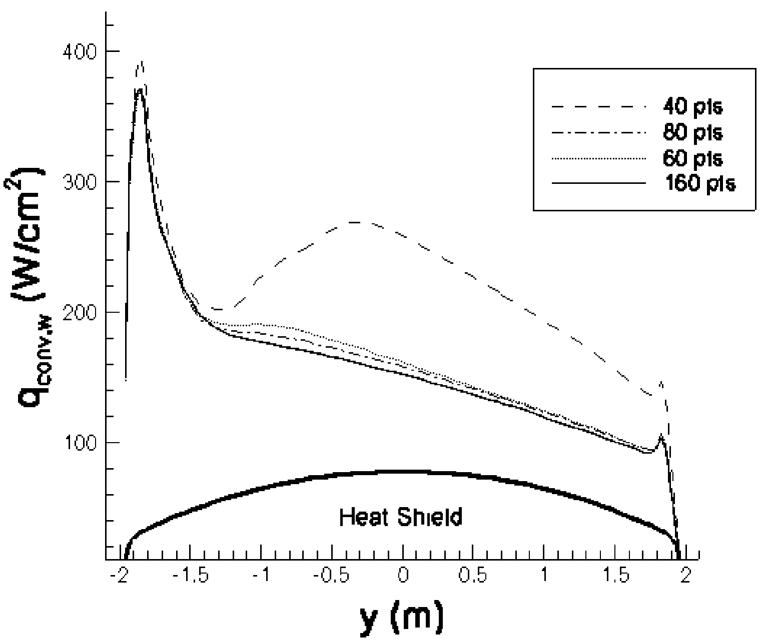

Figure 3.5: Symmetry plane convective heat flux for Apollo heat shield grid resolution study

3.4 Baseline Radiation Results

NEQAIR surface radiative heating results generated from the baseline DPLR solution are shown in Figure 3.6. Peak radiative heating occurs slightly leeward of the stagnation point at a value of 217 W/cm^2. Stagnation point radiative heating is only slightly lower at 204 W/cm^2. Table 3.3 shows a comparison of the present calculated stagnation point radiative heating rates with past work. The lower-order method over estimates NEQAIR stagnation point radiative heat flux by 16%; however, this overestimation combined with the under-predicted convective heat flux yields a total stagnation point heat flux (391 W/cm^2) that differs from the combined DPLR/NEQAIR solution (425 W/cm^2) by only 8%. Total stagnation point heat flux agrees mostly well (within 25%) with past results, while stagnation point radiative heat flux agrees to within 20% for most cases. The values that are vastly greater than the NEQAIR solution use models that do not account for energy dissipation in the boundary layer, resulting in expectedly greater estimates. It should be noted that for, convective heating, past work resulted in higher values, while that trend is the opposite for radiative heating. Combining these two phenomena explains the relative accuracy of the combined DPLR/NEQAIR approach to predict total stagnation point heat flux. This implies that the effect of coupling would be to lower radiative heat flux, while increasing convective heat flux, creating only a negligible difference in the sum. Figure 3.7 shows the convective, radiative, and total heat flux along the symmetry plane. The maximum overall heat flux occurs at the location of peak convective heating (windward of the stagnation point) at a value 507 W/cm^2. This prediction agrees very well with the 480 W/cm^2 estimation by Pavlovsky and Leger.[67]

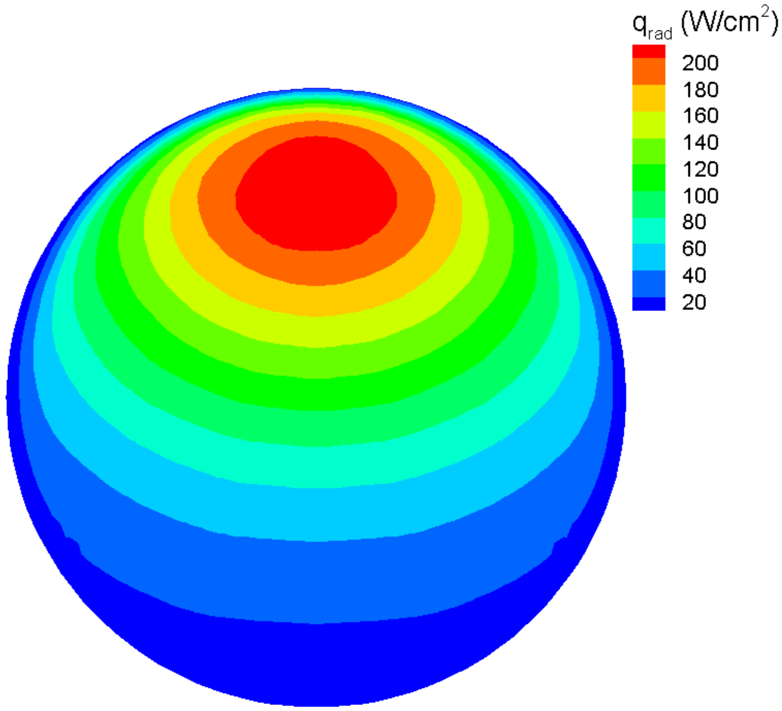

Figure 3.6: Surface radiative heat flux contours for Apollo heat shield at Apollo 4 peak heating conditions

Table 3.3: Apollo 4 stagnation point radiative and total heating

Author	$q_{s,rad}$(W/cm^2)	%Diff	$q_{s,tot}$(W/cm^2)	%Diff
Present work	204	-	425	-
Johnson et al.[2]	237	16.18	391	-8.00
Flight data[a]	167	-18.1373	-	-
Curry and Stephens[68]	176	-13.73	515	21.18
Bartlett et al.[69]	193	-5.39	482	13.41
Ried et al.[21]	300	47.06	527	24.00
Park 2001[70]	507	148.53	731	72.00
Park 2004[66]	168	-17.65	531	24.94
LORAN[71]	320	56.86	-	-
Balakrishnan et al.[72]	184	-9.80	-	-

[a] Calculated using measured peak intensity by Park[70]

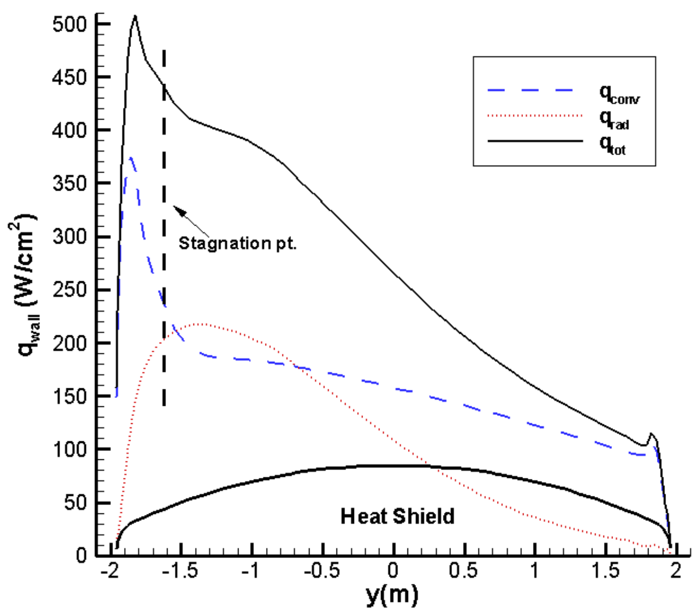

Figure 3.7: Convective, radiative, and total heat flux on symmetry plane for Apollo heat shield at Apollo 4 peak heating conditions

3.5 Torus Radius

As previously stated, the forebody of the Apollo command module during reentry is made up of a 23° half-angle spherical segment blended into a torus with radius $R_T = 0.196$ m that extends for 133.9° until the conical frustum afterbody begins. This torus, only to the capsules widest extent, is included in the baseline benchmark results for Apollo 4; however, the geometries generated by the optimization process do not include these regions of curvature. What role this torus plays on a blunt-body's flow field is detailed in the following subsections through parametric studies of the baseline Apollo geometry with various different torus designs.

3.5.1 Torus Extent

To further understand the effects the extent of this torus has on the aerothermodynamics of a blunt-body capsule, the baseline Apollo 4 case (referred to here as a half torus) is compared to solutions on meshes that include the entire torus (expanded until the beginning of the conical frustum afterbody) and that include no torus at all. Figure 3.8 shows a comparison of the wall heat flux on the plane of symmetry for all three cases. Only minor differences can be seen when any part of the torus is considered; however, the results obtained without a torus show a singularity at the edges of the heat shield and a local maximum in a very different location than the other cases. Since local convective heating is proportional to the reciprocal of the square root of the local radius of curvature, this asymptotically high heating at the edge of the heat shield is not surprising; however, another explanation for these spurious results can be seen by examining the sonic line of the three cases (Figure 3.9).

For cases that include the torus, regions of subsonic flow spill over to the torus on the windward side of the heat shield before expanding back to supersonic. When the torus is absent, flow at the exit of the grid near the windward edge is subsonic, violating the DPLR boundary condition of a supersonic exit. This numerical limitation can be solved, without introducing some curvature at the edges, by adding an afterbody to the heat shield. Still, by adding a simple, conical afterbody (thereby retaining the infinitesimally small radius of curvature at the heat shield edge) without including the wake, there is still the possibility of subsonic flow at the leeward boundaries of the heat shield. Essentially, this means that the afterbody must be a fully closed body and the topology must be extended to include the wake, which will greatly increase the computational cost incurred. To avoid these sky-rocketing costs, some manner of curvature at the edge of an optimized heat shield must be added while taking care to not drastically change the original geometry.

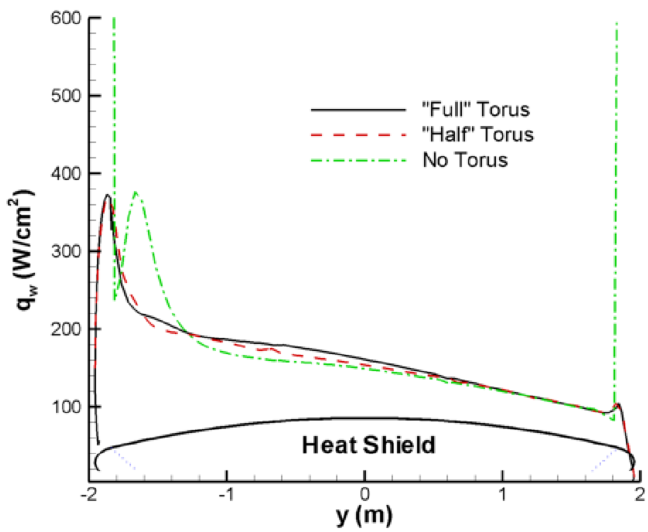

Figure 3.8: Symmetry convective heat flux comparison of Apollo 4 peak heating case for three different torus extents

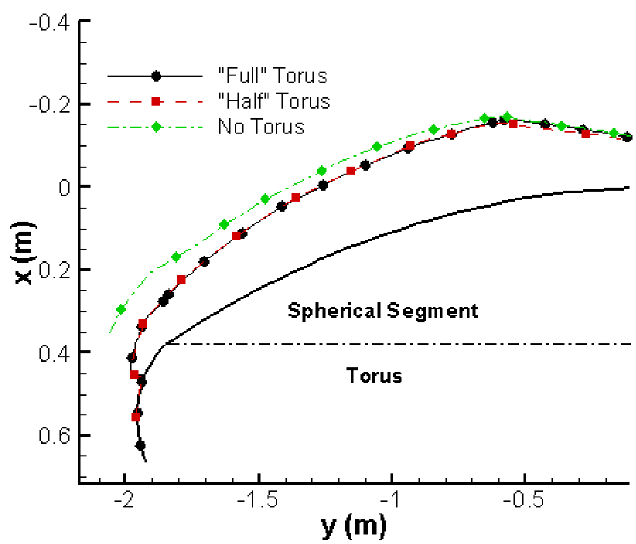

Figure 3.9: Sonic line comparison of Apollo 4 peak heating case for three different torus extents

3.5.2 Torus Size

Though some finite curvature is required to perform CFD with DPLR on a blunt-body heat shield, it was unclear what impact the exact amount of edge curvature or bluntness will have on the aerothermodyamics of a heat shield. As such, Apollo forebodies with various multiples of the baseline torus radius (up to 5xR_T) are compared to the benchmark Apollo results calculated using Apollo 4 peak heating altitude and velocity at the dominant entry angle of attack, $\alpha = -25°$, and at $\alpha = -15°$. The lower magnitude angle of attack case is included to explore edge radius effects on a blunt-body for which the stagnation point is not near the vehicle's edge. Figure 3.10 shows the maximum heat flux on the symmetry plane for all topologies at both angles of attack. Both curves show that heat flux decreases in a power law sense with increasing torus radius, which should be the case since convective heat transfer is function of the inverse of the square of the local radius of curvature. However, when the stagnation point is further from the vehicles windward edge (i.e. for $\alpha = -15°$) the heat flux decreases at a slightly slower rate than it does at a higher angle of attack. Since the regions of higher temperature and pressure occur farther away from the torus at lower angles of attack, it is reasonable to assume that changing the torus radius will have a lesser impact on the heat flux in this case. For all torus sizes, the $\alpha = -15°$ case has lower peak convective heat flux. This phenomena can be attributed to the lower velocity gradients experienced at the edge of the heat shield at that particular angle of attack.

Figure 3.11 shows the resulting lift to drag ratio for all cases of torus radius for both considered angles of attack, -15°and -25°. The dashed lines show the predicted Newtonian L/D for each respective angle of attack. When torus radius is small, the DPLR calculated L/D approaches this predicted value. Since the Newtonian values are calculated with no radius of curvature at the edge, this trend is understandable. For both angles of attack, the L/D decreases linearly; however the lift to drag ratio for the higher angle of attack set of solutions decreases at a faster rate. This occurs due to peak pressures shifting toward the center of the heat shield rather than being closer to the highly curved edges. Figure 3.12 is a plot of moment coefficient versus torus size for both considered angles of attack. The center of gravity may change with increasing torus radius if more heat shield material is added unevenly to the windward edge to counter higher heating; but, for all cases studied here, the center of gravity is considered fixed. $C_{m,cg}$ increases linearly with torus radius for both angles of attack due to the increased moment arm induced by the larger tori. Also, note, that for a larger edge radius ($\approx 5xR_T$), $\alpha = -15°$ is nearly the trim angle of attack.

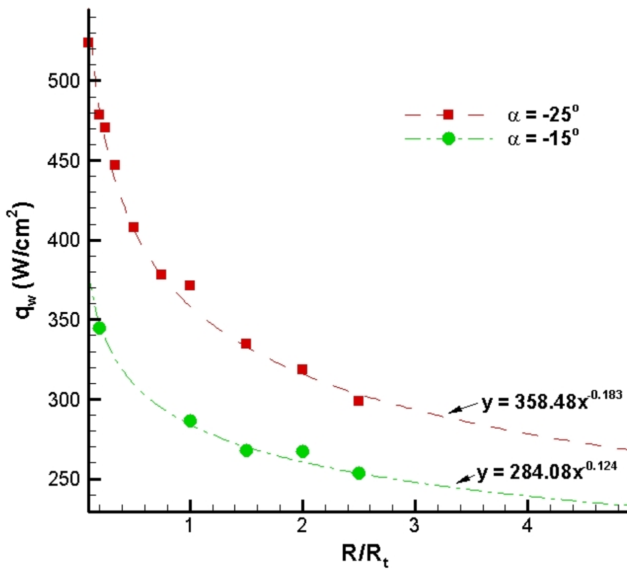

Figure 3.10: Peak convective heat fluxes for Apollo heat shield at Apollo 4 peak heating conditions for two angles of attack

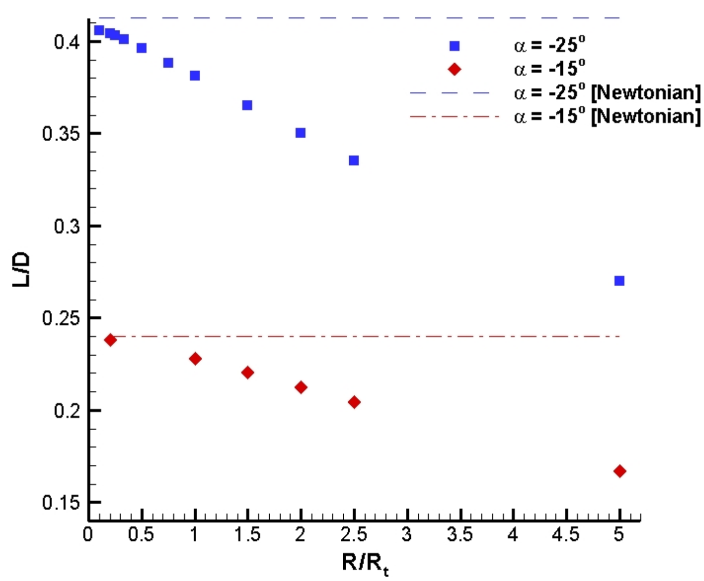

Figure 3.11: Lift to drag ratios versus torus radius for Apollo heat shield at two angles of attack

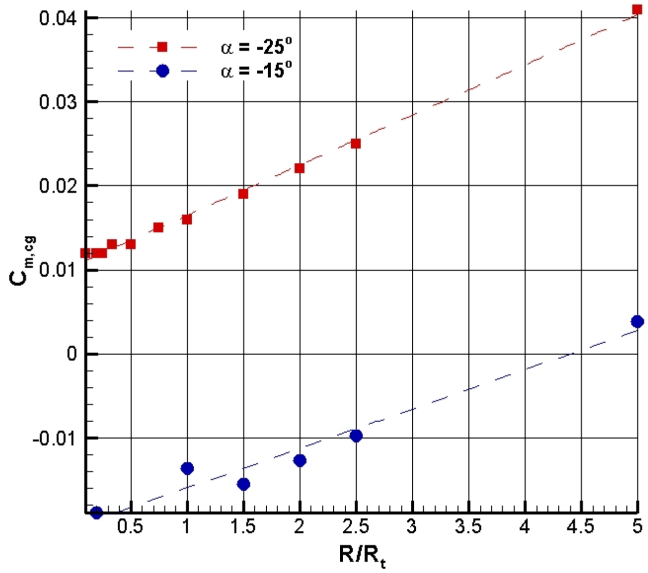

Figure 3.12: Moment coefficient for Apollo heat shield at different angles of attack

3.5.3 Further Considerations

Edge curvature plays a significant role in determining the resulting aerothermodynamics of a vehicle. Mission requirements and hardware concerns (i.e. launch vehicle mating) will often determine what the afterbody of a vehicle will look like and how it will attach to the heat shield. Since these concerns are beyond the scope of this work, a fixed torus matching that of the Apollo capsule ($R_T = 0.196$ m) is blended to all blunt-body optimized designs for further study. However, for elliptical bases, scaling effects need to be considered when deciding upon which axis to apply the torus. Figure 3.13 shows an elliptical heat shield (to be discussed in Chapter 4) with the torus applied on the semi-major axis on the left and on the semi-minor axis on the right. Although applying the curvature along the shorter side first generates a larger surface area, the peak heat flux is significantly less than if the torus were first applied on the longer side. These lower heating rates would, in all likelihood, require cheaper materials to dissipate. As such, all elliptical and blunt designs to be studied here will have the torus added to the axial profile along the semi-minor axis before being swept around the base cross-section.

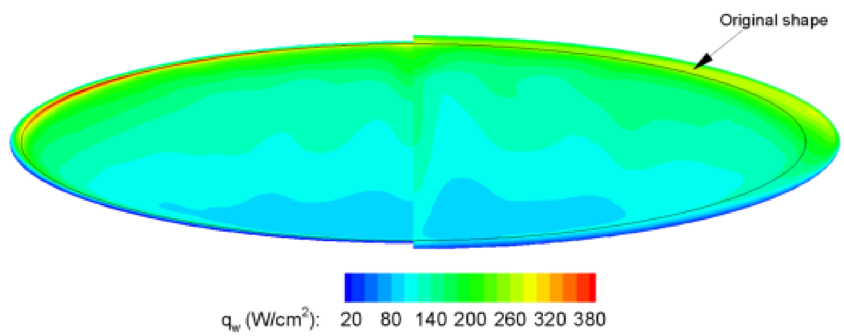

Figure 3.13: Convective heat flux on an elliptical heat shield for two different methods of torus generation

3.6 Computational Cost Summary

Table 3.4 shows a summary of grid sizes, iteration counts, and computational time for all Apollo derived cases considered here. There is no consistency in the time it takes to arrive at a final solution, since convergence occurs only at the user's satisfaction. That is, the solution is allowed to mature until the user deems the solution to have stabilized (usually by the time the L_2 norm of the residuals of a conserved variables is less than 10^{-8}). Still, no case took less than 390 CPU hours and 20,000 iterations for convergence. In fact, most cases needed more time to reach sufficient convergence. NEQAIR solutions were run using 2,667 lines of sight for the Apollo geometry. At 15 minutes per line of sight, the single uncoupled radiation solution needed 666.75 CPU hours to complete.

Table 3.4: Summary of computational cost for Apollo edge radius cases

R/RT	α	Grid Size (# cells)	Iterations	CPU Time (hrs)
0.100	-25°	197120	64400	1831.2
0.200	-25°	197120	77900	1594.46
0.200	-15°	197120	52500	987.84
0.250	-25°	191720	70000	1470.0
0.333	-25°	191720	46600	1470.0
0.500	-25°	203040	66000	1186.08
0.750	-25°	203040	85300	2286.62
1.000	-25°	195840	20400	392.84
1.000[a]	-25°	98560	108000	1099.99
1.000[a]	-25°	147840	37000	604.33
1.000[a]	-25°	394240	55500	2123.33
1.000	-15°	195840	42900	1524.46
1.500	-25°	205560	36800	735.0
1.500	-15°	205560	34000	692.16
2.000	-25°	205560	41700	976.08
2.000	-15°	205560	40700	1240.54
2.500	-25°	205560	38100	1034.46
2.500	-15°	205560	33600	738.92
5.000	-25°	205560	52300	1664.46
5.000	-15°	205560	31400	1065.54

[a]Grid resolution cases

Chapter 4

Slender Bodies: A High L/D Case

The n_2 parameter, from Equation 1.1, controls the sharpness of the base cross section for blunt-body heat shields of Johsnon, et al.[4,6] Optimized geometries have utilized a lower bound of 1.3 for this parameter along with a more slender profile to generate high L/D solutions; however, it is unclear as to how this sharpness will affect the off-stagnation point performance of these generated shapes. As such, a representative geometry, optimized for high L/D at Apollo 4 peak heating conditions, is explored in this chapter.

4.1 Baseline Geometry and Results

To study the full flow field of the high L/D shapes classified by Johnson, et al.[2,6] , DPLR solutions are obtained for a spherical segment heat shield optimized for maximum L/D at Apollo 4 peak heating conditions ($h_t = 61$ km, $M_\infty = 32.8$). The modified Newtonian approach predicted a lift to drag ratio of 1.24 and $q_{s,conv}$ of 240 W/cm^2 for an 89° spherical segment with $n_2 = 1.3$, $m = 4$, and $e = -0.968$ at $\alpha = 18°$. This shape (see Figure 4.1) has more of a "nosecone" like geometry in that it is more slender and eccentric than the Apollo heat shield. As such, edge radius effects would be expected to have less significant an impact on overall performance, since the velocity gradients at the boundaries are less steep than those for a more classical spherical segment blunt design. for this study a four block structured mesh with 236,440 grid cells is used as shown in Figure 4.2.

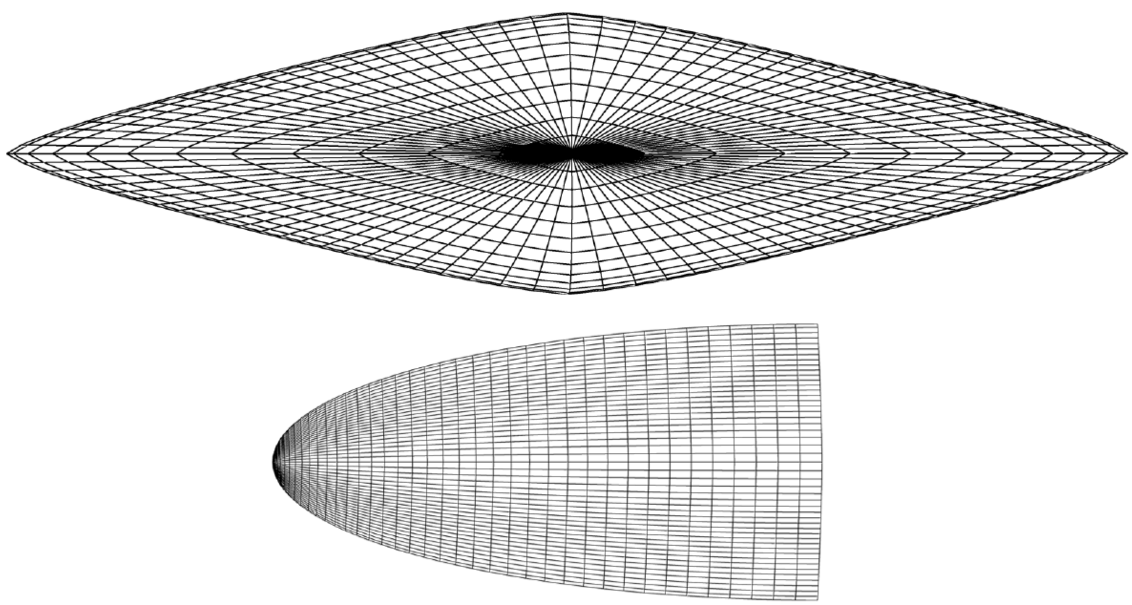

Figure 4.1: 89° spherical segment with $n_2 = 1.3$ optimized for maximum L/D

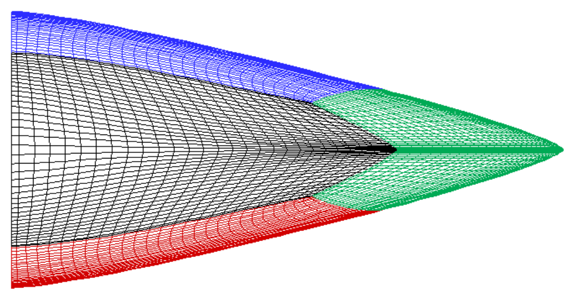

(a) Surface

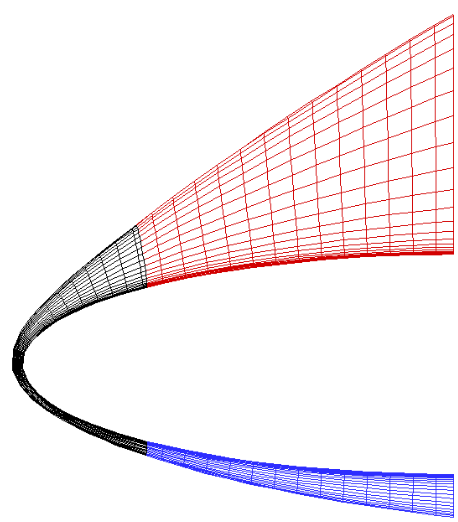

(b) Symmetry Plane (every other point)

Figure 4.2: mesh for 89° spherical segment optimized for maximum L/D

Figures 4.3 and 4.4 show surface heat flux and pressure contours as well as symmetry plane Mach and pressure contours respectively. Mach contours are very close to the vehicle's surface, resulting in a thinner shock layer for radiation than exists with a more blunt geometry (i.e. Apollo). DPLR solutions show $C_L = 0.795$ and $C_D = 0.711$, resulting in $L/D = 1.118$. The lower-order prediction for L/D is 11% higher than the CFD result. This difference is due, in most part, to the simpler method ignoring surface pressures in the shadow region ($\vec{V} \cdot \hat{n} \geq 0$) that may contribute to lift and drag. Still, this offset is not extreme; and, the predictions by the lower-order approach would still be useful in design studies.

Convective heating at the stagnation point is calculated as 430 W/cm^2. The low-order approach under-predicts this value by 44%, a larger discrepancy than was observed for Apollo 4. This difference implies that empirical correlations used for heating rates may not be ideally suited for elliptical base cross sections such as the one seen here. Peak heating occurs along the leading edge of the vehicle far away from the stagnation point at a value of approximately 980 W/cm^2. This value is 2.28 times higher than the DPLR calculated stagnation point heat transfer and 4.08 times greater than the low-order stagnation point prediction. Essentially, the edge of the parallelogram base cross section (controlled by the n_2 parameter) creates a sharp leading edge away from the nose near the edges of the heat shield, that generates what is almost an attached shock-wave at the point where highest convective heating is shown to occur. The heat flux is expectedly high in that area because there is little gas, in the shock layer, with which to dissipate the high temperatures created by the shock-wave. Because the lower-order approach only looks at the stagnation point for heating rates, it omits an area of adverse heating that may make the design infeasible. For future optimizations, a situation such as this one can be avoided by altering the optimization constraints in such a way that would prevent near attached shock-waves from forming on a generated heat shield.The simplest way to do this would be to raise the lower bound of the sharpness parameter, n_2 to 1.4 or 1.5.

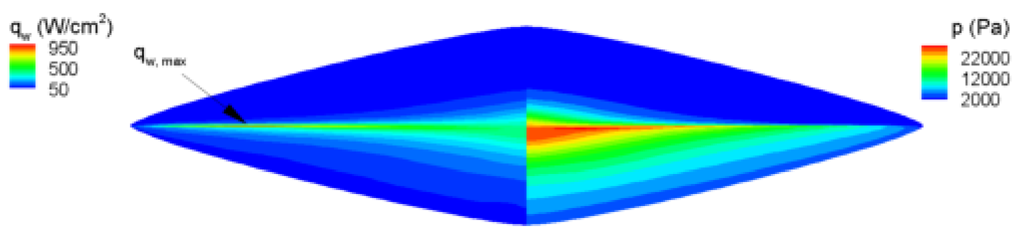

Figure 4.3: Surface convective heat flux and pressure contours for 89° spherical segment optimized for maximum L/D

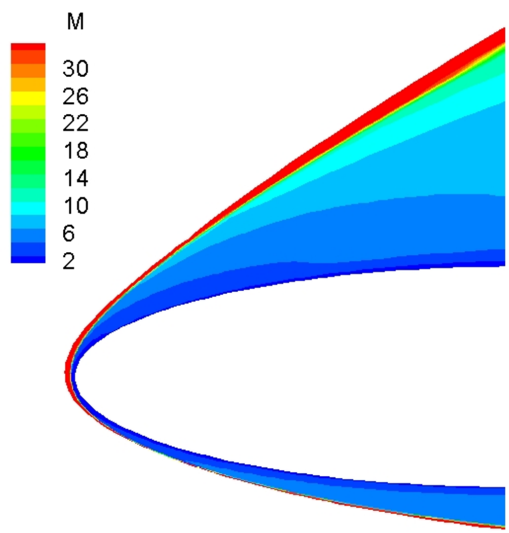

(a) Mach Number

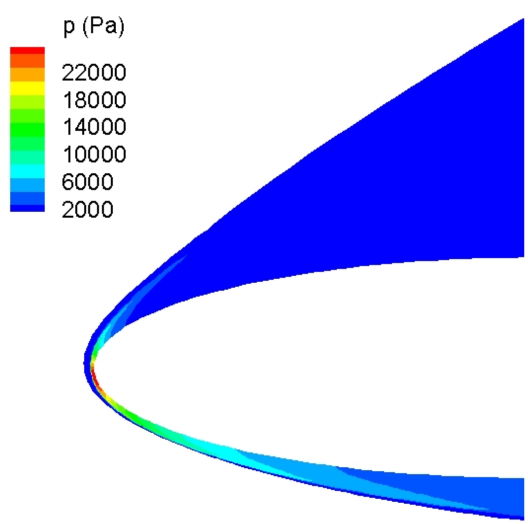

(b) Pressure

Figure 4.4: Symmetry plane contours for 89° spherical segment optimized for maximum L/D

4.2 Surface Grid Resolution

Furthermore, the impact of surface grid resolution on the resulting aerothermodynamics of the above slender heat shield is examined by comparing results from the representative high L/D shape (an 89° spherical segment with $n_2 = 1.3$, $m = 4$, and $e = -0.968$ at $\alpha = 18°$ at Apollo 4 peak heating freestream conditions) using a baseline surface grid (236,440 total cells) with one in which the number of points in both surface directions (i and j) are doubled (1,205,600 total cells). Table 4.1 shows the resulting aerothermodynamics of these two cases. The lower resolution case shows good agreement (within 1.5%) with the finer resolution solution for aerodynamic coefficients of lift and drag but shows a greater than 15% difference with respect to peak convective heating.

A closer examination of the surface convective heat flux of these two meshes (see Figure 4.5) shows a clearer picture of this disparity. In both cases, peak heating occurs at nearly the same position, on the leading edge away from the stagnation point, but the higher resolution solution shows a larger area of high heating around that point at values much higher than seen in the low resolution case. Likely, the greater number of points generates a shape that is sharper than geometrically possible with fewer points. In reality, a heat shield with this design would have a leading edge that would ablate, or burn up, as it experienced these high heat loads. Essentially, it would have an initial shape that is more like the fine mesh that would eventually become more like the sparser mesh over time. The lower point case is probably more artificially blunt than it is meant to be, if only the geometric parameters were considered, which causes heating rates to be reported lower. Still, nothing in these results conflicts with the above conclusion that an n_2 value of 1.3 allows for the possibility of extreme off-stagnation point heating rates that may reach or exceed material limits; in fact, they only underscore it.

Table 4.1: Aerothermodynamics for slender heat shield surface grid resolution study

Cells (Surface)	C_L	C_D	L/D	$q_{conv,max}$ (W/cm^2)
236,440	0.795	0.711	1.118	978.75
1,205,600	0.800	0.705	1.135	1173.2
Δ (%)	*-0.625*	*0.851*	*-1.464*	*-16.574*

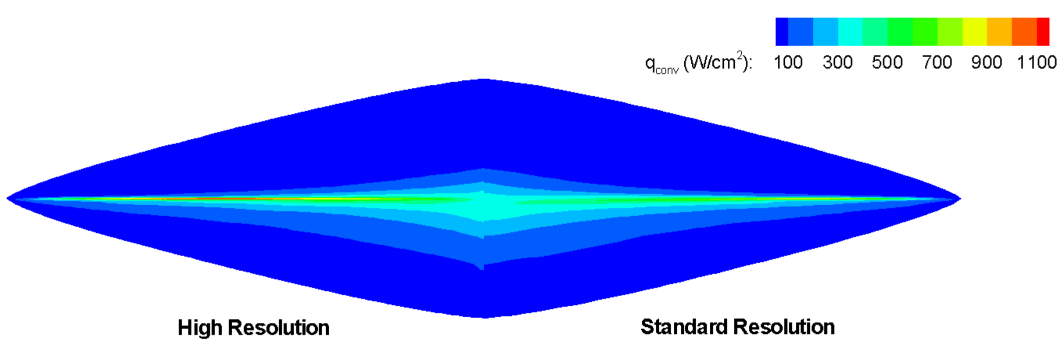

Figure 4.5: Surface convective heat flux for slender heat shield surface grid resolution study

4.3 Radiation

NEQAIR surface radiative heating results generated from the high L/D test case DPLR solution are shown in Figure 4.6. Peak radiative heating is 106 W/cm^2 and occurs at the stagnation point. The lower-order approach predicts stagnation point radiative heating as 190 W/cm^2, which is 79% higher than the NEQAIR result. This disparity is much greater than the 16% difference seen in the Apollo benchmarking case. As such, it is entirely possible that the assumptions used in applying the Tauber and Sutton model for radiative heating in the lower-order method may be incorrect. Likely, the relations used to calculation shock stand off distance, the most important factor in determining the radiative heating, do not account for elliptical geometries such as those with oblate stretching in the base cross-section seen here. Since these models are empirical in nature, this implies the necessity for further wind tunnel and flight tests to provide the data points needed in creating an approximation that has even greater physical basis.

Using the value of radiative heating calculated by NEQAIR, the total stagnation point heating is 536 W/cm^2. This result compares favorably to the lower-order prediction of 430 W/cm^2 (a -20% difference). In reality, the convective and radiative heating are drastically under-predicted and over-predicted by the lower-order method respectively when compared to the present computational approach. So, in essence, the errors introduced to the convective heat flux model by the elliptical cross section are canceled out by the errors in predicting true shock stand off distance by the radiative heating model. While certainly not intended, this inaccuracy in the underlying models generates overall results that are indeed accurate, and can be used effectively for first-pass design studies.

Not surprisingly, NEQAIR predicts little to no radiative heating on the leading edge of the vehicle at the location where maximum convective heat flux occurs. This result confirms the earlier assertion that the shock-wave must be very close to the body at that point. Essentially, because the shock layer is so small, there is very little high temperature gas necessary to radiate heat back to the vehicle's surface. Still, the peak convective flux is almost twice the total heating felt at the stagnation point and can not be ignored, as it nears design limits for the Orion CEV capsule.

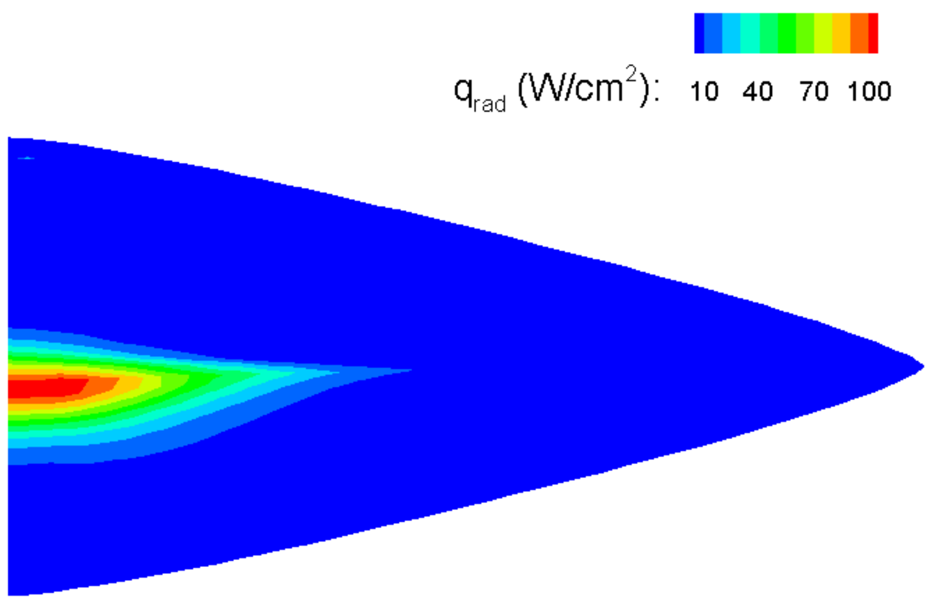

Figure 4.6: Surface radiative heat flux and pressure contours for 89° spherical segment optimized for maximum L/D

4.4 Changing Edge Sharpness

The effective edge sharpness of the high L/D example is further studied by comparing the baseline ($n_2 = 1.3$) case to other designs with the all same parameters except a different value of n_2. Figure 4.7 shows the peak heat fluxes for four different values of n_2, and it can be seen that heating decreases approximately with the inverse cube of the sharpness parameter. Essentially, by increasing the bluntness of the edge on the base cross section, large reductions in peak heat flux, when compared to the baseline ($n_2 = 1.3$), are obtained. Figure 4.8 shows the lift to drag ratios for the four cases of n_2 studied here. In all cases, the modified Newtonian solution over-predicts the calculated L/D by up to 10%. This discrepancy is caused by the lower-order method's consistent inability to capture reductions in lift do to pressures experienced on the body in the vehicle's shadow region, which are neglected by the modified Newtonian approach. This phenomenon is apparent in that the modified Newtonian approach predicts lift coefficients that are 2-10% more than the high fidelity model; however, the accuracy of the Modified Newtonian approach does improve as the base cross section becomes more elliptical ($n_2 \approx 2.0$). When the base is more like a parallelogram ($n_2 \approx 1.1$-1.3), the revolved surface will have a sharp leading edge blending into a blunt nose. A Newtonian solution is not as well suited for these sharp leading edges;[9] as such, the blunter edged solutions ($n_2 \approx 2.0$) should be more accurate.

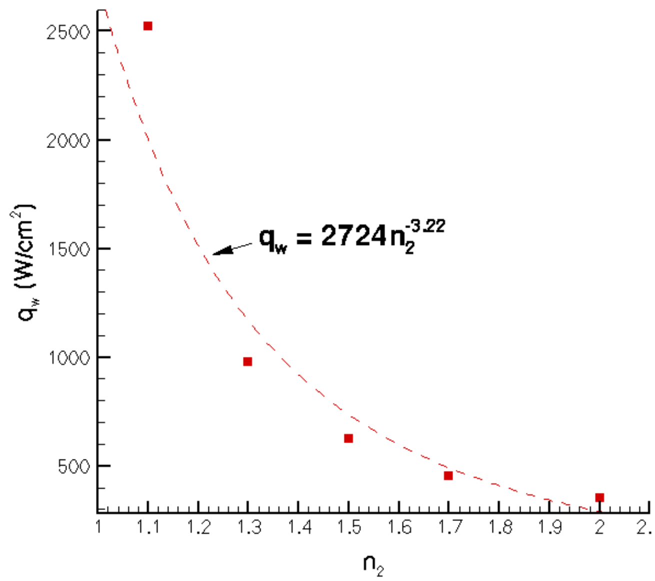

Figure 4.7: Maximum convective heat fluxes for 89° spherical segment with varying n_2 parameter

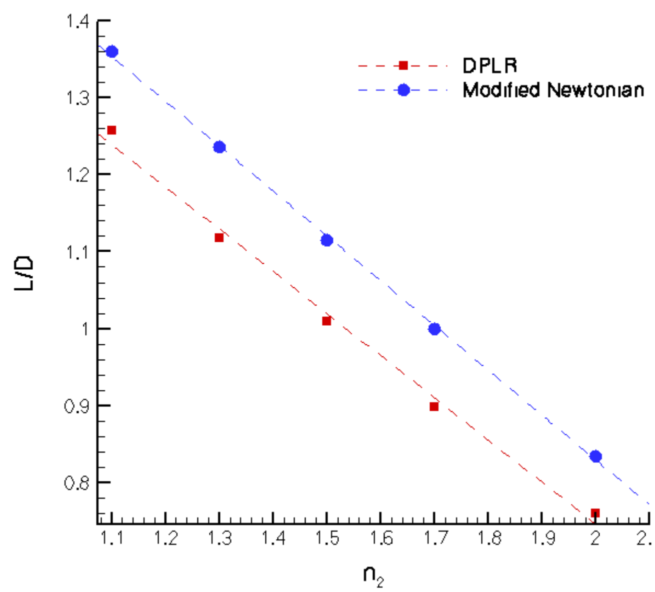

Figure 4.8: Lift to drag ratios for 89° spherical segment with varying n_2 parameter

4.5 Computational Cost Summary

Table 4.2 shows a summary of grid sizes, iteration counts, and computational time for all cases considered in this section. In order to properly mesh the parallelogram cross-section geometry, more points are needed than the simpler Apollo heat shield. As such, more computational effort is needed in general for these cases. No case took less than 900 CPU hours and 34,000 iterations to converge. The grid resolution case took over 204 days of CPU time to complete. This was facilitated by the much larger *Columbia* supercomputing cluster, as the use of 48 processors in parallel lessened the physical duration to eight and half days. All other cases were performed on the *Skystreak* cluster, using only 14 processors in parallel. The NEQAIR radiation case require 3,864 lines of sight and 966 CPU hours to complete.

Table 4.2: Summary of costs for 89°spherical segment optimized for max L/D

n_2	Grid Size (# cells)	Iterations	CPU Time (hrs)
1.1	236440	56000	1625.56
1.3	236440	65300	1738.38
1.3[a]	1205600	86200	9800.00
1.5	236440	42000	1135.54
1.7	236440	52800	1493.38
2.0	236440	34500	937.16

[a]Grid resolution case done on *Columbia* cluster

Chapter 5

Vehicle/Trajectory Optimized Geometries

5.1 Lunar Return Optimized Designs

This section presents computational solutions for heat shields that were generated for earth return following a mission to the moon using the trajectory/vehicle coupled optimization scheme discussed in Chapter 1. Due to time and computational constraints, no NEQAIR radiation simulations are undertaken for these cases. As such, only convective heating and aerodynamic calculations are presented.

5.1.1 General Summary

CFD solutions are obtained for heat shields generated using the coupled optimization technique for lunar return entry velocities, $V_E = 11$ km/s, and entry flight path angles of $\gamma_E = -6.0°$ at the location on the trajectory upon which the peak instantaneous heat flux is predicted to occur. Table 5.1 shows a summary of the geometry, design point, the aerothermodynamics calculated from DPLR solutions and the predicted aerothermodynamics using the lower-order approach for all cases studied in this section. The cases maintain their descriptors from Table 12.1 of Reference [6]. Percent differences, in reference to the DPLR solutions, are presented for the lower-order results in parenthesis where applicable. All shapes considered here have a spherical segment axial profile, as all other choices for axial shape mimicked a spherical segment as they approached an optimum. Basically, optimized power-law and spherically blunted cone geometries were disguised spherical segments for lunar return trajectories. Optimizations were performed at $L/D = 0.3$, 0.5, and 1.0 for two objective functions sets: (1) maximizing downrange while minimizing heat load and (2) maximizing cross range while minimizing heat load. Trajectory entry corridors widths of up to 1.37° were used to ensure mission feasibility (in the sense that a small change in entry flight path angle would not result in vehicle loss), and skip trajectories were used to take advantage of downrange gains incurred by such mission profiles. This analysis tended toward designs with base cross sections that were either parallelograms or pure ellipses (or combinations of the two).

As before, the analytical approach under-predicts DPLR peak stagnation point heating by 30% to 70%, and the aerodynamic solutions match up very well with the lower-order predictions (within 10% for all cases). Cases C and D experience their maximum heat flux at higher altitudes (above 64 km) than do cases A and F (below 60 km), corresponding to both the lower-order method and the CFD predicting much lower heating rates and heat loads. Since these cases do their primary deceleration occurring in lower density atmosphere, this result is expected.

The following subsections detail the differences between the the lower-order methodology and DPLR in convective heating rates for the different cases described in Table 5.1. Grid topologies are not shown for each design, but all CFD meshes are four-block structured grids with 80 points in the body normal direction. Total grid cells for each case are tabulated in Table 5.2 at the end of this section.

Table 5.1: Summary of lunar return cases

		Case			
	Parameter	A[a]	C[a] (Orion)	D[a]	F[b]
Geometry	Axial Profile[c]	SS	SS	SS	SS
	n_2	1.31	2.00	1.98	1.56
	m_1	4.00	4.00	4.00	4.00
	e	-0.967	0.0	-0.968	0.654
	θ_s	75.7°	25.0°	5.0°	23.8°
	$S_{ref,notorus}$ (m^2)	16.19	19.87	28.14	20.18
	$S_{ref,torus}$ (m^2)	16.19	21.70	33.63	21.69
Design Point	h_t (km)	57.622	64.100	66.266	59.651
	V (km/s)	10.450	10.548	10.545	10.422
	α	26.3°	-17.0°	-19.2°	-28.8°
Calculated (DPLR) Aerothermodynamics	$q_{max,conv}$ (W/cm^2)	1429.8	259.7	289.2	572.6
	$q_{s,conv}$ (W/cm^2)	543.8	156.4	194.5	394.9
	C_L	1.08	0.36	0.44	0.47
	C_D	1.15	1.41	1.49	1.07
	L/D	0.94	0.26	0.30	0.46
Predicted Aerothermodynamics	$q_{s,tot}$ (W/cm^2)	700	380	270	440
	$q_{s,conv}$ (W/cm^2)	370 (*-31.9%*)	120(*-23.3%*)	60 (*-70%*)	130 (*-67.1%*)
	C_D	1.04 (*-9.6%*)	1.49 (*5.7%*)	1.52 (*2.0%*)	1.14 (*6.5%*)
	L/D	0.95 (*1.1%*)	0.27 (*3.8%*)	0.32 (*6.7%*)	0.47 (*2.2%*)
	p_{xrs}(km)	3060	710	900	440
	p_{dwn} (km)	10790	10920	10580	25280
	$Q_{s,tot}$(kJ/cm^2)	88.0	30.3	18.5	36.9
	m (kg)	15100	10000	10500	14500

[a] Minimizing heat load and maximizing cross range, using lower mass estimation
[b] Minimizing heat load and maximizing down range, using upper mass estimation
[c] SS = spherical segment

5.1.2 Case A

Case A (see Figure 5.1) is a slender heat shield with a rounded parallelogram base much like those discussed in Chapter 4. A shape like this one is very different from a classic spherical segment and may be more difficult to implement into an actual vehicle, but its high L/D allows it to possess the greatest downrange, or the maximum horizontal distance the craft travels after entry interface, of all cases. This geometry's relatively low reference area (S_{ref}) means that it must decelerate in higher density atmosphere thus creating the most adverse heating environment. Low surface area corresponds to a low drag area ($C_D S_{ref}$) which is proportional to drag divided by dynamic pressure, itself a function of altitude (free-stream density). Basically, to achieve the same amount of deceleration (drag) using a shape with a smaller surface area, the dynamic pressure must be higher. This is achieved only at lower altitudes (corresponding to higher free-stream densities).

DPLR solutions show that absolute peak heating occurs along the leading edge of the vehicle away from the plane of symmetry at 1420 W/cm^2, which is 2.6 times the stagnation point value and well above Orion CEV feasibility limits. Essentially, in order to produce a design with greater aerodynamic maneuverability, the vehicle would need to experience heating rates higher than even the most conservative estimates for Apollo. The situation here is similar to what was observed in Chapter 4. The lower-order approach seems to not account for regions of potential high heat fluxes away from the stagnation point. These results further emphasize the dangers in using a parallelogram base cross section with n_2 close to 1.3.

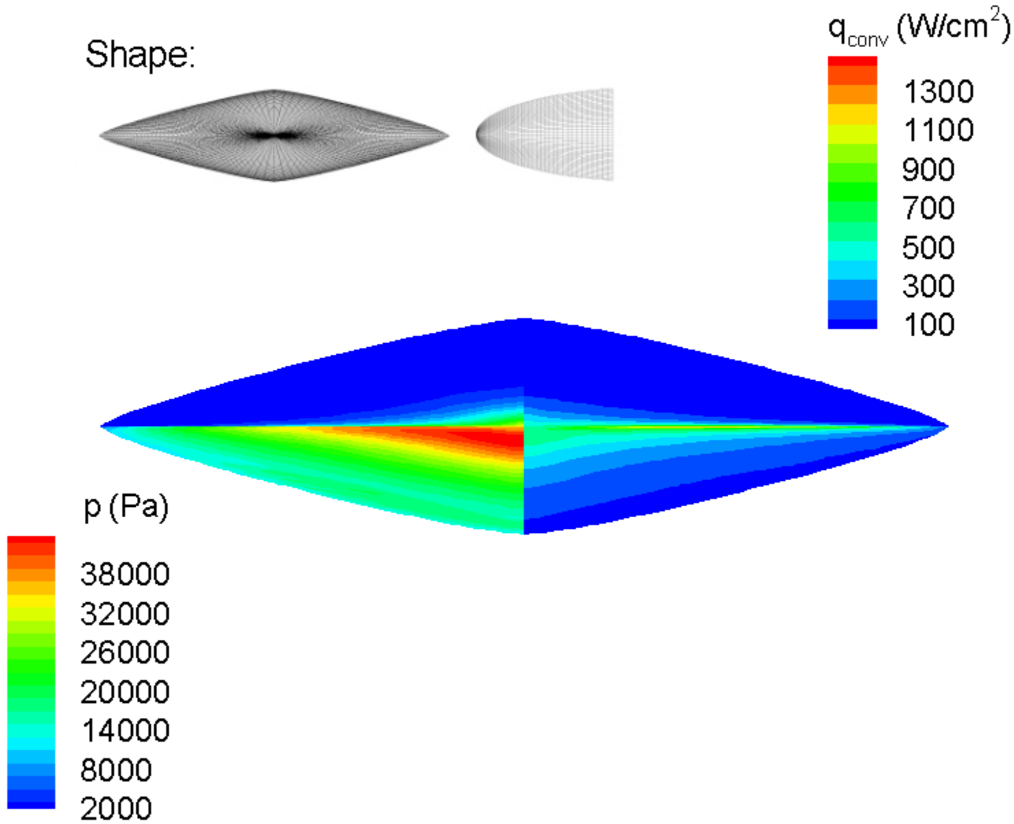

Figure 5.1: Case A surface pressure and convective heating profiles

5.1.3 Case C

Case C (see Figure 5.2) is similar in shape to the baseline Orion CEV heat shield (5.03 m diameter, $\theta_s = 25.0°$, and no eccentricity). This geometry is shown here to provide a basis of comparison for the other optimized designs. This design has a relatively low L/D, giving it the lowest cross range capabilities of all designs studied for lunar return. Like for Apollo 4, peak convective heating occurs on the symmetry plane further windward of the stagnation point at 260 W/cm^2. The Orion capsule's convective wall heat flux is lower than that of Apollo because a larger planform area allows it to decelerate much higher in the atmosphere (64.1 km vs. 61 km). Basically, the larger drag area yields a lower free stream density at peak instantaneous heating, and the lower density corresponds to lower peak heating rates.As before, the maximum convective heating pulse is 1.66 times the heating experienced at the stagnation point and is the lowest of all cases examined here. At least in terms of convective heating, this simple geometry would appear to provide the ideal performance. It remains to be seen, however, whether or not the radiating shock layer, necessary to produce lower convective heating rates, will cause total heat fluxes to exceed what is experienced by the other designs.

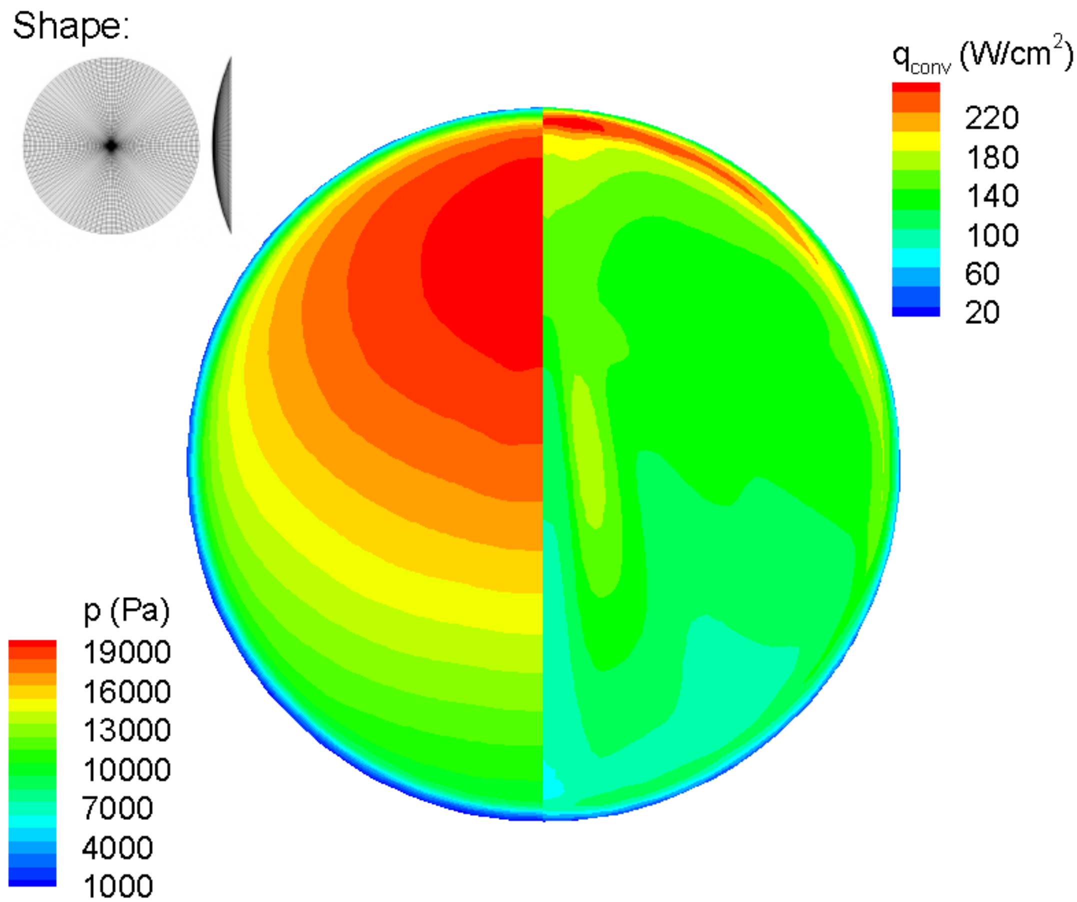

Figure 5.2: Case C (Orion) surface pressure and convective heating profiles

5.1.4 Case D

Case D (see Figure 5.3) is an oblate design with an L/D slightly larger than that of Orion (≈ 0.3). Here, peak heating is 289 W/cm^2, which is 1.49 times the heating at the stagnation point. Peaking heat is spread out all along the windward edge of the heats shield, suggesting that the effect of adding edge radius, in the form of a torus, is to temper velocity gradients as the flow is turned around that edge. Without the added curvature, peak heating rates would be extremely higher, leading to the necessity to use more sophisticated (and more expensive) thermal protection material. This case also exhibits the largest relative spread between calculated convective heating rates and low-order predictions.

The lower-order approach suggested that this geometry would experience 50% of the convective heat flux experienced by Orion. The reason being that this design would decelerate at a higher altitude in less dense atmosphere. DPLR results show that this trend does not actually exist; and that, in fact, this design's stagnation point heat flux actually exceeds that calculated for the Orion analog. This observation supports the previous assertion that non-axisymmetric shapes (i.e. those generated by an eccentric base) cause adverse heating conditions that, in turn, force the semi-empirical correlations used in the lower-order method to fail. Without flight data for such eccentric shapes, it is nearly impossible to discern the true relationship between eccentricity and the resulting heating environment.

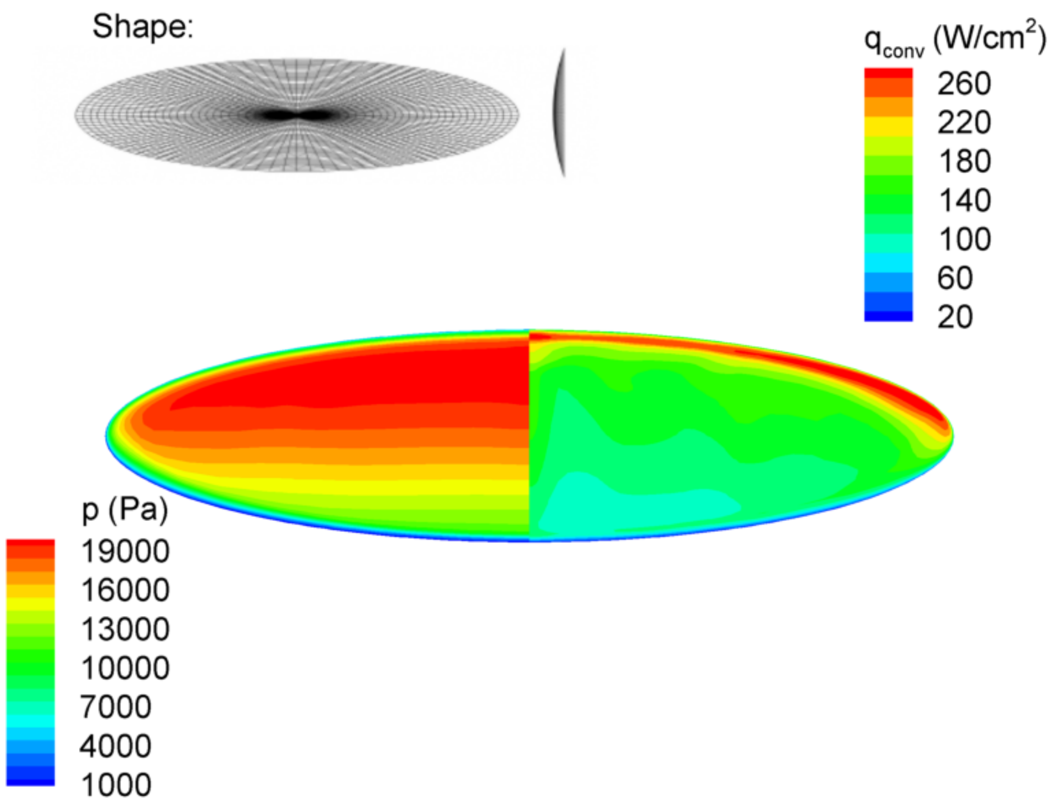

Figure 5.3: Case D surface pressure and convective heating profiles

5.1.5 Case F

Case F (see Figure 5.4) is a prolate design with a rounded diamond base optimized using a conservative mass estimation that includes a three-fold increase in heat shield mass to deal with heating loads. Peak heating is 573 W/cm^2, 1.45 times the stagnation point rate; and, it can be found further windward on the symmetry plane than the stagnation point. Greater mass forces the vehicle to decelerate lower in the atmosphere, yielding high convective heating rates, but not more than the high L/D case.

For this design, the low-order stagnation point convective heat flux underpredicts the DPLR result by 67%. Both this case and the previous one show large discrepancies in predicting the stagnation point convective heating rates using the low-order approach. The elliptical nature of these geometries would appear to force the semi-empirical correlations to report incorrect estimates. Either the method in which effective nose radius (the driver for the convective heat flux relations) is calculated is the source of this error or the correlations themselves fail to account for the true physical nature of the flow around such shapes.

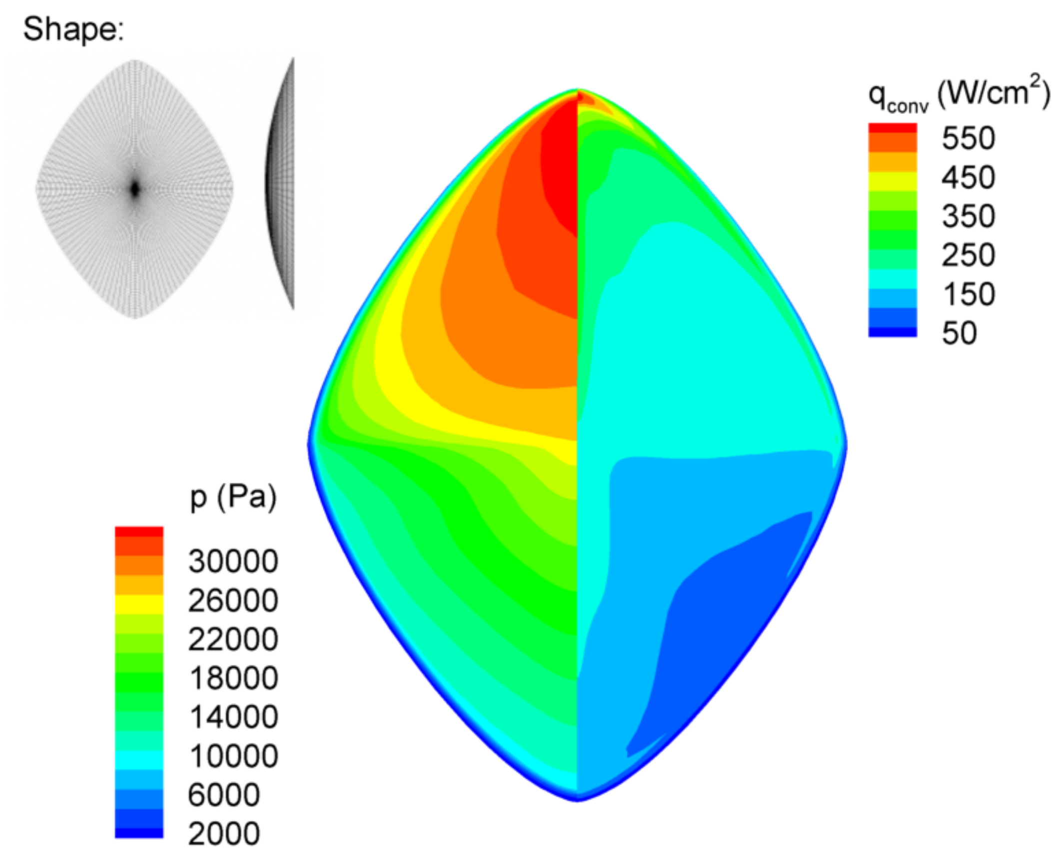

Figure 5.4: Case F surface pressure and convective heating profiles

5.1.6 Computational Cost Summary

Table 5.2 shows a summary of grid sizes, iteration counts, and computational time for all cases considered in this section. No case took less than 30,000 iterations and 1,400 CPU hours to converge. Case A needed the most iterations to converge to a stable solution due to a small pocket of subsonic flow existing at the windward exit of its mesh. More care was needed to ensure that this case was not influenced by this discrepancy and, in fact, did reach a stable solution. There exists a possibility that this boundary condition violation would introduce errors into the final solution for this case; however, results for that design are consistent with a similar shape (see Chapter 4), suggesting that the errors, if they exist, are negligible.

Table 5.2: Summary of computational costs for lunar return cases

Case	Grid Size (# cells)	Iterations	CPU Time (hrs)
A	268800	85400	3247.16
C	250880	47100	1882.16
D	336000	49300	3640
F	232960	30000	1442.78

5.2 Mars Return Optimized Designs

This section presents computational solutions for heat shields generated for earth return after a mission to Mars using the coupled trajectory/vehicle optimization scheme discussed in Chapter 1. Again, no NEQAIR simulations are included for these cases due to time and computational constraints. As such, only convective heating and aerodynamic predictions are presented. A possible breakdown of the continuum flow assumption used by DPLR is discussed in this section, but non-continuum simulations are left for future work.

5.2.1 General Summary

DPLR results are obtained for heat shields generated using the coupled optimization technique for Mars return entry velocities, $V_E = 12.5$ km/s, and entry flight path angles of $\gamma_E = -6.4°$ at the location on the trajectory upon which the predicted peak instantaneous heat flux occurs. Table 5.3 shows a summary of the geometry, design point, the aerothermodynamics calculated using DPLR, and the lower-order predicted aerothermodynamics for all cases studied in this section. The cases maintain their descriptors from Table 13.1 of Reference [6]. Percent differences, in reference to the DPLR solutions, are presented for the lower-order results in parenthesis where applicable. Both spherical segment and sphere-cone axial profiles are considered here as the optimizer generated independent geometries for these two types of topologies. All power-law optimized shapes were simply disguised versions of the two other profiles. Optimizations were performed at $L/D = 0.3$ and 0.5

for two objective functions sets: (1) maximizing downrange while minimizing heat load and (2) maximizing cross range while minimizing heat load. No optimizations were done at $L/D = 1.0$ because those designs resulted in heat loads that were considered infeasible.[4] Smaller entry corridor widths of up to 0.79° were necessary to generate flyable trajectories here.

Similarly to the lunar return cases, designs with the lowest heat loads will experience their peak heat pulses at much higher altitudes. For all Mars return cases, DPLR reports stagnation point convective heat fluxes much lower than does the simple, analytical method. For example, the stagnation point heat flux for case B is only 19% that of what was calculated using the modified Newtonian approach. At Mars return velocities, the shock layer is actually larger than at lower speeds (larger shock stand off distance); and, consequently, shock layer radiation should play a larger role in the resulting heating profile for a given blunt-body heat shield. A firm grasp of the potentially strong coupling between convection and radiation must be reached before making any concrete conclusions about the designs studied in this section. Still, there is a great deal to glean from comparing the higher order simulation with lower-order predictions, especially if the aim is to improve the lower-order method for use in initial design studies.

Furthermore, most of these cases require the addition of increased numerical dissipation for convergence. This increased dissipation is necessary due to the possibility of non-continuum flow present at these entry conditions. Continuum flow can be classified through the use of the Knudsen number, K_N, which is the ratio of mean free path (distance a molecule will travel before colliding with another molecule) to a characteristic length. Mean free path, in turn, is a function of temperature divided by pressure.[13] Regions of relatively high temperature and relatively low pressures are more likely for the higher Mars return velocities, yielding values of K_N that may violate the continuum requirement of $K_N < 0.3$. Another way to classify non-continuum flow is by using the gradient-length local Knudsen number:[73]

$$K_{N,GLL} = \frac{\lambda}{Q} \left| \frac{dQ}{dl} \right| \tag{5.1}$$

where λ is the mean free path, Q is a flow property (usually temperature), and l is a distance between two points in the flow field along the direction of steepest gradients. Continuum breakdown occurs when the value of this parameter is less than 0.05, and this definition of Knudsen number is better suited to the discretized flow fields used in computational fluid dynamics as it is relatively easy to extract gradients from a computational solution. Adding extra dissipation may force continuum flow to exist everywhere in the flow field, but it adds further sources of error to the solutions. Though results are consistent with what is seen at lunar return velocities, it is paramount that this additional source of error be classified and quantified before robust conclusions are made. Such classifications are left in the realm of future work.

The following subsections detail the differences between the the lower-order methodology and DPLR in convective heating rates, as the aerodynamic predictions are almost identical, for the different cases described in Table 5.3. Grid topologies are not shown for each design, but all CFD meshes are four-block structured grids with 80 points in the body normal direction. Total grid cells for each case are tabulated in Table 5.4 at the end of this section.

Table 5.3: Summary of Mars return cases

		Case			
	Parameter	A[a]	B[a] (Orion)	D[a]	F[b] (*Orion*)
Geometry	Axial Profile[c]	SS	SS	SC	SS
	n_2	1.66	2.00	2.00	2.00
	m_1	4.00	4.00	4.00	4.00
	e	0.621	0.0	-0.968	0.0
	θ_s	23.7°	25.0°	-	25.0°
	θ_c	-	-	88.4°	-
	r_n/d	-	-	3.95	-
	$S_{ref,notorus}$ (m^2)	20.26	19.87	36.83	19.87
	$S_{ref,torus}$ (m^2)	21.83	21.70	44.65	21.70
Design Point	h_t (km)	62.488	63.729	67.671	62.565
	V (km/s)	11.749	11.776	111.847	11.824
	α	-28.5°	-17.0°	-17.7°	-17.0°
Calculated (DPLR) Aerothermodynamics	$q_{max,conv}$ (W/cm^2)	656.94	319.57	235.8	361.11
	$q_{s,conv}$ (W/cm^2)	446.3	182.3	128.0	248.0
	C_L	0.48	0.36	0.46	0.36
	C_D	1.11	1.41	1.59	1.40
	L/D	0.43	0.26	0.289	0.26
Predicted Aerothermodynamics	$q_{s,tot}$ (W/cm^2)	950	980	640	1160
	$q_{s,conv}$ (W/cm^2)	160 (*-64.1%*)	170(*-6.7%*)	90 (*-29.7%*)	190 (*-23.4%*)
	C_D	1.16 (*4.5%*)	1.49 (*5.7%*)	1.60 (*0.6%*)	1.49 (*6.4%*)
	L/D	0.43 (*9.3%*)	0.27 (*3.8%*)	0.31 (*7.3%*)	0.27 (*3.8%*)
	p_{xrs}(km)	1600	910	890	1160
	p_{dwn} (km)	11320	11440	13200	25960
	$Q_{s,tot}$(kJ/cm^2)	69.8	68.2	38.3	82.6
	m (kg)	10100	10000	11200	13100

[a] Minimizing heat load and maximizing cross range, using lower mass estimation
[b] Minimizing heat load and maximizing down range, using upper mass estimation
[c] SS = spherical segment, SC = sphere-cone

5.2.2 Case A

Case A (see Figure 5.5) is a prolate shape, similar to Case F for lunar return, with the highest L/D of all shapes considered here; however, this maneuverability comes at the cost of having, by far, the highest maximum convective heat flux. Peak convective heating (657 W/cm^2) occurs along the axis symmetry further windward of the stagnation point and is 1.47 times greater than the calculated value there. The lower-order stagnation point convective heat flux is 64% lower than the DPLR calculation, which is the largest discrepancy in this category for all cases for Mars return.

Notably, this case is the only one studied in this section that does not need extra numerical dissipation to converge. This suggests that continuum flow assumption is valid for this design at its predicted peak heating trajectory point and that the conclusions drawn from these results are free of the additional errors that plague the other heat shields examined for Mars return. Case F for lunar return, which is nearly the same shape as this design, shows an almost identical offset for stagnation point convective heat flux (a 67% difference between the lower-order methodology and DPLR). In that respect, this severe under-prediction by the lower-order approach implies that the semi-empirical correlations are not suited to a shape of this class for the same reasons as discussed in Section 5.1.5.

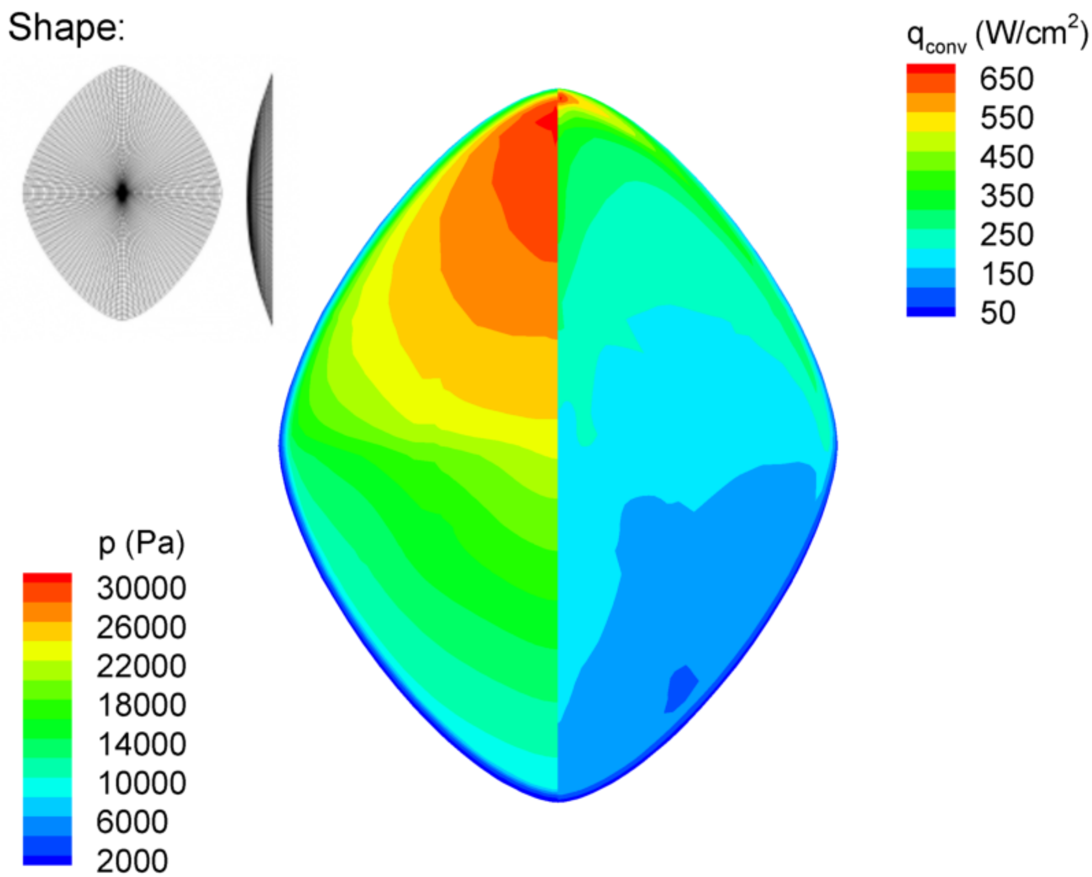

Figure 5.5: Case A surface pressure and convective heating profiles

5.2.3 Cases B and F - Orion Analogs

Cases B (see Figure 5.6) and F (see Figure 5.7) are Orion sized spherical segments (5.03 m diameter, $\theta_s = 25.0°$, no eccentricity) simulated using a lower (no additional heat shield mass added to account for heat loads) and an upper (three-fold increase in heat shield mass) mass estimation respectively. Both cases have peak heating occurring along the axis of symmetry further windward of the stagnation point. Peak heat flux is 1.45 (320 W/cm^2) and 1.75 (361 W/cm^2) times that experienced at the stagnation point for the lower and upper mass estimations respectively. These particular values bracket the baseline Apollo value (1.66) and fall well within the span of what was observed for lunar return.

Both modified Newtonian solution sets report stagnation point convective heat fluxes that are relatively similar to their DPLR counterparts (7% and 23% less respectively). Since added dissipation was needed for these cases, it is reasonable to assume that the true difference between the two approaches will actual be larger (on the order of what was observed for Apollo and axisymmetric lunar return designs). When mass is increased, the lower-order method shows a stagnation point heat flux increase of 12%. Essentially, additional mass translates to a lower altitude deceleration and, thus, higher heating rates. DPLR solutions, on the other hand, show a 36% increase convective heating rate at the stagnation point. This is a relatively modest increases that may be an artifact pf the added dissipation. Still, nothing in the CFD results suggest that anything other than altitude is responsible for the increase in convective heat flux.

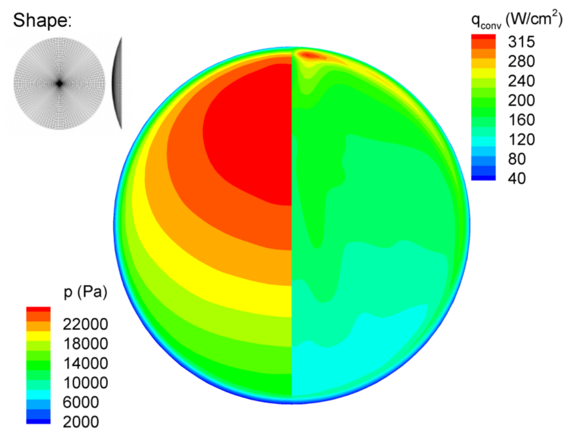

Figure 5.6: Case B (Orion) surface pressure and convective heating profiles

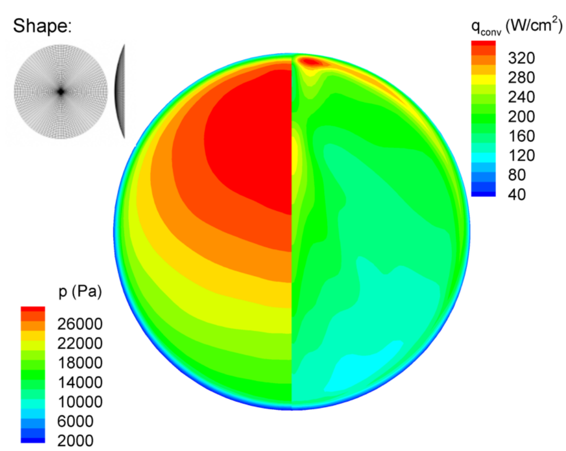

Figure 5.7: Case F (Orion) surface pressure and convective heating profiles

5.2.4 Case D

Case D (see Figure 5.8) represents an oblate design, with similar L/D to the Orion analog heat shield, optimized for minimized heat load an maximum cross range using the lower mass estimation. Peak heating is spread out along the windward edge of the vehicle upstream of the stagnation point. Peak convective heat flux (236 W/cm^2) is 2.15 times more that which is experienced at the stagnation point (128 W/cm^2), and the lower-order approach under-estimates stagnation point heating rates by approximately 30%. Though this case has an eccentric base, the discrepancy between DPLR and low-order results is on the order of what was observed for Apollo 4. Simply, while eccentricity pushes the convective heat flux up, the added dissipation drops the calculated rate, creating a false sense of consistency with axisymmetric cases (the lower order method under-predicts computational solutions by $\approx 70\%$ for all other elliptical base cases).

This case was meant to represent a marked improvement over the baseline Orion geometry as its larger surface area should allow for lower heat loads and heat fluxes, while maintaining similar aerodynamic performance (i.e. L/D, p_{xrs}, p_{dwn}). At first glance, the DPLR results show such an improvement. A comparison of the two cases reveals that peak convective heating decreases by a modest 26% while stagnation point convective heating lowers by 30% when comparing this case to the low mass Orion analog. Similarly, the modified Newtonian approach predicts a slightly larger 35% decrease in stagnation point heat flux between the two cases. The more elliptical heat shield shows a marked decrease in peak heating when compared to a simple spherical segment. This is the opposite trend than was observed for lunar return. There, the heating rate actually increased when transitioning from an axisymmetric heat shield to an elliptical one. The disparity that exists between the different flight regimes stems, most likely, from the poor classification of non-continuum effects that precipitates the need for added numerical dissipation, rather than something physically different in the flow fields for Mars and lunar return.

Furthermore, it is interesting to note that surface heating contours for Case D show that peak heating is more spread out over the entire windward edge of the heat shield as opposed to the more local and concentrated heat pulse displayed in case B. This means that the highest heat loads would potentially be more widely spread over the elliptic heat shield, forcing the addition of more thermal material which, in turn, adds to vehicle weight. Simply, there is no single metric here that can prove whether or not this shape is really an improvement over the simpler axisymmetric geometry. Really, until all the errors of non-continuum flow and the elliptical effects can be quantified into improved empirical correlations, it will always be difficult to determine which shape is more ideal.

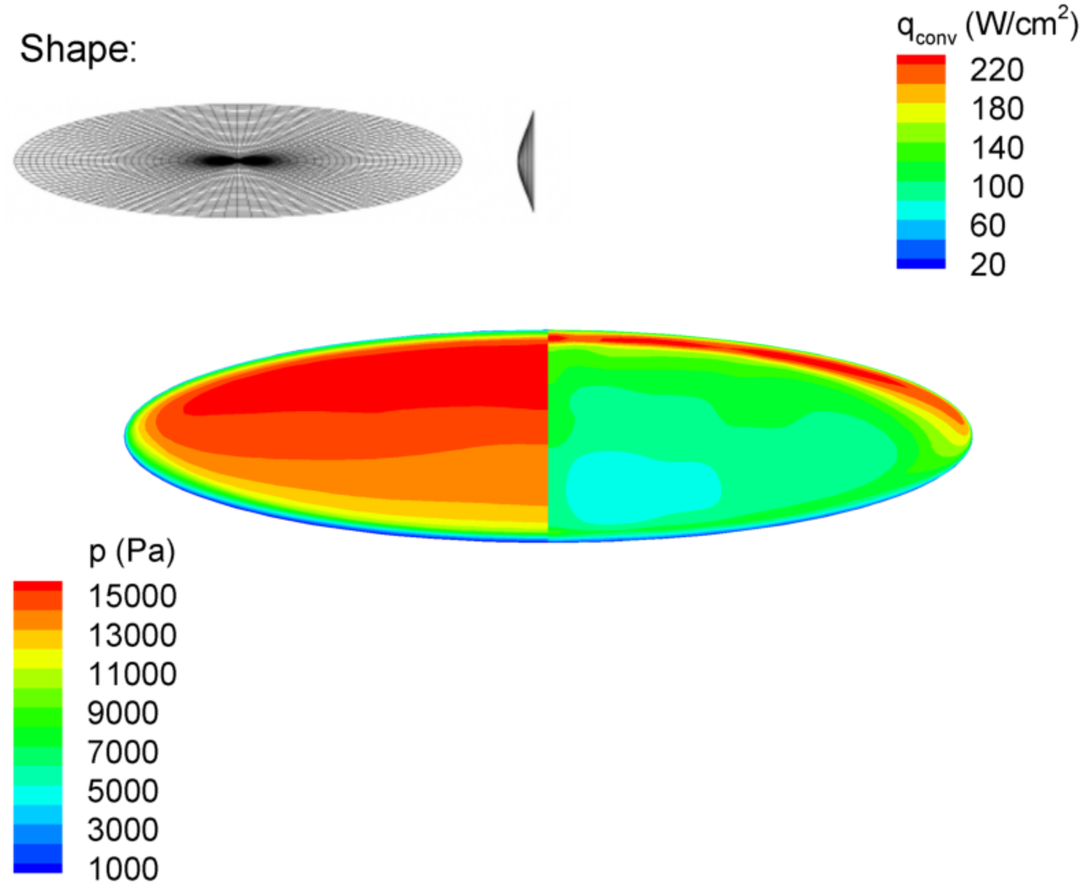

Figure 5.8: Case D surface pressure and convective heating profiles

5.2.5 Computational Cost Summary

Table 5.4 shows a summary of grid sizes, iteration counts, and computational time for all cases considered in this section. No case took less than 30,000 iterations and 800 CPU hours to converge. Case D needed the most time to arrive at a steady state solution, possibly due to side-effects from the added dissipation. Case A, which needed no extra numerical dissipation, converged the fastest, while the other cases were all much more computationally intensive. Probably, the numerical dissipation, though helping keep the solution stable, is the source of the slow convergence rates.

Table 5.4: Summary of computational costs for Mars return cases

Case	Grid Size (# cells)	Iterations	CPU Time (hrs)
A	219520	30500	847.84
B	250880	52600	1773.38
D	250780	91100	2714.46
F	250880	40600	1446.67

Chapter 6

Conclusions

6.1 Summary of Results

In general, computational fluid dynamics solutions of the Apollo 4 capsule and of optimized heat shield geometries show that the lower-order approach discussed in Chapter 1 gives reasonable estimations of aerothermodynamic properties useful for initial design studies. Particularly, CFD solutions show that the modified Newtonian approach, as expected, gives highly accurate predictions for the aerothermodynamic parameters (i.e. C_L, C_D, and L/D); however, large disparities in convective and radiative (where applicable) heating profiles are seen. The following subsections detail the important results discussed in this work.

6.1.1 Apollo 4 Benchmarking

For the Apollo axisymmetric heat shield at Apollo 4 peak heating conditions, the lower-order approach under-predicts convective stagnation point flux by 30% and over predicts stagnation point radiative heat flux by 16% when compared to computational solutions. These disparities can be attributed to the failure of the lower-order method to capture boundary layer physics. The correlations used to calculate the heating profiles in the analytical approach were formulated for simple axisymmetric shapes like spheres; as such, these offsets provide a useful baseline for all other comparisons of the computational solutions to the lower-order ones. Essentially, if the errors seen for other geometries exceed the ones seen here, then other inaccuracies, above and beyond boundary phenomena, must exist in the lower-order approach. Though these errors are modest but significant, combining the two heating regimes yields an offset of only 8% for total heat flux between the two approaches. The errors that manifest themselves in the low-order correlations used to calculate heat transfer would appear to cancel each other out.

Edge radius plays a major role in the aerothermodynamics of a blunt-body heat shield, especially with regards to its heating environment. Ignoring curvature at the edges of the heat shield introduces discontinuities in the heating profile and may even cause a violation of DPLR boundary conditions. For the Apollo capsule, peak heating decreases as a power law function of the exact curvature that exists at the edge of the vehicle, even at an angle of attack that would place the stagnation point further away from the windward edge of the heat shield. Including edge radius as a design variable in the design process may prove difficult without more detailed mission profiles, but is necessary to add this feature if the a true optimum geometry is desired. One way to implement edge curvature into the optimization process would be to blend a torus, of either fixed or variable radius, to the geometries generated by the process discussed in Chapter 1. This addition would cause additional computational cost, through the addition of mesh points and the possible inclusion of more optimization constraints, but the results would provide a much more accurate representation of what would be expected aerothermodynamically from an actual blunt-body heat shield.

6.1.2 High L/D shapes

For a representative slender, high L/D heat shield with $n_2 = 1.3$, the lower-order approach under-estimates stagnation point convective heating by 44% and over-predicts stagnation point radiative heat flux by 79% compared to the computational solutions. For convective heat flux the percent offset is similar to what was observed for the Apollo benchmark case because the stagnation point falls in a highly spherical region of the heat shield. Still the 14% increase (from 30% seen for Apollo 4 to 44% seen here) in convective heat flux offset (comparing the lower-approach to DPLR solutions) suggests that the elliptical nature of the base cross section may cause the relations sued to predict this value in the lower-order approach to break down. The stagnation point radiative heat flux offset is much larger than the 16% seen for the axisymmetric Apollo case. Likely, the process by which shock stand-off distance (the driving factor for radiative heat flux) is calculated is not suitable for a slender body such as this one. Still, more evidence to this effect would need to be accrued before this assertion could be truly corroborated. Again, combining the two heating rates calculated computationally generates a result that compares favorably (within 20%) to what was predicted using the lower-order approach.

At Apollo 4 peak heating conditions, using $n_2 = 1.3$ does indeed produce high lift geometries; however, the heating profiles for these shapes show maximum convective heating to be more than twice what is experienced at the stagnation point. The effective sharpness of the base cross-section creates a sharp leading edge near the boundaries of the heat shield when the axial profile is added to complete the geometry. While not exactly a discontinuity, the low bluntness at this leading edge generates a thin shock layer that contributes to the adversely high heating rates experienced near the edges of the heat shield. This same thin shock layer generates negligible radiative heat transfer at the point of highest heating, but the maximum convective heating is still almost twice that of the total heat flux at the stagnation point (where peak radiative heating occurs). Some newer materials might be able to withstand heating rates at or near 1000 W/cm^2, but that would push design limitations imposed for the current Orion CEV capsule and significantly add to vehicle cost. For the representative high L/D shape, maximum convective heating decreases as a power law as the n_2 parameter is increased. A an approximate 40% reduction in peak convective heating can be obtained by increasing the n_2 parameter to 1.5 while still maintaining an L/D greater than 1. As such, future optimizations should alter the lower bound on this n_2 parameter to 1.4 or 1.5 in order to generate high L/D geometries without the adverse off stagnation point heating seen here..

6.1.3 Coupled Vehicle/Trajectory Optimized Geometries

For lunar return, shapes with eccentric bases (either prolate or oblate) show qualitative discrepancies in heating profile when compared to the modified Newtonian solutions. A close examination of DPLR solutions show that any possible gains from increased surface area and higher altitude decelerations are wiped out by changes in the flow-field introduced by stretched geometries. As such, there is reason to suspect that these eccentric shapes fall outside the realm of the semi-empirical correlations used in the lower-order method for heat fluxes. Simply, the correlations are not valid for every class of blunt-body heat shield created by the lower-order optimization process. These relations can, however, be improved through the use of a larger data set of wind tunnel data and CFD solutions (like those seen in this thesis) that includes more shapes with eccentric bases and sharp edges. For Mars return, errors associated with non-continuum flow (manifesting itself in increased dissipation) and eccentricity effects make it difficult to make any concrete conclusions regarding the merits of one design over another. These errors need to be quantified and accounted for before any such study may continue.

Furthermore, it can be seen that it is difficult to produce heat shields that show a great deal of improvement, for both lunar and Mars return, over one with geometric parameters similar to that which is currently in consideration for the Orion CEV capsule. Any advantages gained by using a more novel shape will, more than likely, be canceled out by the ease of manufacturing and vehicle integration for an Apollo-like spherical segment design. Whether intended or not, it would appear that a simple spherical segment with $\theta_s = 25.0°$ is indeed an ideal shape for earth entry at super orbital velocities.

6.2 Future Work

Future additions to this work fall into four categories: 1) better radiation modeling, 2) material response, 3)turbulence, and 4) other atmospheres for entry. The heating profile for a blunt-body heat shield can not accurately be calculated unless convection and radiation are fully coupled. Loosely coupling the two with NEQAIR and DPLR is possible with the technique described in Chapter 2, but future versions of DPLR will contain internal methods for dealing with shock layer radiation, allowing for much simpler acquisition of fully coupled solutions without the high computation costs associated with using NEQAIR. Materials play a major role, through ablation, in determining the heat actually felt by the vehicle. All materials will undergo sometime sort of chemical change when exposed to the extreme environments experienced during re-entry. Future CFD solutions, and the lower-order optimized geometries for that matter, need to take into account how chemical changing in a vehicle's surface will change the resulting flow-field around a next generation space capsule (i.e. the gas model changes as the environment is no longer just air) if truly accurate solutions are desired.

All CFD solutions in this work assume a laminar flow. It is not entirely obvious weather or not earth entering heat shields will experience local regions of turbulent flow. To that end, it would be germane to adopt a some sort of transition criteria, based on flow physics, and then apply turbulence models, within DPLR, to those regions to correctly model the flow. This transition criteria might be more pertinent in different planetary atmospheres such as Mars, where turbulent flow is much more likely to exist. Furthermore, since a next generation space capsule will be used for missions that require entry to the atmospheres of other planets, it would be interesting to see how the shapes studied in this work, optimized for earth entry, measure up in different environments, like that on Mars.

6.3 Concluding Remarks

At this point, it is important to try to understand the computational results compiled in this work in a more general perspective. The purpose of conducting high fidelity CFD on geometries optimized using a low-order approach was to evaluate how well that analytical method could predict the extreme aerothermodynamic environments these geometries would experience on a real mission. To that end, the CFD results show that the aerodynamic model used by the low-order approach does a more than adequate job in predicting the proper pressure distribution on the heat shield surface, while the correlations used to predict the thermodynamic environment prove poor, even in circumstances for which they were derived for (i.e. spheres). Also, these stagnation point heating models fail to pick up areas of high heat flux on other parts of the vehicle's surface, highlighting a further shortcoming of the lower-order analytical approach. All of these conclusions were, to some extent, expected; but the process by which they were obtained implies possible improvements for the lower-order approach. Namely, that the empirical relations used to predict heating rates need to be replaced with improved correlations with a more physical basis and that the geometric constraints used in the optimization process need to be further limited in order to avoid large local off-stagnation point heat fluxes.

Furthermore, the results gathered in this work allow for some conclusions to be made about the blunt-body design space in general. Presently, there are very few physical data points for blunt-body entry at extra-planetary velocities.

As such, the empirical relations derived from those data points break down when they are used for unconventional shapes. In order to improve these correlations, more data must be obtained through flight and ground tests as well as through further computational simulations. That way, curve fits derived from this larger data set will truly reflect the full range of possible outcomes. Finally, the lower-order method sought to show that more complicated shapes could provide large gains over the simpler, axisymmetric geometries. However, in practice, the more complex shapes introduce aspects into the blunt-body flow field (i.e. high off stagnation point heating and other elliptical effects) that do not manifest themselves with the simpler shapes. Sometimes the simpler approach can be the better one; and, certainly in this work, it can be seen that choosing a simpler shape (in this case a 25° spherical segment) can be more advantageous, in many respects, than a more complicated design.

BIBLIOGRAPHY

[1] Allen, H. J. and Eggers, Jr., A. J., "A Study of the Motion and Aerodynamic Heating of Ballistic Missiles Entering the Earth's Atmosphere at High Supersonic Speeds," *Forty-Fourth Annual Report of the NACA - 1958*, 1959, pp. 1125–1140, NACA TR-1381.

[2] Johnson, J. E., Starkey, R. P., and Lewis, M. J., "Aerothermodynamic Optimization of Reentry Heat Shield Shapes for a Crew Exploration Vehicle," *Journal of Spacecraft and Rockets*, Vol. 44, No. 4, 2007, pp. 849–859.

[3] Johnson, J. E., Starkey, R. P., and Lewis, M. J., "Coupled Entry Heat Shield/Trajectory Optimization for Lunar Return," *AIAA Atmospheric Flight Mechanics Conference*, Aug. 2008, AIAA 2008-6557.

[4] Johnson, J. E., *Aerothermodynamic Optimization of Earth Entry Blunt Body Heat Shields for Lunar and Mars Return*, Ph.D. thesis, Department of Aerospace Engineering, University of Maryland, College Park, 2009.

[5] Johnson, J. E., Starkey, R. P., and Lewis, M. J., "Entry Heat Shield Optimization for Mars Return," *47th AIAA Aerospace Sciences Meeting*, Jan. 2009, AIAA 2009-518.

[6] Johnson, J. E., *Multidisciplinary Optimization of Non-Spherical, Blunt-Body heat Shields for a Planetary Entry Vehicle*, Master's thesis, Department of Aerospace Engineering, University of Maryland, College Park, 2006.

[7] Gielis, J., "A Generic Geometric Transformation that Unifies a Wide Range of Natural and Abstract Shapes," *American Journal of Botany*, Vol. 90, No. 3, 2003, pp. 333–338.

[8] Bertin, J. J., *Hypersonic Aerothermodynamics*, AIAA Education Series, New York, 1994.

[9] Rasmussen, M., *Hypersonic Flow*, Wiley, New York, 1994.

[10] Regan, F., *Re-Entry Vehicle Dynamics, 1st Ed.*, AIAA education Series, New York, New York, 1994.

[11] Anderson, J. D., *Fundamentals of Aerodynamics, 3rd Ed.*, AIAA Education Series, New York, 2001.

[12] NOAA, NASA, and USAF, "U.S. Standard Atmosphere, 1976," *NASA TM X-58091*, April.

[13] Anderson, J. D., *Hypersonic and High Temperature Gas Dynamics Second Edition*, AIAA Education Series, New York, 2006.

[14] Tauber, M. E. and Menees, G. P., "Aerothermodynamics of Transatmospheric Vehicles," *Journal of Aircraft*, Vol. 24, No. 9, 1987, pp. 594–602.

[15] Fay, J. A. and Riddell, F. R., "Theory of Stagnation Heat Transfer in Dissociated Air," *Journal of Aeronautical Sciences*, Vol. 25, No. 2, 1958, pp. 73–85.

[16] Lovelace, U. M., "Charts Depicting Kinematic and Heating parameters for Ballistic Reentry Speeds of 26,000 to 45,000 Feet per Second," *NASA TN D-968*, Oct. 1961.

[17] Tauber, M. E. and Sutton, K., "Stagnation Point Radiative Heating Relations for Earth and Mars Entries," *Journal of Spacecraft and Rockets*, Vol. 28, 1991, pp. 40–42.

[18] Tannehill, J. C. and Mugge, P. H., "Improved Curve Fits for the Thermodynamic Properties of Equilibrium Air Suitable for Numerical Computation Using Time-Dependent or Shock-Capturing Methods," *NASA-TM-X-74335, NOAA-S/T-76-1562*, Oct. 1976.

[19] Kaattari, G. E., "Shock Envelopes of Blunt Bodies at Large Angles of Attack," *NASA TN D-1980*, Dec. 1963.

[20] Kaattari, G. E., "A Method for Predicting Shock Shapes and Presssure Distributions for a Wide Variety of Blunt Bodies at Zero Angle of Attack," *NASA TN D-4539*, April 1968.

[21] Ried, Jr., R. C., Rochelle, W. C., and Milhoan, J. D., "Radiative Heating to the Apollo Command Module: Engineering Prediction and Flight Measurement," *NASA TM X-58091*, April 1972.

[22] *Design Optimization Tools (DOT) Ver 4.20*, Vanderplaats Research & Development Inc., Colorado Springs, CO, 1995.

[23] Rankins, F., *The University of Maryland Parallel Trajectory Optimization Program User's Manual*, College Park, MD, 2007.

[24] Starkey, R. P., Rankins, F., and Pines, D., "Effects of Hypersonic Cruise Trajectory Optimization Coupled with Airbreathing Vehicle Design," *44th AIAA Aerospace Sciences Meeting and Exhibit*, Reno, Nevada, January 2006, AIAA 2006-2036.

[25] Stevens, B. L. and Lewis, F. L., *Aircraft Control and Simulation*, John Wiley & Sons, Ltd., New York, 1992.

[26] Madavan, N. K., "On Improving Efficiency of Differential Evolution for Aerodynamic Shape Applications," Aug. 2004, AIAA 2004-4622.

[27] Deb, K., *Multi-Objective Optimization Using Evolutionary Algorithms*, John Wiley & Son, Ltd., Chichester, England, 2001.

[28] Powell, R. W., Striepe, S. A., Desai, P. N., and Braun, R. D., *Program to Optimize Simulated Trajectories (POST) Volume 2 Utilization Manual*, Hampton, VA, October 1997.

[29] Young, J. W. and Smith, R. E., "Trajectory Optimization for an Apollo-Type vehicl Under Entry Conditions Encountered During Lunar Return," May 1967, NASA TR-R-258.

[30] Graves, C. A. and Harpold, J. C., "Re-Entry Targeting Philosophy and flight Results from Apollo 10 and 11," January 1970, AIAA 1970-28.

[31] Wright, M. J., Candler, G. V., and Bose, D., "Data-Parallel Line Relaxation Method for the Navier-Stokes Equations," *AIAA journal*, Vol. 36, No. 9, 1998, pp. 1603–1609.

[32] Wright, M. J., Prabhu, D. K., and Martinez, E. R., "Analysis of Apollo Command Module Afterbody Heating Part I: AS-202," *Journal of Thermophysics and heat Transfer*, Vol. 20, No. 1, 2006, pp. 16–30.

[33] Wright, M. J., Loomis, M. A., and Papadopoulos, P. E., "Aerothermal Analysis of the Project Fire II Afterbody Flow," *Journal of Thermophysics and heat Transfer*, Vol. 17, No. 2, 2003, pp. 240–249.

[34] Gnoffo, P. A., Gupta, R. N., and Shinn, J. L., "Conservation Equations and Physical Models for Hypersonic Air Flows in Thermal and Chemical Nonequilibrium," February 1989, NASA TP-2867.

[35] Gnoffo, P. A., "An Upwind-Biased, Point-Implicit Relaxation Algorithm for Viscous, Compressible Perfect-Gas Flows," 1990, NASA TP-2953.

[36] Lee, D. B. and Goodrich, W. D., "The Aerothermodynamic Environment of the Apollo Command Module During Superorbital Entry," *NASA TN D-6792*, Jan. 1972.

[37] Gnoffo, P. A., Gupta, R. N., and Shinn, J. L., "Conservation Equations and Physical Models for Hypersonic Air Flows in Thermal and Chemical Nonequilibrium," 1989, NASA TP-2867.

[38] Park, C., *Nonequilibrium Hypersonic Aerothermodynamics*, John Wiley & Sons, New York, 1990.

[39] Park, C., "Assessment of a Two-Temperature Kinetic Model for Dissociating and Weekly Ionizing Nitrogen," *Journal of Thermophysics and Heat Transfer*, Vol. 2, No. 1, 1988, pp. 8–16.

[40] Olynick, D. R., Henline, W. D., Chambers, L. H., and Candler, G. V., "Comparison of Coupled Radiative Flow Solutions wit Project Fire II Flight Data," *Journal of Thermophysics and Heat Transfer*, Vol. 9, No. 4, December 1995.

[41] Milikan, R. C. and White, D. R., "Systematics of Vibrational Relaxation," *Journal of Chemical Physics*, Vol. 39, No. 12, 1963, pp. 3209–3213.

[42] Gupta, R., Yos, J., Thomspon, R., and Lee, K., "A Review of Reaction Rates and Thermodynamic and Transport Properties for an 11-species Air Model for Chemical And thermal Nonequilibrium Calculations to 30,000 K," August 1990, NASA RP-1232.

[43] Ramshaw, J. D., "Self-Consistent Effective Binary Diffusion in Multicomponent Gas Mixtures," *Journal of Non-Equilibrium Thermodynamics*, Vol. 15, No. 3, 1990, pp. 295–300.

[44] MacCormack, R. W. and Candler, G. V., "The solution of the Navier-Stokes equations using Gauss-Seidel line relaxation," *Computers & Fluids*, Vol. 17, No. 1, 1989, pp. 135–150.

[45] Yee, H. C., "A Class of High-Resolution Explicit and Implicit Shock Capturing Methods," Feb. 1989, NASA TM-101088.

[46] McCormack, R. W., "Current Status of the Numerical Solutions of the Navier Stokes Equations," January 1985, AIAA Paper 85-0032.

[47] Saunders, D. A., Yoon, S., and Wright, M. J., "An Approach to Shock Envelope Grid tailoring and Its Effect on Reentry Vehicle Solutions," *44th AIAA Aerospace Sciences Meeting and Exhibit*, Reno, Nevada, January 2007, AIAA 2007-207.

[48] *PathScale Compiler Suite Ver. 3.2*, PathScale, Sunnyvale, CA, 2008.

[49] *Open MPI v1.4.1*, http://www.open-mpi.org, 2008.

[50] *Intel Fortran Compiler User and Reference Guides*, Intel Corporation, 2008, Document Number: 304970-006US.

[51] Stallman, R. M. and the GCC Developer Community, "Using the GNU Compiler Collection," 2008.

[52] *PGI Fortran Reference*, The Portland Group, Lake Oswego, OR, 2008.

[53] *LAM/MPI User's Guide Version 7.1.4*, The LAM/MPI Team, Open Systems Lab, July.

[54] *Pointwise Ver. 16.03*, Pointwise, Inc., Ft. Worth, TX, 2009.

[55] *Gridgen Version 15.09*, Pointwise, Inc., Fort Worth, TX.

[56] Thomas, P. D. and Middlecoff, J. F., "Direct Control of the Grid Point Distribution in Meshes Generated by Elliptic Equations," *AIAA Journal*, Vol. 18, No. 6, June 1980.

[57] Sorenson, R. L. and Steger, J. L., "Numerical generation of Two-Dimensional grids by the use of Poisson Equations with Grid Control at Boundaries," *NASA. Langley Research Center Numerical Grid Generation Tech.*, Jan. 1980.

[58] Holst, T., "Elements of Computational Fluid Dynamics," March 1991, from ENAE 685 class notes.

[59] *Rhinoceros Version 4.0*, McNeel North America, Seattle, Washington, 2006, www.rhino3d.com.

[60] Whiting, E. E., Park, C., Yen, L., Arnold, J. O., and Peterson, J. A., "NEQAIR96, Nonequilibrium and Equilibrium Radiative Transport and Spectra Program: User's Manual," December 1996, NASA RP-1389.

[61] Pace, A. E., Ruffin, S. M., and Bose, D., "A Loosely-Coupled Approach to Shock-Layer Radiation Modeling in DPLR," *41st AIAA Thermophysics Conference*, San Antonio, Texas, June 2009, AIAA 2009-4312.

[62] Bose, D., McCorkle, E., Thompson, C., Bogdanoff, D., Prabhu, D., Allen, G., and Grinstead, J., "Analysis of Model Validation of Shock Layer Radiation in Air," *46th AIAA Aerospace Sciences Meeting and Exhibit*, Reno, Nevada, AIAA 2008-1240.

[63] Hillje, E., "Entry Aerodynamics at Lunar Return Conditions Obtained from the Flight of Apollo 4 (AS-501)," *NASA TN D-5399*, 1969.

[64] Moseley, Jr., W. C., Moore, Jr., R. H., and Hughes, J. E., "Stability Characteristics of the Apollo Command Module," *NASA TN D-3890*, March 1967.

[65] Crowder, R. S. and Moote, J. D., "Apollo Entry Aerodynamics," *Journal of Spacecraft and Rockets*, Vol. 6, 1969, pp. 302–307.

[66] Park, C., "Stagnation-Point Radiation for Apollo 4," *Journal of Thermophysics and Heat Transfer*, Vol. 18, No. 3, 2004, pp. 349–357.

[67] Pavlovsky, J. and Leger, L., "Apollo Experience Report - Thermal Protection Subsystem," *NASA TN D-7564*, Jan. 1974.

[68] Curry, D. M. and Stephens, E. W., "Apollo Ablator Thermal Performance at Super-Orbital Entry Velocities," *NASA TN D-5969*, Sept. 1970.

[69] Bartlett, E. P., Abbett, M. J., Nicolet, W. E., and Moyer, C. B., "Improved Heat Shield Design Procedures for Manned Entry Systems, Part II: Application to Apollo," *NASA CR-108689*, June 1970.

[70] Park, C., "Stagnation-Point Radiation for Apollo 4: A Review and Current Status," June 2004, AIAA Paper 2001-3070.

[71] Chambers, L. H., "Predictive Radiative Heat Transfer in Thermochemical Nonequilibrium Flow Fields: Theory and User's Manual for LORAN," September 1994, NASA TM-4564.

[72] Balakrishnan, A., Park, C., and Green, M. J., "Radiative Viscous Shock Layer Analysis of Fire II, Apollo, and PSET Flight Data," *Thermophysical Aspects of Re-Entry Flows*, edited by J. N. Moss and C. D. Scott, Progress in Astronautics and Aeronautics Vol 103, 1986, pp. 514–540.

[73] Boyd, I. D., Chen, G., and Candler, G. V., "Predicting Failure of the Continuum Fluid Equations in Transitional Hypersonic Flows," *Phyiscs of Fluids*, Vol. 7, No. 1, Jan. 1995, pp. 210–219.